JGR Earth Surface

RESEARCH ARTICLE
10.1029/2021JF006345

Large-Scale Tectonic Forcing of the African Landscape

C. P. B. O'Malley[1,2], N. J. White[1], S. N. Stephenson[1,3], and G. G. Roberts[2]

[1]Bullard Laboratories, Department of Earth Sciences, University of Cambridge, Cambridge, UK, [2]Department of Earth Science and Engineering, Imperial College London, London, UK, [3]Department of Earth Sciences, University of Oxford, Oxford, UK

Key Points:

- Continent-wide inventories of longitudinal river profiles preserve recoverable signals of regional uplift
- Tectonically forced landscape simulations enable testing of inverse modeling strategies
- Closed-loop modeling suggests that fluvial landscapes are dominated by tectonic forcing

Supporting Information:

Supporting Information may be found in the online version of this article.

Correspondence to:

C. P. B. O'Malley and N. J. White, conor.omalley19@imperial.ac.uk; njw10@cam.ac.uk

Citation:

O'Malley, C. P. B., White, N. J., Stephenson, S. N., & Roberts, G. G. (2021). Large-scale tectonic forcing of the African landscape. *Journal of Geophysical Research: Earth Surface*, *126*, e2021JF006345. https://doi.org/10.1029/2021JF006345

Received 22 JUL 2021
Accepted 28 OCT 2021

Author Contributions:

Conceptualization: C. P. B. O'Malley, N. J. White
Validation: C. P. B. O'Malley, N. J. White, S. N. Stephenson, G. G. Roberts
Visualization: C. P. B. O'Malley, N. J. White
Writing – review & editing: C. P. B. O'Malley, N. J. White, S. N. Stephenson, G. G. Roberts

Abstract Successful inverse modeling of observed longitudinal river profiles suggests that fluvial landscapes are responsive to continent-wide tectonic forcing. However, inversion algorithms make simplifying assumptions about landscape erodibility and drainage planform stability that require careful justification. For example, precipitation rate and drainage catchment area are usually assumed to be invariant. Here, we exploit a closed-loop modeling strategy by inverting drainage networks generated by dynamic landscape simulations in order to investigate the validity of these assumptions. First, we invert 4,018 African river profiles to determine an uplift history that is independently calibrated, and subsequently validated, using separate suites of geologic observations. Second, we use this tectonic forcing to drive landscape simulations that permit divide migration, interfluvial erosion and changes in catchment size. These simulations reproduce large-scale features of the African landscape, including growth of deltaic deposits. Third, the influence of variable precipitation is investigated by carrying out a series of increasingly severe tests. Inverse modeling of drainage inventories extracted from simulated landscapes can largely recover tectonic forcing. Our closed-loop modeling strategy suggests that large-scale tectonic forcing plays the primary role in landscape evolution. One corollary of the integrative solution of the stream-power equation is that precipitation rate becomes influential only if it varies on time scales longer than ~1 Ma. We conclude that calibrated inverse modeling of river profiles is a fruitful method for investigating landscape evolution and for testing source-to-sink models.

Plain Language Summary There is excellent geologic evidence that large portions of the African landscape were lifted up above sea level over the last 30 million years by upward flow of hot mantle rocks beneath the tectonic plate. The strongest evidence comes from marine deposits which contain fossil fish and sea snakes that are now perched at elevations of hundreds of meters in the middle of the North African desert. Mantle processes gave rise to an egg-carton pattern of gigantic swells and depressions that characterizes much of the continent. As the landscape evolved, it was sculpted and eroded by the action of massive rivers such as the Niger, the Nile and the Congo. Height along the length of each of these rivers varies and appears to preserve a memory of landscape growth. In that sense, rivers appear to act as tape recorders of tectonic processes such as mantle flow. Here, we use computer simulations of an evolving landscape to test the idea that rivers contain mantle memories. These simulations, which include complexities such as variable rainfall, allow rivers to develop naturally as landscapes grow. Our results suggest that the African landscape and its drainage patterns contain valuable information about deep Earth processes.

1. Introduction

We investigate how large-scale tectonic forcing can influence landscape development. The combined forward and inverse modeling strategy that we exploit is known as closed-loop modeling or twin experimentation (Canet et al., 2009; Li et al., 2011; Lorenz, 1963). This approach is often employed by the seismological community and is a helpful means for objectively investigating complex systems that is based upon a combination of guided forward and inverse modeling. Here, we adopt a three-fold strategy. First, we extract a regional uplift history by inverting a revised and augmented inventory of river profiles. This approach builds upon previous work by Paul et al. (2014), Wilson et al. (2014), and Rudge et al. (2015). The recovered history is independently calibrated, and then separately tested (i.e., validated) using two different suites of geologic observations. Second, the recovered uplift history is used to force a series of dynamic landscape simulations for a sequence of increasingly complex spatio-temporal precipitation patterns. Finally, synthetic river profiles extracted from these simulated landscapes are inverted in order to gauge recoverability of the original regional uplift history. It is important to emphasize that the source of the original uplift history is not relevant—the principal issue concerns recoverability of any

original signal by a simplified inverse modeling algorithm. This form of closed-loop modeling can be independently assessed by comparing observed and predicted sedimentary flux at major offshore deltas. Our principal aim is to determine whether or not the simplifying assumptions that underpin the inverse algorithm are robust. We focus our study on the Cenozoic epeirogeny of Africa, Arabia and Madagascar where the spatial and temporal pattern of regional uplift is reasonably well understood.

Generation of regional plateaux with elevations of $O(1)$ km (i.e., of order 1 km) and wavelengths of $O(10^3)$ km interspersed with low-lying depressions throughout the African continent has long been debated (see, e.g., Burke, 1996; Holmes, 1945; King, 1978; Nyblade & Robinson, 1994). Africa is surrounded by passive margins and, apart from the East African Rift, it is unaffected by significant Cenozoic orogeny. Its distinctive "basin-and-swell" physiography is considered to be a consequence of mantle convective upwelling and downwelling beneath the lithospheric plate (Al-Hajri et al., 2009; Braun et al., 2014; Burke, 1996; Fairhead, 1979; Gurnis et al., 2000; Hartley et al., 1996; Moucha & Forte, 2011; Nyblade & Sleep, 2003). At wavelengths $\gtrsim$800 km, admittance and coherence studies of gravity and topography demonstrate that sub-crustal density differences, rather than flexural rigidity, act to support topography (Ebinger et al., 1989; S. M. Jones et al., 2012; McKenzie & Fairhead, 1997; McKenzie, 2010). Thus crustal isostasy does not completely account for swell elevation (Nyblade & Robinson, 1994; Paul et al., 2014). This important inference is corroborated by detailed measurements of residual depth anomalies of oceanic lithosphere along African margins. For example, a series of topographic swells intersects the west African coastline that is manifest by positive residual depth anomalies on the adjacent oceanic floor (Hoggard et al., 2017). Surface wave tomographic models show that the "basin-and-swell" physiography coincides with shear wave velocity anomalies that lie beneath the plate (Al-Hajri et al., 2009; Fishwick, 2010).

During Paleogene times, stratigraphic and geomorphic observations suggest that most of Africa either had low relief and sat at, or close to, sea level (Figure 1a; Burke, 1996). There are two significant observations. First, Late Cretaceous and Cenozoic marine sedimentary rocks crop out across North Africa and Arabia (R. Guiraud et al., 2001; Sahagian, 1988; Ziegler, 2001). As shown in Figure 1a, we draw attention to four specific locations, although it is important to emphasize that evidence for marine incursions is more widespread. Details of a selection of marine fossils found at each location, which are later used to validate our independently calibrated erosional parameters, are listed in Table 1. At Location ① on the Arabian peninsula, Madden et al. (1980) document a diverse Paleocene vertebrate fauna within the Umm Himar Formation that crops out at an elevation of ~1,200 m near Jabal Umm Himar at the southern end of Harrat Hadan. This fauna contains abundant sharks, eagle rays, and rarer pycnodont fish that are consistent with shallow marine and estuarine paleoenvironment. At Location ② in western Yemen, Al-Subbary et al. (1998) and Al-Qayim et al. (2005) mapped and analyzed the basal Zijan Member of the widespread Medj-zir Formation, which crops out at elevations of 2.0–2.4 km and consists of shallow marine sandstones containing *Thalassinoides* and *Orbitulina discordea*. At Location ③ in the Atlas Mountains of North Africa, Late Cretaceous limestones crop out at an elevation of ~970 m at the edge of the deeply dissected Kem Kem plateau near Gara Es Sba (Martill et al., 2011). Here, finely laminated deposits contain an abundant assemblage of marine fish, including Actinopterygii (e.g., *Belonostomus sp*.) and Macrosemiidae (e.g., *Agoultichthys chattertoni*). A thick Eocene sequence of interbedded carbonate deposits, shales, and phosphatic conglomerates crop out at an elevation of ~400 m at Location ④ near Tamaguélelt on the edge of the Tilemsi valley of northeastern Mali (Tapanila et al., 2008). The phosphatic conglomerates are highly fossiliferous and contain some of the largest species of Palaeophiidae and Nigerophiidae snakes, including a giant sea snake *Palaeophis colossaeus* and an ammonite *Libycoceras ismaeli* (Bellion et al., 1989; McCartney et al., 2018). Mudstones and wackestone carbonate rocks contain a diverse variety of cephalopods, echinoderms, and benthic foraminifera that include *Cibicides reinholdi* and *Operculinoides bermudezi* (Berggren, 1974). Outcrops of Albian-Cenomanian marine sedimentary rocks across North Africa, the Horn of Africa, and the Benue Trough show that large portions of these regions were below sea level (Figure 1; Petters, 1978; Reyment & Dingle, 1987). Sahagian (1988) interpolates between outcropping Cenomanian shoreline deposits to estimate that 1–2 km of Cenozoic epeirogenic uplift occurred across much of Africa. Similar inferences can be made for northern and eastern Arabia, as well as for Madagascar (Figure 1a; Brown et al., 1989; Dixey, 1960; Powers et al., 1966; G. G. Roberts et al., 2012; M. J. de Wit, 2003; Ziegler, 2001).

Second, within a 20° belt straddling the equator that embraces much of central Africa and southern Arabia, lateritic and bauxitic weathering profiles developed during the Eocene and Oligocene times (Beauvais et al., 2008; Guillocheau et al., 2017; Gunnell & Burke, 2008; Moufti, 2010). These chemical precipitates and associated

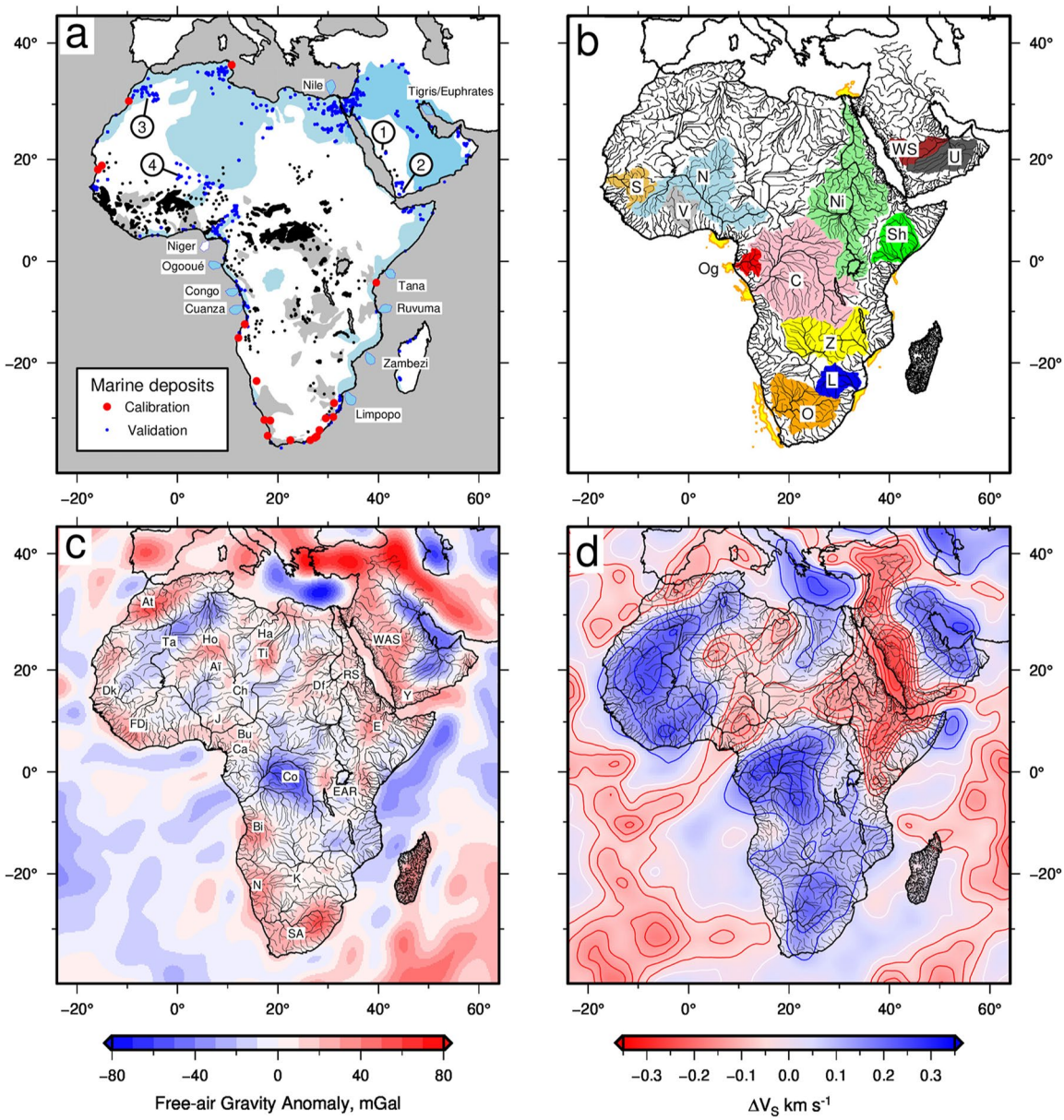

Figure 1. (a) Paleogeography of Africa and Arabia. Lighter/darker blue polygons = extent of marine deposition during Cenomanian and Eocene times for Africa and Arabia, respectively (R. Guiraud et al., 2001; Sahagian, 1988; Ziegler, 2001); red dots = locations of marine rocks used to calibrate v by Rudge et al. (2015); blue dots = Late Cretaceous to Eocene marine deposits (see, e.g., Uhen et al., 2019); black polygons = Paleogene lateritic deposits; gray polygons = degraded lateritic and paleosol deposits (Beauvais & Chardon, 2013; Botha, 2000; Brown et al., 1989; Chardon et al., 2006; Coleman et al., 1983; Gunnell & Burke, 2008; Moufti, 2010; Guillocheau et al., 2017); blue labeled polygons at river mouths = deltas dominated by Paleogene carbonate deposition, except Niger delta which has shale deposition (Ismail et al., 2010; Lavier et al., 2001; Nyagah, 1995; Salman & Abdula, 1995; Séranne & Nzé Abeigne, 1999; Wilson et al., 2014; Ziegler, 2001). Numbered circles = specific loci described in text. (b) Present-day fluvial catchments. WS = Wadi Subay; U = unnamed; Ni = Nile; N = Niger; S = Senegal; V = Volta; Og = Ogooué; C = Congo; Sh = Shebelle; Z = Zambezi; L = Limpopo; O = Orange. (c) Long wavelength (i.e., ≥ 800 km) free-air gravity field calculated from GRACE measurements (Tapley et al., 2007). Drainage network = >4,000 rivers used to calculate regional uplift as function of time and space (see Figure 2); yellow polygons = principal deltas with significant Neogene clastic deposition (Bluck et al., 2007; Haack et al., 2000; Lavier et al., 2001; Nyagah, 1995; Reijers, 2011; Salman & Abdula, 1995; Séranne & Nzé Abeigne, 1999; Sestini, 1989; Walford, 2003); Aï = Aïr Massif; At = Atlas Mountains; Bi = Bié Dome; Bu = Biu Plateau; Ca = Cameroon Line; Ch = Chad Basin; Co = Congo Basin; Df = Darfur Dome; Dk = Dakar; E = Ethiopian Highlands; EAR = East African Rift; FDj = Fouta Djallon Plateau; Ha = Haruj; Ho = Hoggar Swell; J = Jos Plateau; K = Kalahari Basin; N = Namibian Dome; RS = Red Sea Flank; SA = South African Plateau; Ta = Taoudeni Basin; Ti = Tibesti Massif; WAS = Western Arabian Swell; Y = Yemeni Volcanic Province. (d) Shear wave velocity anomaly averaged between 100 – 200 km depth from surface wave tomographic model (Schaeffer & Lebedev, 2013). Drainage network as before.

Table 1
Marine Fauna Used to Validate Calibrated Value of v

Location	Lon.	Lat.	Elev.	Genus/species	Environment	Reference
Jabal	41.422	21.186	1,244	Pycnodus	Shallow marine	Madden et al. (1980)
Umm	41.420	21.188	1,244	Myliobatidae	Open marine	Madden et al. (1980)
Himar	41.411	21.187	1,246	Squatina	Marine	Madden et al. (1980)
①	41.405	21.196	1,236	Eotorpedo	Marine	Whitmore and Madden (1994)
Western	43.633	15.425	1,803	Ostracoda	Marine	Al-Subbary et al. (1998)
Yemen	44.104	13.936	2,339	Choffatella	Marine	Beydoun (1966)
②	44.746	13.938	2,067	Thalassinoides	Marine	Al-Qayim et al. (2005)
Tilemsi	0.131	19.861	416	Laffitteina	Marine	Bellion et al. (1989)
Valley	0.131	19.861	416	Valvulinaria	Marine	Bellion et al. (1989)
③	0.131	19.861	416	Nonionella	Marine	Bellion et al. (1989)
Dur At	18.505	26.588	334	Thalassinoides	Marine	Abouessa et al. (2012)
Talah	17.833	28.833	141	Ostrea	Shallow marine	Abouessa et al. (2012)
Toshka	31.300	21.300	332	Coleoidea	Marine	Košťák et al. (2013)
Gebel Gifata	28.000	26.500	215	Nostoceratidae	Marine	Tantawy et al. (2001)
Oman	55.900	24.900	278	Chaetetidae	Shallow marine	Skelton et al. (1990)
Mtns.	55.859	24.300	328	Dictyoptychus	Marine	Skelton et al. (1990)
Gebel Hafit	55.800	24.100	316	Terebratulina	Shallow marine	Bitner and Boukhary (2012)
Eastern	37.100	31.600	531	Basilosaurus	Marine	Zalmout et al. (2000)
Jordan	36.600	31.500	669	Nummulites	Marine	Zachos et al. (2008)
Sokoto	5.702	13.436	323	Mosasauroidea	Shallow marine	Soliar (1988)
Somal-	44.900	9.900	1,497	Nummulites	Marine	Haas and Miller (1952)
iland/	46.000	9.800	990	Deltoidonautilus	Shallow marine	Haas and Miller (1952)
Puntland	48.500	8.400	461	Vulsella	Marine	Piccoli and Savazzi (1983)
	49.316	8.853	694	Nummulites	Marine	Azzaroli (1958)
Congo	13.500	−5.900	318	Xiphodolamia	Marine	Adnet et al. (2009)
Senegal	−15.900	14.600	30	Amiidae	Marine	O'Leary et al. (2012)
Gueran	−13.894	25.095	182	Archaeoceti	Marine	Gingerich and Zouhri (2015)
Khenc-	6.900	34.900	923	Membraniporidae	Marine	Allegre (1939)
Hela	8.100	35.400	887	Dyrosauridae	Shallow marine	Jouve (2005)
El Kem	8.709	36.191	695	Guembelitria	Marine	Keller et al. (1995)
	9.100	35.900	921	Globigerinelloides	Marine shelf	Keller et al. (2002)
Ouled	−6.938	32.750	616	Argillochelys	Marine	Tong and Hirayama (2008)
Abdoun	−6.371	32.879	874	Elopomorpha	Marine	Cavin et al. (2000)

surfaces are preserved when fluvial run-off is limited, which implies that paleotopographic gradients were modest (Thomas, 1994; Thorne et al., 2012). Low relief persisted into Paleogene time across western and central Africa where an extensive series of etchplains have been mapped (Guillocheau et al., 2017; Gunnell & Burke, 2008). Many of these surfaces are capped by lateritic and saprolitic deposits. ^{39}Ar–^{40}Ar radiometric dating of minerals (e.g., cryptomelane) that grew during lateralization combined with stratigraphic relationships suggest that this region had negligible topographic relief between 70 and 40 Ma (Beauvais & Chardon, 2013; Beauvais et al., 2008; Brown et al., 1989; Chardon et al., 2006; Coleman et al., 1983; Guillocheau et al., 2017; Gunnell & Burke, 2008; Moufti, 2010).

African physiography suffered major reorganization during Late Paleogene (35–30 Ma) times. Widespread basaltic magmatism associated with topographic swells developed throughout Africa (Aït-Hamou et al., 2000;

Burke, 1996; Ebinger et al., 2000; Lo et al., 1992). At the same time, there was a marked switch from carbonate to clastic deposition at the fringes of most, but not all, deltas (Abu El-Ella, 1990; Delaunay, 2018; Reijers, 2011; Séranne & Anka, 2005; Walford et al., 2005). Where topographic swells intersect the African and Arabian coastlines, emergent Quaternary marine terraces with significant height variations are observed, which suggests that these swells are growing at rates of $O(0.1)$ mm a^{-1} or more (Elmejdoub & Jedoui, 2009; M. Guiraud et al., 2010; D. L. Roberts & Brink, 2002; Walker et al., 2016). During this period, the African Plate has been moving slowly with respect to a mantle plume reference frame (Burke, 1996). The present-day plate motion is 1 ± 0.5 mm a^{-1} in a NE direction which translates into $0.1 \pm 0.05°$ Ma^{-1} (DeMets et al., 2010; Gripp & Gordon, 1990). This rich diversity of geologic observations means that the African continent is an excellent natural laboratory, which we can exploit to test a closed-loop modeling approach.

2. Inverse Modeling Strategy

A number of strategies have been used to parameterize the response of river longitudinal profiles to changes in base level (e.g., Anderson & Anderson, 2010; Howard et al., 1994). The empirical stream power equation is often used to describe how the geometry of a river profile evolves with time (e.g., Whipple & Tucker, 1999). Height along a river profile, z, as a function of distance along the profile, x, and time, t, is controlled by competition between rate of rock uplift, U, and rate of erosion, E, so that

$$-\frac{\partial z}{\partial t} = U(x,t) + E(x,t), \tag{1}$$

where

$$E(x,t) = -\upsilon A^m \left(\frac{\partial z}{\partial x}\right)^n + \kappa \left(\frac{\partial^2 z}{\partial x^2}\right). \tag{2}$$

The first term of this equation is advective and determines the speed at which slopes propagate upstream. This speed depends upon the local gradient and upon stream power, which is proportional to υA^m where A is the upstream drainage area. υ and m are erosional constants that must be obtained by independent calibration and validation (Rudge et al., 2015). The value of the empirical exponent n is subject to debate. Here, we assume that $n = 1$ since it yields the smallest misfit between large numbers of observed and calculated river profiles (Paul et al., 2014). This assumption enables an efficient solution to the inverse problem (e.g., Rudge et al., 2015). In Supporting Information S1, we present a series of landscape simulations where $n = 1.5$ and $n = 2$ are assumed (Figure S1). When synthetic river profiles extracted from these simulations are subsequently inverted by assuming $n = 1$, the overall similarity of recovered uplift rate histories and landscapes confirms that our assumption is an appropriate one at the scales of interest (Figures S2–S5 in Supporting Information S1). The second term of Equation 2 is diffusive and, provided that $\kappa < 10^7$ m^2 Ma^{-1}, it has been shown that this term can be safely ignored (Rosenbloom & Anderson, 1994; Rudge et al., 2015). Thus, we infer that the advective retreat of a signal is the dominant control at the scales under consideration. An appropriately modified stream power equation is

$$-\frac{\partial z}{\partial t} = -\upsilon A^m \frac{\partial z}{\partial x} + U(x,y,t), \tag{3}$$

where $U(x, y, t)$ represents the rate of regional uplift as a function of space and time. This equation is often solved by assuming that the river profile is in equilibrium (i.e., $\partial z/\partial t = 0$). If $\log(\partial z/\partial x)$ is plotted as a function of $\log(A)$, m and U/υ are estimated from the slope and intercept. This popular form of analysis has obvious drawbacks. Here, we are more interested in determining uplift rate as a function of time and space and so we solve Equation 3 by posing the more general inverse problem. The smoothest distribution of $U(x, y, t)$ that minimizes the misfit between observed and calculated river profiles is sought (Fox et al., 2014; Parker, 1994; Pritchard et al., 2009; G. G. Roberts & White, 2010). By fitting long wavelength features along river profiles, we are assuming that a distinction can be made between knickzones (i.e., $O(10^2 - 10^3)$ km changes in slope) that are generated by the spatio-temporal pattern of regional uplift rate, U, and knickpoints (i.e., $O(10^{-1} - 10^0)$ km changes in slope) that could be generated by lithologic and other intrinsic and/or extrinsic factors (e.g., Wapenhans et al., 2021). Figures 2g–2i suggests there is a relatively weak correlation between lithology and channel elevation, slope, curvature, or steepness index on the large scales of interest (Hartmann & Moosdorf, 2012).

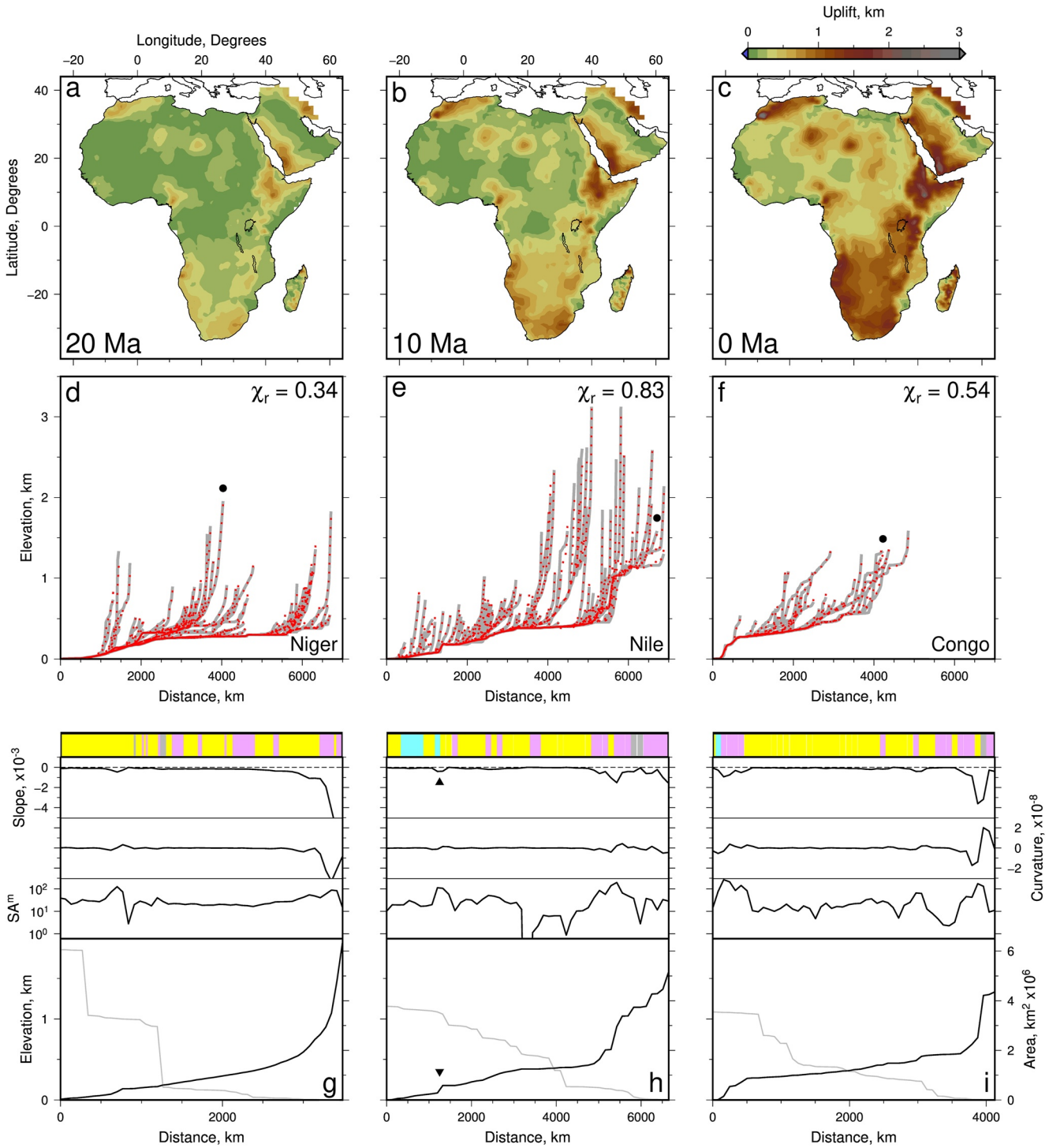

Figure 2. (a) Cumulative uplift of Africa and Arabia at 20 Ma calculated by inverse modeling of 4,018 longitudinal river profiles. (b) Same at 10 Ma. (c) Same at present day. (d) Gray lines = observed river profiles from Niger catchment; red dotted lines = calculated river profiles determined by inverse modeling where χ_r = RMS misfit; black dot = profile shown in panel (g). (e and f) Same for Nile and Congo catchments. (g) Knickpoint analysis of Niger river profile. Horizontal colored strip = bedrock lithology where yellow = siliciclastic sedimentary rocks, pink = metamorphic rocks, blue = carbonate/evaporite sedimentary rocks, gray = water (Hartmann & Moosdorf, 2012); black lines = slope, curvature, steepness index ($S = \frac{\partial z}{\partial x}$), and elevation of river profile indicated by black dot in panel (d); dashed line = zero reference; gray line = upstream drainage area of Niger. (h) Same for Nile where black triangles indicate locus of Aswan dam. (i) Same for Congo river.

Following Lighthill and Whitham (1955) and Rudge et al. (2015), we exploit the method of characteristics to solve the linear inverse problem. First, Equation 3 is recast as two ordinary differential equations where

$$\frac{dx}{dt} = -vA^m,$$

and

$$\frac{dz}{dt} = -U(x(t), t). \tag{4}$$

The appropriate boundary conditions are

$$x = x^*, \quad z = z^* \quad \text{at} \quad t = 0,$$

$$\text{and} \quad x = 0, \quad z = 0 \quad \text{at} \quad t = \tau_G, \tag{5}$$

where z^* is elevation at a distance x^* along the river profile and τ_G is the time at which a river profile records an uplift signal at some position (x^*, z^*). Thus a knickzone located at x^* takes τ_G years to advect upstream from a river mouth at $x = 0$. G. G. Roberts et al. (2012) refer to τ_G as the Gilbert time, where

$$\tau_G = \int_0^{x^*} \frac{dx}{vA^m}. \tag{6}$$

The response time of a given landscape is governed by τ_G, which represents the time taken for a spatially invariant uplift signal to travel upstream. In this way, model temporal resolution can be gauged from river length, assuming that it is reasonable to average v and m over long length scales and timescales.

Following Lighthill and Whitham (1955) and Pritchard et al. (2009), a solution for Equations 2–5 is written in integral form as

$$z^* = \int_0^{\tau_G} U(x(t), t)\ dt. \tag{7}$$

Rudge et al. (2015) showed that Equations 2 and 4 can be used to invert for uplift rate written in matrix form, $\mathbf{U}$, by minimizing the misfit between observed and predicted values of (x^*, z^*), subject to spatial and temporal smoothing, by solving

$$|\mathbf{MU} - \mathbf{z}|^2 + \lambda_s^2|\mathbf{SU}|^2 + \lambda_t^2|\mathbf{TU}|^2, \tag{8}$$

where $\mathbf{U} \geq 0$. In this matrix formulation, $\mathbf{z}$ represents a set of observed river profiles and $\mathbf{MU}$ the corresponding set of predicted river profiles. S and T represent spatial and temporal smoothing operators that are weighted by parameters λ_s and λ_t (Rudge et al., 2015). The smoothest model that yields the smallest misfit between observed and calculated profiles is sought (Parker, 1994). Optimal values of λ_s and λ_t are identified by carrying out a parameter sweep across multiple inverse models (Rudge et al., 2015). We note that alternative methods of solving the inverse problem have been proposed and implemented by Fox et al. (2014), Goren et al. (2014), and Glotzbach (2015), G. G. Roberts and White (2010), and G. G. Roberts et al. (2012).

2.1. Inverse Modeling of Africa, Arabia, and Madagascar

G. G. Roberts and White (2010) developed a one-dimensional inverse modeling approach and applied it to selected river profiles from three uplifted domes in sub-equatorial Africa. This approach was generalized by G. G. Roberts et al. (2012) and Paul et al. (2014) who developed and applied a non-linear optimization scheme that simultaneously fits inventories of river profiles from Madagascar and Africa, respectively. Rudge et al. (2015) showed that a linear inverse model can be used to obtain essentially the same result but at a greatly reduced computational cost. Here, we present a revised cumulative uplift history of Africa, Arabia, and Madagascar (Figure 2). River profiles were extracted using standard flow-routing algorithms from the 30 m resolution digital elevation model determined by the Shuttle Radar Topography Mission (Becker et al., 2009; Jenson & Domingue, 1988).

These profiles were manually checked for elevation and drainage area artifacts, and the fidelity of recovered drainage planforms was compared with satellite imagery. In this way, the original drainage inventories of Paul et al. (2014), Wilson et al. (2014), and G. G. Roberts et al. (2012) have been revised and augmented with a view to improving both accuracy and spatial resolution.

The value of m is straightforward to determine since it directly affects the misfit between observed and calculated river profiles. Paul et al. (2014) identified a weak global minimum at $m = 0.35$. If $n = 1$, this value of m is consistent with the work of Stock and Montgomery (1999) and of Whipple and Tucker (1999), who suggested that the concavity index for fluvial channels (i.e., $\theta = m/n$) falls within the range 0.35–0.6. Paul et al. (2014) used this calibrated value of m in combination with incision rate estimates from Angolan rivers to obtain $v = 3.62\ \mathrm{m}^{0.3}\ \mathrm{Ma}^{-1}$ (M. Guiraud et al., 2010). These values of m and v yielded predicted values of cumulative uplift across Africa that broadly concurred with independent constraints such as emergent marine stratigraphy, volcanism, deltaic sedimentary flux, and thermochronometry. Rudge et al. (2015) carried out a comprehensive sweep of inverse models for a wide range of values of v with a view to matching predicted and observed uplift rates for emergent marine strata that fringe the west and south African coastlines (Figure 1a). Their optimal value of $v = 3.62\ \mathrm{m}^{0.3}\ \mathrm{Ma}^{-1}$ agrees with that of Paul et al. (2014). For Arabia, Wilson et al. (2014) exploited fluvial incision measurements from lava flows to show that $v = (9.678 \times 10^3)(3.4164018 \times 10^9)^{-m}$, which yields $v = 4.46 \pm 0.2$ if $m = 0.35$. Based upon these studies, our starting assumption is that $v = 3.62 \pm 1\ \mathrm{m}^{0.3}\ \mathrm{Ma}^{-1}$ where $m = 0.35$. Following Rudge et al. (2015), we use smoothing parameter values of $\lambda_s = \lambda_t = 0.5$.

Linearized inverse modeling of a revised and augmented inventory of 4018 river profiles yields a cumulative uplift history that is broadly consistent with previously published results (Figure 2; Lodhia et al., 2019; Paul et al., 2014; Rudge et al., 2015; Wilson et al., 2014). It is important to emphasize that, although we only recover significant cumulative uplift for the last 40 Ma, the calibrated Gilbert time is $\tau_G \sim 120$ Ma, which means no artificial limitation is placed upon the actual duration of cumulative uplift. That the recovered history falls between 40 Ma and the present day depends only upon the calibrated value of v. The residual root-mean-square (RMS) misfit between observed and calculated river profiles is $\chi_r < 2$. An ability to simultaneously fit over four thousand river profiles with a plausible uplift rate history suggests that the drainage networks are acting as tape recorders of external tectonic forcing (Figure 2). Notwithstanding this agreement between observed and calculated river profiles, the inverse algorithm makes a series of significant, and potentially limiting, assumptions that are open to debate. First, why should v, m, and n be treated as constants? What happens if they vary as a function of space and time? What is the relationship between rock erodibility and precipitation rate? Secondly, inverse modeling schemes assume that drainage planforms are invariant. What happens if migration of drainage divides and changes in catchment size occur?

2.2. Independent Validation of Calibrated Erosional Parameters

It is essential to provide independent justification for the assumption that $v = 3.62 \pm 1\ \mathrm{m}^{0.3}\ \mathrm{Ma}^{-1}$, which is inferred from Quaternary uplift rates along the coastline in the southern half of Africa, can be used across the continent during Neogene times. Figures 3a and 3b summarize locations and average uplift rates of outcropping marine rocks from the northern half of Africa and Arabia, which can be used to independently validate this assumption. These Cenozoic deposits contain definitively shallow marine fauna (Table 1). Observed and predicted uplift rates match within uncertainty for the last 40 Ma if the value of v varies between 3 and 4. Notwithstanding this validation, we acknowledge that the value of v could vary as a function of time and space within the bounds of uncertainty. Such variability could account for differences between predicted and observed uplift rates. However, the general agreement between observation and prediction suggests that such variability is minor, at least on the timescales and length scales of interest to us.

Elevated marine deposits are distributed across regions where the lithospheric plate appears to be much thinner than the thick cratonic keels of west and central Africa (Figure 3c). For example, geochemical modeling of major, trace and rare earth elements from basaltic rocks of the Neogene volcanic provinces of North Africa demonstrate that adiabatic melting of anomalously hot asthenosphere occurs as shallow as 60–80 km (Ball et al., 2019). One mechanism for reconciling this combination of thin lithosphere, magmatism, and elevated marine deposits is the thermal erosion of the lower lithospheric mantle (e.g., Davies, 1994; Gunnell et al., 2008). An isostatic argument is used to determine the relationship between present-day elevation, Z, and the change in lithospheric thickness from an initial value of a_o to a present-day value of a_1. We assume that the original lithospheric template sits at

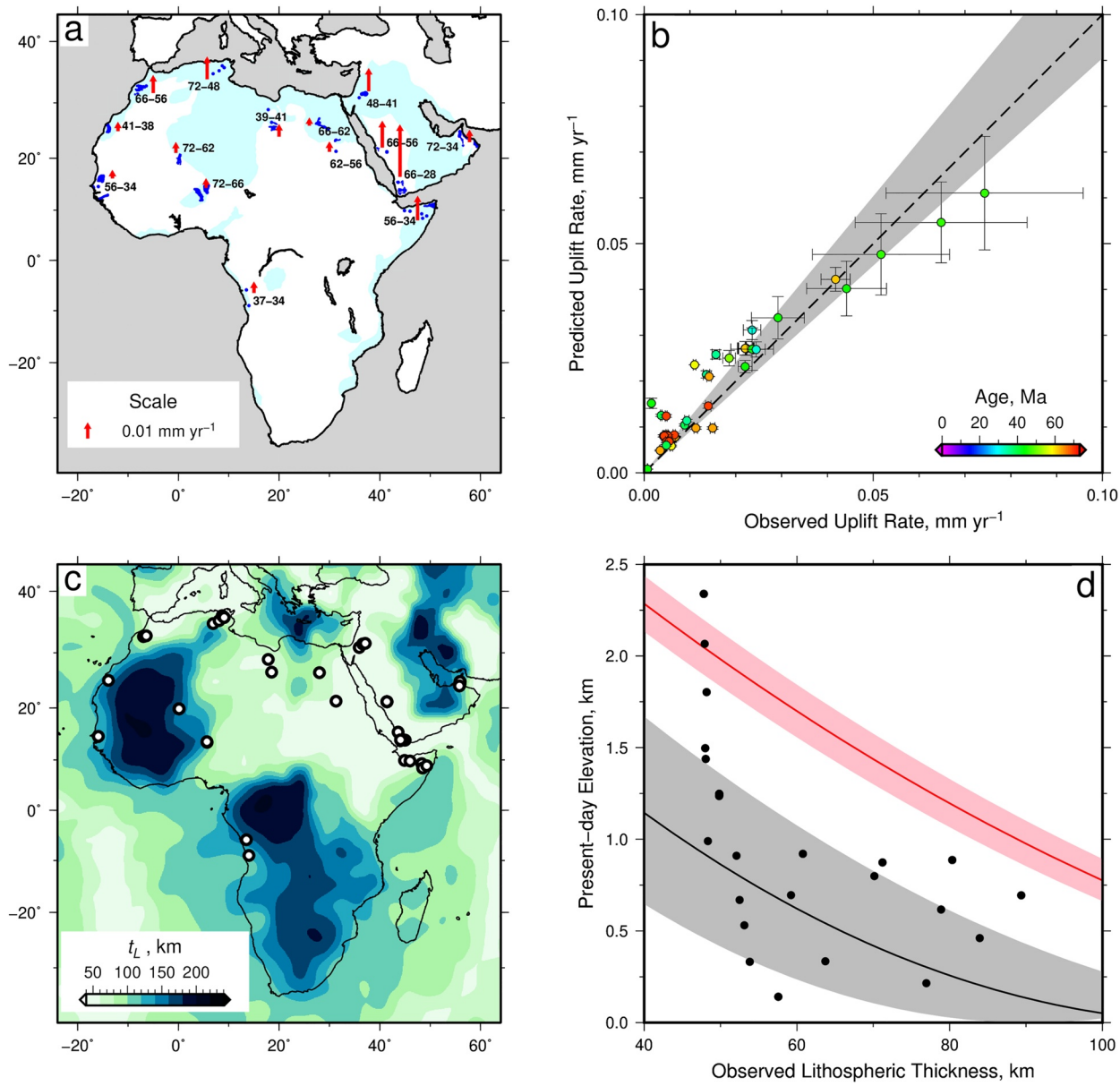

Figure 3. (a) Blue polygons = localities with Maastrichtian-Eocene marine fossils of well-known age and elevation used to test predicted uplift rates; red arrows = scaled uplift rate from range of marine fossils. (b) Predicted uplift rate from river profile inverse model that assumes $v = 3.62$ m$^{0.3}$ Ma^{-1}, plotted against uplift rates estimated from elevated marine fossils (Table 1; Uhen et al., 2019). Dashed line = 1:1 correlation; upper/lower edges of gray band = predicted uplift rates assuming $v = 4$ and $v = 3$, respectively. (c) Lithospheric thickness of Africa and Arabia calculated from surface wave tomographic model (Priestley et al., 2019). White circles = loci of marine fossil localities shown in panel (a). (d) Present-day elevation plotted as function of lithospheric thickness. Solid circles = elevations of marine sedimentary rocks for lithospheric thicknesses taken from panel (c); black line with gray band = predicted uplift of and its uncertainty from lithosphere that is initially 116 ± 26 km thick at zero elevation subsequently thinned to present-day value; red line with pink band = same for depleted cratonic lithosphere that is originally 220 ± 10 km thick.

sea level in isostatic equilibrium with a mid-oceanic ridge, in accordance with the parameter values shown in Table 2, and that the present-day lithosphere has not had sufficient time to regain thermal equilibrium (McNab et al., 2018). The relationship between Z and changing lithospheric structure is given by

$$Z = \left(\frac{\alpha T_1}{1-\alpha T_1}\right)\left[\left(\frac{a_1 - a_\circ}{\alpha T_1}\right)\left(1 - \frac{\rho_m^*}{\rho_m}\right) + (a_\circ - a_1) + \frac{\rho_m^*}{\rho_m}\left(\frac{a_1^2}{2a_\circ} - \frac{a_\circ}{2}\right)\right] \quad (9)$$

Table 2
Parameters Used in Isostatic Calculations

	Symbol	Parameter	Value	Units
Mid-Ocean Ridge	t_w	Ridge depth	2.8	km
	t_{oc}	Oceanic crustal thickness	7.1	km
	$a - t_w - t_{oc}$	Oceanic asthenospheric thickness	-	km
	ρ_w	Water density	1.0	Mg m^{-3}
	ρ_{oc}	Oceanic crustal density	2.8	Mg m^{-3}
	ρ_1	Oceanic asthenospheric density	-	Mg m^{-3}
Continent	t_c	Continental crustal thickness	40	km
	a_0	Lithospheric template thickness	-	km
	a_1	Modern lithospheric thickness	-	km
	ρ_c	Continental crustal density	2.8	Mg m^{-3}
	ρ_2	Continental lithospheric density	-	Mg m^{-3}
	ρ_3	Thinned lithospheric density	-	Mg m^{-3}
	ρ_m^*	Reference depleted mantle density	-	Mg m^{-3}
General	ρ_m	Reference mantle density	3.33	Mg m^{-3}
	A	Thermal expansion coefficient	3.3×10^{-5}	°C^{-1}
	T_1	Temperature at base of column	1,340	°C

where T_1 is the asthenospheric temperature, α is the thermal expansion coefficient, and ρ_m and ρ_m^* are the reference densities of mantle and of depleted mantle, respectively (see Table 2 for parameter values).

Figure 3d shows the relationship between Z and observed (i.e., present-day) lithospheric thickness for two alternative initial lithospheric templates. The first template consists of lithosphere which has reference crustal and mantle densities of 2.80 and 3.33 Mg m^{-3}, respectively. Phanerozoic African lithosphere away from cratons has an average crustal thickness of 33 ± 3 km, according to the continent-wide compilation of Globig et al. (2016). These values yield a starting lithospheric thickness of $a_\circ = 116 \pm 26$ km that sits at sea level. The second template consists of cratonic lithosphere characterized by depleted mantle (i.e., $\rho_m^* = \rho_m - 0.02$ Mg m^{-3}; Crosby et al., 2010). The cratonic lithosphere has an average crustal thickness of 40 ± 1 km, which yields a starting lithospheric thickness of $a_\circ = 220 \pm 10$ km that sits at sea level. Our results suggest that the observed and predicted elevation above sea level of Cretaceous-Paleogene marine deposits broadly agree if Phanerozoic (rather than cratonic) lithosphere is thermally eroded during Neogene times.

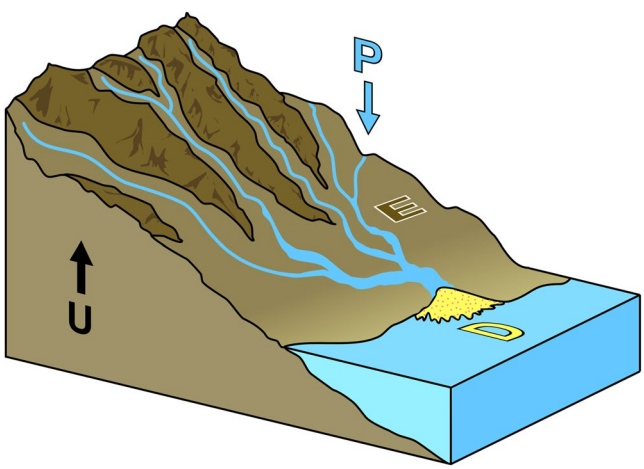

Figure 4. Schematic cartoon showing key elements of landscape evolution. *U*, *P*, *E*, *D* refer to regional uplift, precipitation, landscape erosion and offshore deposition that vary as function of time and space.

3. Landscape Simulations

Dynamic landscape simulations (i.e., forward models) can be used to test the key assumptions that underpin the inverse modeling of river profiles. These simulations now permit the interplay between uplift, precipitation, erosion, and deposition to be carefully investigated (Figure 4). Stream power and erosional diffusivity are used to model dynamic aspects of drainage that include hillslope processes, channel and divide migration, bedrock erodibility, and variable precipitation. A range of studies have exploited forward landscape simulations to investigate the response of landscapes to tectonic forcing (Braun et al., 2013, 2014; Ruetenik et al., 2016). Here, we carry out closed-loop modeling (also known as twin experimentation) to investigate the robustness of assumptions made by inverse models. First, an uplift rate history is used as the forcing mechanism for a given landscape simulation. Different uplift rate histories can be selected (Supplementary Information). Second, synthetic river profiles extracted from the calculated fluvial landscape are

inverted to recover a cumulative uplift history. Finally, the original and recovered uplift histories are compared. In this way, combinations of forward and inverse models are used to probe the influence of some, but not all, complicating factors that include divide migration and variable precipitation. A significant goal of closed-loop modeling is to assess the reliability of existing inverse modeling algorithms.

Here, we use the Badlands algorithm developed by Salles and Hardiman (2016), which is compared with the Landlab algorithm of Hobley et al. (2017). These two landscape simulators represent the fluvial erosion of a landscape in similar, but not identical, ways. For example, channel and hillslope development is parameterized on a Voronoi grid in an explicit manner that responds to an uplift history in accordance with a variety of erosional laws. Channelization spontaneously emerges as a response to small perturbations of the calculated land surface that arise from the discretization of uplift history (Smith & Bretherton, 1972). In the Badlands algorithm, sedimentary flux and deposition are calculated by assuming conservation of water and eroded sediment. The Badlands algorithm describes the evolution of an eroding landscape using

$$\frac{\partial z}{\partial t} = -\nabla.\mathbf{q_s} + U(x, y, t). \tag{10}$$

In this equation, $-\nabla.\mathbf{q_s}$ represents the depth-integrated volumetric flux out of a given cell per unit area. It is assumed that

$$\mathbf{q_s} = \mathbf{q_r} + \mathbf{q_d}, \tag{11}$$

where $\mathbf{q_r}$ and $\mathbf{q_d}$ represent mass transport caused by channel erosion and hillslope diffusion, respectively (Salles & Hardiman, 2016). Following Whipple and Tucker (1999), the stream power equation is used to characterize channel erosion such that

$$-\nabla.\mathbf{q_r} = -\upsilon(PA)^m\nabla z, \tag{12}$$

where ∇z is the topographic gradient between a given cell and its neighbors. A represents the contributing drainage area, which is a proxy for discharge through a given cell, and P is precipitation that can vary as a function of space and time. Note that discharge is explicitly calculated. Water and sediment are conserved and no threshold for the entrainment of sediment is applied. The component of mass flux out of a given cell generated by hillslope processes is approximated by a diffusive term that depends linearly upon topographic curvature (Braun et al., 2001; Dietrich et al., 1995; Fernandes & Dietrich, 1997). In the Badlands algorithm, this interfluvial erosion is parameterized using

$$-\nabla.\mathbf{q_d} = -\kappa(\nabla^2 z) \tag{13}$$

where κ is erosional diffusivity.

The Landlab toolkit was developed by Hobley et al. (2017) as part of a software package that includes gridding tools, stream power erosion models and hillslope creep processes. For comparison, we have combined a range of tools that implement physical processes similar to those used by the Badlands algorithm. Component tools include linear diffusion of off-channel topography based on the approach of Culling (1963), stream power erosion using the implicit scheme of Braun and Willett (2013), as well as a single direction convergent flow-routing scheme, which closely resembles that employed by the Badlands algorithm (Salles & Hardiman, 2016). The RasterModelGrid class is used to construct the regular grid for any given uplift rate history. Both algorithms are set up on grids with identical node distribution in (x, y) space, although Badlands employs Delaunay triangulation to connect nodes. Note that regular and irregular grids are not always free of artifacts with regard to flow-routing prediction. Once gridding, flow routing, and erosional parameters are selected, each landscape simulation is run using the cumulative uplift history of Africa and Arabia that was previously calculated by inverse modeling.

Given the distribution of marine strata and laterite deposits, we assume that the initial topography of the forward models can be set to zero at 40 Ma (i.e., channelization is solely a function of tectonic forcing and not a function of initial noise). The present-day shoreline and bathymetry are fixed using the modern configuration. We recognize that these assumptions are significant ones and alternative schemes have also been thoroughly investigated (see Figures S6 and S7 of Supporting Information S1). Calculated landscapes and drainage patterns are robust to noisy initial topographies with amplitudes < 500 m. It is important to point out that the prior existence of an

Table 3
Parameters Used in Comparative Tests of Badlands and Landlab Codes

Symbol	Description	Value	Units
v	Advective constant	3.62×10^{-6}	$m^{1-2m}\ yr^{-1}$
m	Erosional constant/exponent	0.35	-
n	Erosional constant/exponent	1.0	-
κ	Erosional diffusivity	2.0×10^{-15}	$m^2 yr^{-1}$
P	Precipitation rate	1.0	$m\ yr^{-1}$
N_p	Number of vertices in model	367, 211	-
I_x	Model resolution in x direction	15.0	km
I_y	Model resolution in y direction	15.0	km
t_{max}	Total model run time	42.050	Ma
t_{int}	Output interval	0.4205	Ma

Note. Self-consistent parameter values were selected and tectonic forcing is identical.

elevated plateau across southern Africa at 40 Ma is incompatible with our calibrated values of v and m (see e.g., Baby et al., 2019; Doucouré & de Wit, 2003; Guillocheau et al., 2012; Stanley et al., 2021; Tinker et al., 2008; Wildman et al., 2016). Our approximation of the initial state of the African and Arabian landscapes and coastlines is supported by geologic observations, which suggest that continental relief was subdued during Paleogene times (i.e., 60–30 Ma). The most valuable observations include the spatial distribution of Late Cretaceous to Oligocene marine deposits and Eocene lateritic and bauxitic surfaces together with an absence of clastic deposition at major deltas (Figure 1). During the Cenozoic Era, there has been relatively little overall change in the precise locus of the African paleocoastline. This stability probably reflects the fact that the continental shelves around Africa are comparatively narrow. The paleobathymetric history of oceanic floor abutting these shelves is poorly constrained but, in any event, only has a minor bearing on the landscape simulations presented here.

3.1. Comparative Tests

An important goal is to investigate whether different simulations can reproduce an observed landscape for constant values of v and m. Cumulative uplift history is interpolated onto a 15 × 15 km grid and each simulation is run for a duration of 40 Ma. A minor exponential tail of 2 Ma is used to mitigate the effect of a discontinuity generated by the sharp onset of regional uplift due to truncation of the input cumulative uplift history at 40 Ma. Initially, we assume that $v = 3.62\ m^{0.3}\ Ma^{-1}$, $m = 0.35$, and $P = 1\ m\ yr^{-1}$ (see Table 3 for other parameter values). Although Badlands can track sedimentary flux, the implementation of Landlab that we exploit does not specifically include sediment routing and deposition (e.g., Shobe et al., 2017). Consequently, these comparative tests do not include the effects of deposition.

Badlands and Landlab simulations can reproduce the general features of African and Arabian landscapes, with average misfit values per node of 222 and 225 m (i.e., cumulative RMS misfit values of 11.1 and 11.3), respectively (Figure 5). These simulations exhibit rapid Neogene topographic growth as a consequence of the external tectonic forcing that has been applied. For the Badlands simulation, the average misfit between observed and calculated topography in most regions is <200 m (Figure 5d). Significant negative misfit values occur along the length of the East African Rift between Ethiopia and South Africa. This mismatch partly reflects the fact that shorter wavelength features associated with rifting and magmatism are not recovered. Heights of major volcanic swells (e.g., Hoggar, Tibesti) and of predominantly amagmatic domes (e.g., Angola, Namibia, South Africa) are systematically underpredicted by 100–300 m. In both instances, an inability to match these elevations reflects the considerable degree of spatial and temporal damping employed during inverse modeling of river profiles. It also reflects the fact tectonic forcing was generated by inverse modeling of river profiles which are necessarily less elevated transects of a given landscape and the fact that ~100 m of regional uplift was recovered by inverse modeling prior to 40 Ma in some locations. Further north, there is a significant misfit between observed and predicted topography for the Atlas Mountains. Note that underprediction of topography along the northeastern fringes of the simulation is an erosional artifact generated by the boundary condition.

Figure 6 shows how drainage divides migrate as a function of space and time for different regions of the Badlands simulation. In both cases, drainage divides are established where short-reach catchments drain directly into the adjacent ocean abut larger catchments that drain toward the other side of the continent. Despite catchment asymmetry, these drainage divides migrate at rates of ~0.01 m yr^{-1} or less, in agreement with the results of some, but not all, landscape modeling studies (Braun, 2018). Within the continental interior, drainage divides are relatively more stable. Testing of alternative uplift histories demonstrates that artificial pinning of drainage divides is not a feature of this model configuration. Equally, divides are not preconfigured by matching present-day topography nor are they unduly static compared with divides generated by landscape simulations that employ finer spatial resolution (Figures S8–S16 of Supporting Information S1). The Landlab algorithm yields similar results (Figures 5e–5g).

These landscape simulations yield drainage planforms that are different in many respects from that of Africa. There are usually three principal catchments. A significantly enhanced "Niger" drainage catchment reaches the

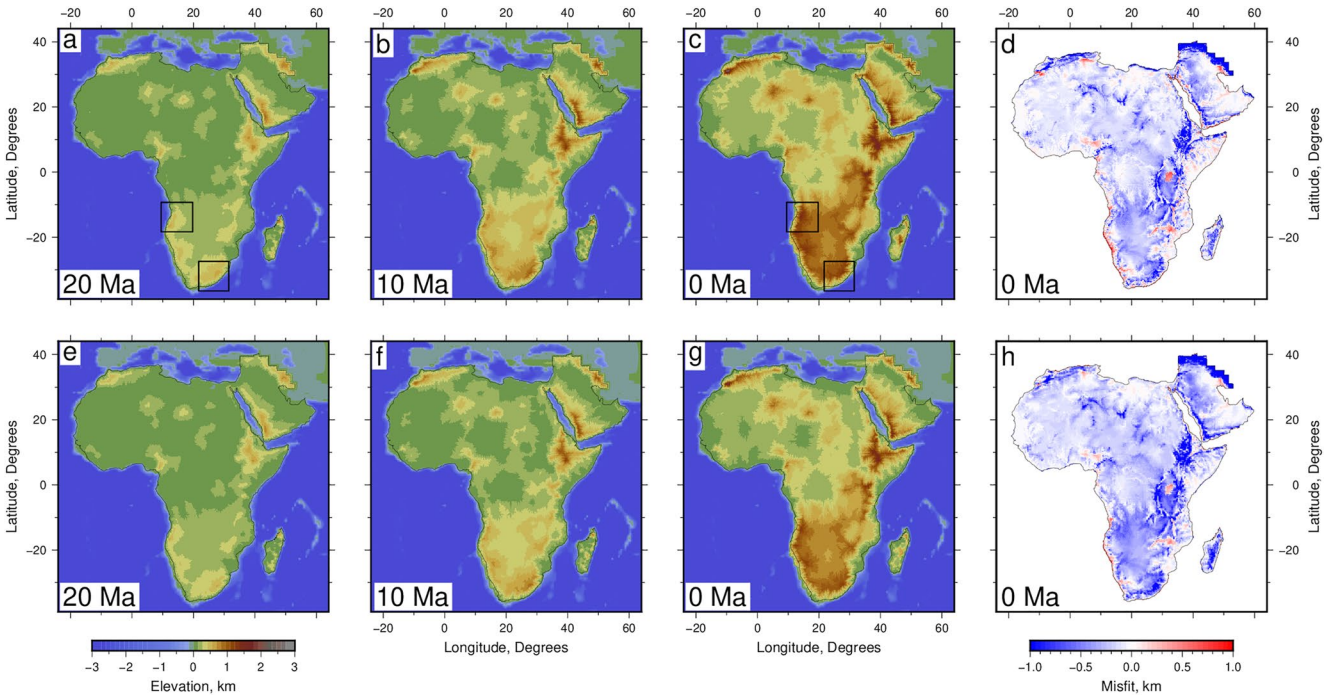

Figure 5. Comparative testing of landscape models. (a) Synthetic African landscape calculated at 20 Ma using Badlands algorithm of Salles and Hardiman (2016) subject to cumulative uplift history shown in Figure 2 and without sedimentary deposition. Boxes show location of zooms from Figure 6. (b) Same at 10 Ma. (c) Same at present day. (d) Map showing difference between predicted and observed African landscape. RMS misfit = 11.1, average misfit = 222 m and volumetric misfit = 7.6×10^6 km^3. (e–h) Same using Landlab algorithm of Hobley et al. (2017). RMS value = 11.3, average misfit = 225 m and volumetric misfit = 7.7×10^6 km^3.

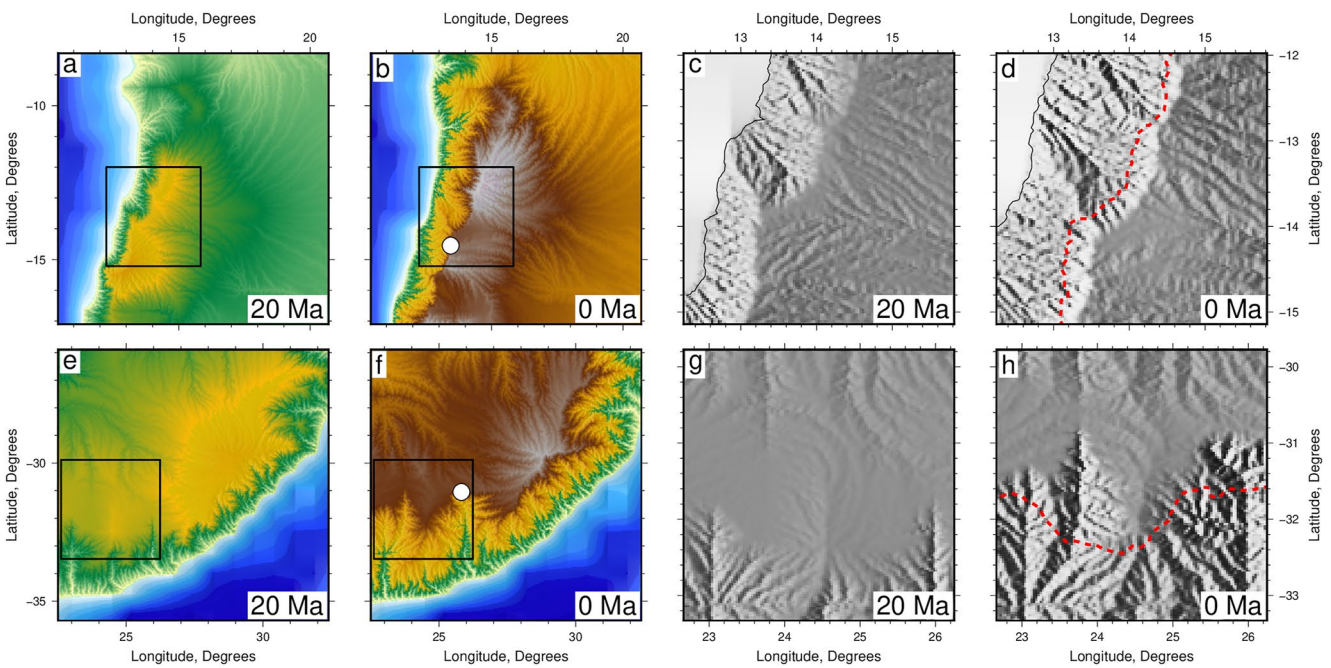

Figure 6. (a) Zoom showing synthetic landscape calculated at 20 Ma using Badlands algorithm for portion of West Africa corresponding to Bié dome (see Figure 5a for location). (b) Same at 0 Ma. Box shows location of detailed portion from panel (c) (c) Detailed portion of panel a where shaded relief highlights drainage divide. (d) Detailed portion of panel (b) Red dashed line = locus of drainage divide shown in panel c at 20 Ma. (e)–(h) Same for portion of southern Africa (see Figure 5a for location).

coast slightly to the west of the actual Niger delta. Simulations also predict the existence of "Nile" and "Congo" catchments that drain into the eastern Mediterranean Sea and into the Atlantic Ocean, respectively. Both simulations predict that some proportion of the African interior undergoes internal drainage. This prediction is a consequence of omitting to simulate sedimentary deposition. Even though water flow routed into any pits or depressions is tracked (i.e., where specific grid cells are bordered by cells of greater elevation), sediment is not actually deposited. Thus water levels do not increase enough to overflow particular basins (Braun & Willett, 2013; Salles & Hardiman, 2016). It is evident that the Landlab simulation underpredicts the most elevated regions by 0.5–1 km (e.g., Ethiopian highlands, sub-equatorial Africa; Figure 5h). These discrepancies partly reflect differences in the implementation of flow-routing for these two algorithms (Braun & Willett, 2013). For example, Badlands predicts that internal drainage occurs within central southern Africa whereas Landlab routes most of this drainage northward into an oversized "Congo" catchment and basin. Differences in flow routing account for significant misfits along the northern edge of the southern African plateau (Figures 5d and 5h). It is encouraging that both simulations recreate the fluvial landscapes of Africa and Arabia reasonably well, despite the fact that they are forward models whose drainage patterns have not been preconfigured. Their similarity to each other, and to the present-day landscape, is likely to be a direct consequence of tectonic forcing, which sets the pace for fluvial erosion. This forcing probably plays a significant role in determining locations of drainage divides.

3.2. Simulation of Catchments, River Profiles and Flux Histories

The Badlands algorithm can be used to predict sedimentary flux histories along the continental margin. This functionality enables observed and calculated flux to be compared, which constitutes an independent test. Comparative tests show that the Badlands and Landlab models have similar run times but, when the sediment routing functionality is included, the run time of the Badlands algorithm increases by up to one order of magnitude. For this reason, we use a horizontal resolution of 15 km to facilitate parameter testing, although higher resolution runs have also been carried out for benchmarking purposes (Figures S17–S19 of Supporting Information S1). For a 15×15 km grid, Badlands takes up to 15 min to run on a single core of an Intel® Core™ i5 3.2 GHz processor if sediment deposition is not tracked. This run time increases fourfold if sediment routing and tracking are included. Note that sediment flux is only tracked to simulate deposition and that its inclusion does not influence erosion rate *per se*.

A Badlands simulation that includes sediment routing and deposition for constant precipitation is shown in Figure 7. The calculated present-day drainage planform is largely unchanged (Figures 5c and 7a). Residual misfit between observed and predicted topography indicates that there is less than ±200 m difference across the bulk of Arabia and the northern half of Africa (Figure 7b). As before, the elevation of the Ethiopian Plateau and of the East African Rift is underpredicted by up to 500 m. Elevations of short wavelength swells are also not adequately resolved. Significantly, the inclusion of sediment routing and deposition, which enables pits and depressions to be infilled, yields a present-day drainage planform with drainage divides that better approximate the observed planform (Figure 7c). Predicted drainage planform shows that three major catchments broadly correspond to the "Nile", "Niger", and "Congo" rivers and their tributaries. Similarities and differences between observed and calculated drainage basins provide useful insights. Although major planform reorganization occurs during the early stages of landscape simulation, we find that individual catchments and the modern drainage divides are very rapidly established and subsequently maintained (Figure 7c). Migration rates of these simulated divides are $O(10^{-1} - 10^{1}$ mm yr$^{-1})$, which are corroborated by a combination of limited field observations and of fluvial modeling (see, e.g., Braun, 2018; Salles & Hardiman, 2016, and references therein; van der Beek & Braun, 1999; van der Beek et al., 2002).

Simulated "Niger" and "Nile" catchments superficially resemble their present-day counterparts and there are significant differences. Both observed and simulated "Niger" catchments include tributaries that drain eastward from the Fouta Djallon plateau. These tributaries then turn southward to meet rivers that drain from the southern flank of the Hoggar and Aïr swells and from the western edge of the Jos plateau before emerging at the coastline. Chardon et al. (2016) proposed that this planform has been stable since ~34 Ma. Note that the calculated "'Niger" catchment includes regions of internal drainage to the northwest and in the vicinity of Lake Chad. Goudie (2005) contends that overflow from the paleo-Lake Chad may have contributed to the ancient Niger catchment during wetter periods, even as recently as the Holocene times. West of the 'Niger' catchment, the landscape simulation predicts the existence of a "Senegal/Gambia" catchment, in general agreement with Chardon et al. (2016). The

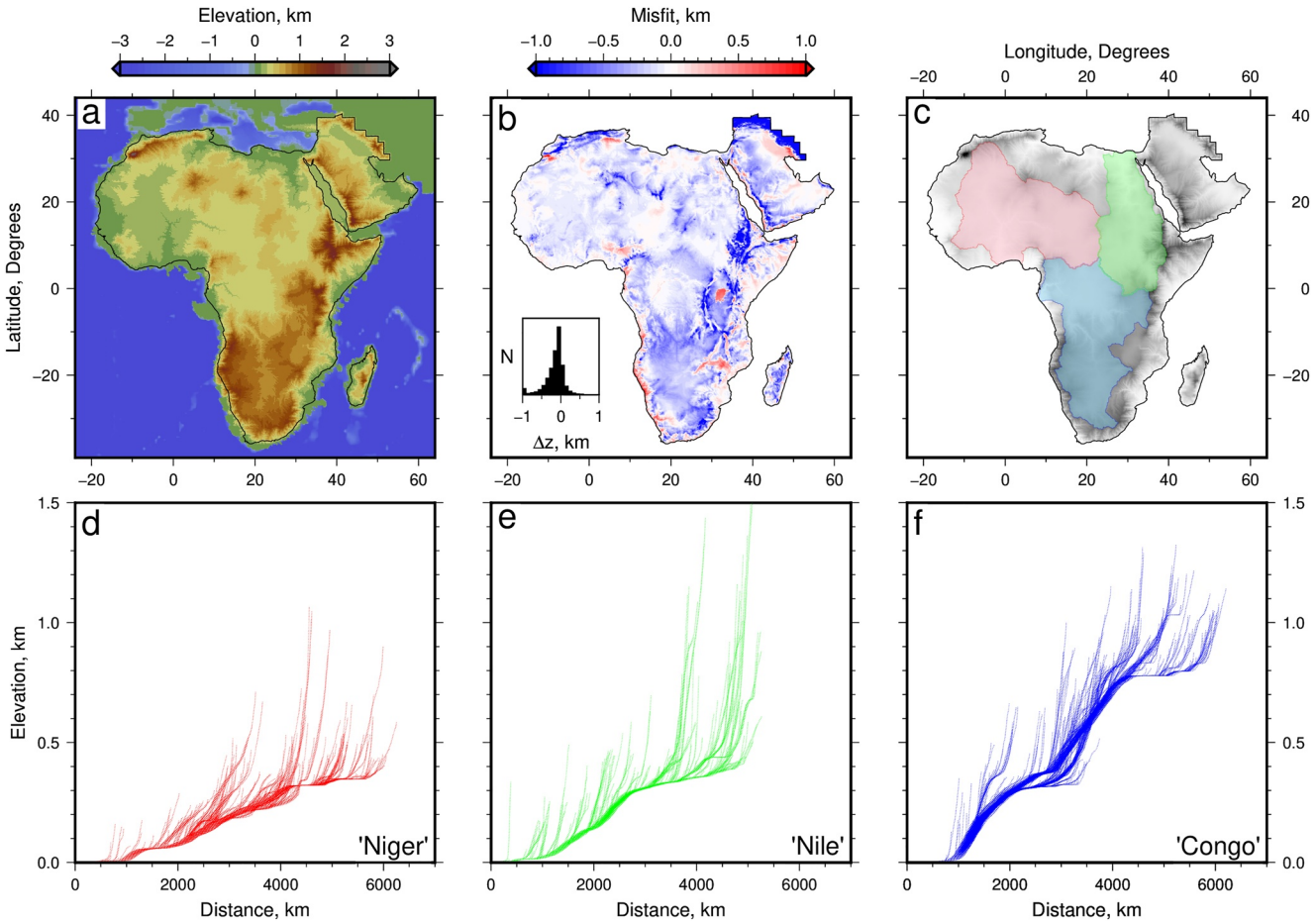

Figure 7. (a) Synthetic African landscape calculated at present day (i.e., 0 Ma) using Badlands algorithm of Salles and Hardiman (2016) subject to cumulative uplift history shown in Figure 2 and with sedimentary deposition. Erosional constants are taken from Rudge et al. (2015) for constant precipitation rate of 1 m yr^{-1}. (b) Map showing difference between predicted and observed African landscape. Inset panel shows histogram of differences between observed and simulated landscapes, in 100 m bins. RMS value = 10.5, average misfit = 210 m and volumetric misfit = 7.2×10^6 km^3. (c) Three main catchments identified using drainage distribution shown on panel (a) Red/green/blue polygons = 'Niger'/'Nile'/'Congo' catchments, respectively. (d)–(f) Synthetic river profiles for 'Niger', 'Nile' and 'Congo' catchments.

calculated "Nile" catchment crudely matches its modern planform, which may have progressively captured its southern reaches during Neogene times (Abdelkareem et al., 2012; Faccenna et al., 2019; Goudie, 2005).

Figure 7c shows that sub-equatorial Africa is dominated by a single "Congo" catchment. The calculated "Zambezi" and "Limpopo" catchments do not lie far from their actual positions along the southeast coast. Note that the "Zambezi" catchment is about half the size of the modern Zambezi catchment, which drains the Angolan highlands. Minor catchments are dotted along the coastline of East Africa, approximately matching the positions of the modern Tana, Ruvuma, Jubba, and Shebelle catchments. The most significant discrepancy between observed and calculated catchments concerns the Orange river. During the early stages of the landscape simulation, the northern portion of the "Orange" catchment is captured by an increasingly dominant "Congo" river. T. Partridge and Maud (1987), M. C. J. de Wit (1999), and Rouby et al. (2009) have proposed that the catchment of the Orange River was configured before 80 Ma and that it has subsequently remained stable. Since the cumulative uplift history used to carry out the simulation starts at 40 Ma, ancient antecedent drainage patterns are absent. Consequently, the nascent "Orange" and "Okavango" catchments are rapidly captured by the "Congo" system. The landscape simulation shown in Figure 7 yields a dynamic drainage network that clearly evolves through time. It includes escarpment retreat and changes in the catchment area, neither of which are parameterized in the much simpler inverse model (Figures S17–S19 of Supporting Information S1).

Longitudinal river profiles are extracted from the Badlands simulation using the in-built flow-routing algorithm (Figures 7d–7f; Braun & Willett, 2013). Principal channels and tributaries from the "Nile", "Niger", and

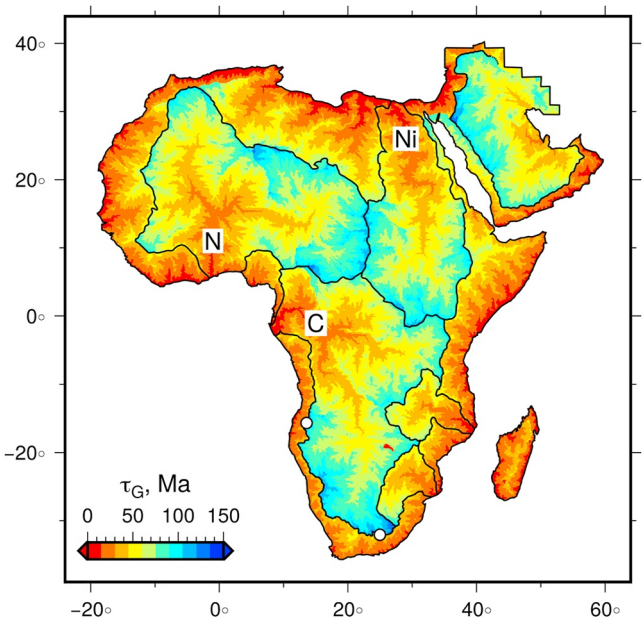

Figure 8. Landscape response time, τ_G, calculated for drainage network extracted from Badlands simulation for constant precipitation using Equation 6. Black lines = drainage divides; white circles = loci of τ_G disparities shown in Figure 6; N, Ni, and C = predicted 'Niger', 'Nile' and 'Congo' catchments.

"Congo" catchments have systematic and correlatable patterns of convex-upward knickzones that are reminiscent of those observed along African river profiles (Paul et al., 2014; G. G. Roberts & White, 2010). A significant question concerns the extent to which these recovered river profiles, which obviously differ from African river profiles, still preserve the spatial and temporal pattern of cumulative uplift history. This question can be directly addressed by closed-loop modeling.

Figure 8 shows the landscape response time, τ_G, for the Badlands simulation. Figure 6 highlights two regions with significant τ_G excursions, where divide migration rates are measurable from the landscape simulation. Landscape response time is predicted to be ~67 Ma to the east of the prominent escarpment near "Angola" (Figure 6b), and ~27 Ma to the west. This contrast of a factor of ~2.5, combined with the spatio-temporal variation of regional uplift, produces an escarpment retreat rate of ~3 mm yr^{-1}. In southern Africa, predicted values of τ_G vary from ~86 Ma north of the escarpment to ~29 Ma south of the escarpment (i.e., a factor of ~3 difference). This difference results in a divided migration rate of 3.8 mm yr^{-1} (Figure 6f). Our recovered rates of migration are in broad agreement with upper bounds for escarpment retreat rates at drainage divides where substantial contrasts in τ_G occur (Braun, 2018).

3.2.1. Sedimentary Flux

The Badlands algorithm predicts sedimentary flux as a function of space and time. At the start of the landscape simulation, we assume the present-day coastal configuration, which is undoubtedly incorrect in detail and probably affects the precise location of each delta. Figure 9a shows the calculated sedimentary deposition at the present day, revealing that the coastline has migrated seaward during Neogene times to form a series of deltas. Significant sedimentary efflux is positioned close to the loci of known fluvial deltas.

Observed and predicted sedimentary flux as a function of time can be compared for individual deltas. Previously, the results of inverse modeling of suites of river profiles have been used to calculate the variation of sedimentary flux with time for particular deltas (see, e.g., Lodhia et al., 2019; Paul et al., 2014; Richards et al., 2016; Rodríguez Tribaldos et al., 2017; Stephenson et al., 2014). These rudimentary calculations are limited in several key respects. First, rock removal is calculated along rivers and selected tributaries alone, which ignores erosion along smaller channels and across interfluves. Second, drainage reorganization and divide migration are ignored. Third, erodibility along rivers and selected tributaries are assumed to be constant. By exploiting a more physically realistic sediment routing approach, Salles and Hardiman (2016) have addressed these limitations. Their approach considers the downhill translation of material in terms of a volumetric solid fraction. Transport of solid sediment through the drainage network is tracked to points of deposition at deltaic lobes. We calculate total volumetric flux into each delta through time but we do not aim to match the precise areal extent of observed deltas. Figure 9 summarizes the predicted sedimentary deposition as a function of space and time for constant precipitation. We are especially interested in the growth of deltas at the mouths of the "Nile", "Niger", and "Congo" rivers. In all three cases, the locations of observed and predicted deltas are in good agreement (Figures 9a–9c). Note that the predicted "Congo" delta can be regarded as a combination of the Congo and Ogooué deltas. Along the east coast of Africa, the predicted "Limpopo" and "Zambezi" deltas, together with minor deltas further north, have locations that are consistent with observed deltas. The eroded material is predicted to appear during Oligocene times, in general agreement with borehole information and with calibrated seismic reflection surveys (Lavier et al., 2001; Reijers, 2011; Rouby et al., 2011; Salman & Abdula, 1995). In the case of the "Nile" delta, sedimentary deposition is predicted to commence earlier than Miocene times (i.e., 15 Ma), as proposed by Sestini (1989). The predicted drainage of the Arabian peninsula suggests that a limited amount of material is eroded from minor catchments along the northeast margin of the Red Sea but that the bulk of sedimentary deposition is funneled through the Persian Gulf, in agreement with observation (Wilson et al., 2014).

Figures 9d–9f show predicted and observed sedimentary flux as a function of time for the "Nile", "Niger", and "Congo" catchments. To aid comparison, we have binned the predicted flux using the same time intervals

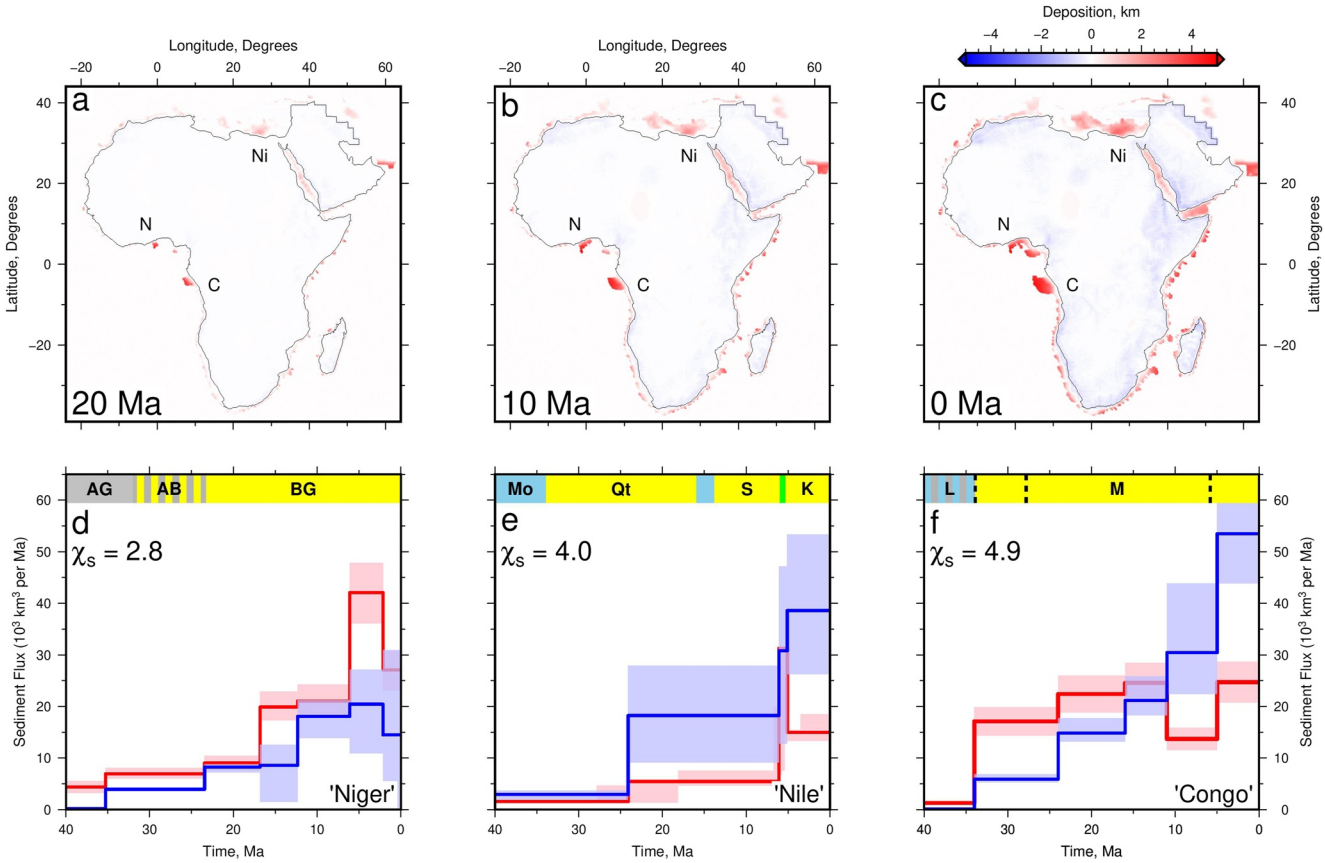

Figure 9. (a) Cumulative offshore deposition calculated at 20 Ma using Badlands algorithm. (b) Same at 10 Ma. (c) Same at present day. (d) Red line with pink band = observed sedimentary flux with uncertainty for Niger delta (Grimaud et al., 2017; Haack et al., 2000; Rouby et al., 2011); blue line with turquoise band = predicted sedimentary flux with uncertainty for 'Niger' delta; colored bar = stratigraphic template. AG = Akata Group (basinal and slope marine shales); AB = Agbada Group (alternating shales and deltaic sands); BG = Benin Group (deltaic sandstone); χ_s = RMS misfit between observed and calculated flux. (e) Red line with pink band = observed flux for Nile delta (Abdel Aal et al., 2001; Walford, 2003); blue line with turquoise band = predicted flux for 'Nile' delta; Mo = Mokattam Limestone (shelfal marine); Qt = Tineh and Qantara formations (Eonile sand/silt deposits); blue bar at ~15 Ma = Marmarica Limestone (reefal); S = Sidi Salem and Qawasim Formations (also Eonile sand/silt); green = Rosetta Formation (Messinian evaporites); K = Kafr El Sheikh and younger formations (deltaic sandstones/shale). (f) Red line with pink band = observed flux for Congo delta (Lucazeau et al., 2003); blue line with turquoise band = predicted flux for 'Congo' delta; L = Landana Formation (interbedded siltstone/shale/carbonates with low depositional rate); M = Malembo Formation (proximal turbidite deposits and deltaic sandstones); dashed lines = unconformities (Anka et al., 2009; Cole et al., 2000; Ismail et al., 2010; Reijers, 2011; Said, 1981).

as published estimates of Cenozoic sedimentary flux (Grimaud et al., 2017; Lucazeau et al., 2003; Rouby et al., 2011; Walford, 2003). Given the considerable uncertainties in accurately estimating sedimentary flux, observed and predicted volumetric flux for the 'Niger' delta broadly agree, despite the fact that flux predictions are predicated upon an uplift rate history that is heavily damped. A notable discrepancy is the underprediction of an observed peak of sedimentary flux during Pliocene times. This peak probably reflects an increase of regional uplift within the broader catchment, which includes the magmatic Hoggar swell. It could also be due to an increase in catchment area. Late Pliocene marine sedimentary cores suggest that the northern portion of the Niger basin became cooler and arider at ~2.8 Ma which could account for the post-Pliocene decrease (DeMenocal, 1995). Although the onset of observed and predicted flux for the 'Nile' delta approximately coincide, there is a substantial discrepancy between 25 and 8 Ma when predicted flux exceeds observed flux by nearly one order of magnitude. This overestimation may reflect easterly migration of the Nile delta during the Early Miocene times (Guiraud & Bosworth, 1999; Sestini, 1989). Observed flux estimates of Abu El-Ella (1990) and Abdel Aal et al. (2001) do not include this earlier western depocenter. At 8 Ma, both observed and predicted flux sharply increase which probably reflects regional uplift of the Ethiopian highlands (Faccenna et al., 2019). Finally, there is a significant discrepancy between observed and predicted flux for the "Congo" delta. Between 35 and 10 Ma, calculated flux underpredicts observed flux by a factor of five. The reasons for this discrepancy are unclear. The predicted depocenter of the "Congo" delta is located to the north of its actual location and is positioned closer to

the mouth of the modern Ogooué river. Analysis of the size of the Ogooué delta compared to the area and relief of its catchment suggest that the Congo river may have been discharged at this position during Early Neogene times (Droz et al., 1996; Karner & Driscoll, 1999; Lucazeau et al., 2003; Walford, 2003). Observed and predicted flux both increase within the last 5 Ma although the predicted flux is much greater, which could be the consequence of the catchment area has been concomitantly larger. This increase is probably associated with the growth of the Angolan dome and elevation of the margins of the Albertine Rift.

3.3. Precipitation Tests

Previously, we have assumed that the precipitation rate has a constant value of $P = 1$ m yr^{-1} within the stream power formulation given by Equation 12. Now, we wish to systematically investigate the effects that spatially and temporally varying values of $P(x, y, t)$ have on knickzone celerity, landscape evolution, and flux predictions. As before, the Badlands algorithm is externally forced with an uplift rate history determined by river profile inverse modeling. A series of landscape simulations are then carried out for different distributions of P. In the Badlands algorithm, variable precipitation is implemented by combining precipitation, P, and upstream drainage area, A, within the discharge proxy of Equation 12. This simplified formulation is exploited by Ferrier et al. (2013), Roe et al. (2002), Royden and Perron (2013), and Wu et al. (2006). It is then straightforward to simulate the effects of variable precipitation as a function of space and time with a view to quantifying the influence of $P(x, y, t)$ upon calculated river profiles and sedimentary fluxes. We acknowledge that more sophisticated formulations that include the effect that precipitation has upon grain size dynamics and erosive thresholds could be investigated but we think that these additions are unlikely to significantly alter our conclusions. In the Supporting Information, we investigate simulations where erodibility and precipitation rate are coupled (Figures S20–S25 in Supporting Information S1; Murphy et al., 2016).

3.3.1. Precipitation as Function of Space

Since the Late Cretaceous times, the spatial distribution of precipitation across Africa is determined by latitudinally-controlled climatic belts (i.e., Hadley cells and the position of the inter-tropical convergence zone; Parrish et al., 1982). Northward continental drift of Africa during Cenozoic times was slow and has only had a modest effect on the position of these Hadley cells over Africa (Frierson et al., 2007). The present-day distribution of precipitation shows that the highest rainfall is centered on the equator where a ten-year average value peaks at 2 m yr^{-1} (Matsuura & Willmott, 2012, Figure 10). This peak value drops by one order of magnitude at latitudes of $\pm 30°$. Here, we represent this latitudinal pattern by fitting an analytical relationship to the average north-south change in precipitation and by assuming that this variation does not change as a function of time.

Results of a landscape simulation with spatially varying precipitation are shown in Figure 11. The predicted present-day landscape is visually similar to that generated under constant precipitation conditions. Formal misfit values between constant and spatially variable precipitation show that the most significant differences occur in the extreme north and south of Africa. A reduction of precipitation results in low average discharge which generates a landscape that is less deeply incised by up to 1 km (Figures 11b). Predicted river profiles for the "Nile", "Niger", and "Congo" catchments are superficially similar to those obtained under constant precipitation conditions (Figures 11e–11g). In all three cases, the principal knickzones have significant horizontal displacements. For example, knickzones in the 'Niger' catchment generated under spatially variable precipitation conditions are offset toward zero (i.e., the coastline) by up to ~500 km because this catchment samples a region with lower average precipitation rates. In contrast, principal channels and tributaries of the "Nile" and "Congo" catchments are horizontally offset away from zero toward the drainage divide by ~500 and ~1000 km, respectively. Differences in horizontal offset for these two catchments reflect the fact that the "Congo" catchment has higher average precipitation. Despite systematic differences, a coherent pattern of knickzones is recorded in all three catchments, which probably reflects the primacy of external tectonic forcing compared with spatially variable precipitation.

Spatially variable precipitation leads to significant changes in the predicted sedimentary flux for the "Nile", "Niger", and "Congo" catchments (compare Figures 9 and 12). Regardless of precipitation, the three predicted deltas are located in almost exactly the same places at 20, 10, and 0 Ma (Figures 12a–12c). Thus the spatial variation of precipitation has a little discernable effect on the catchment outlet. However, increased precipitation close to the equator and reduced precipitation at higher latitudes will undoubtedly affect sedimentary flux as a function of time. As expected, predicted fluxes of the "Nile" and "Niger" catchments are reduced since their catchments now

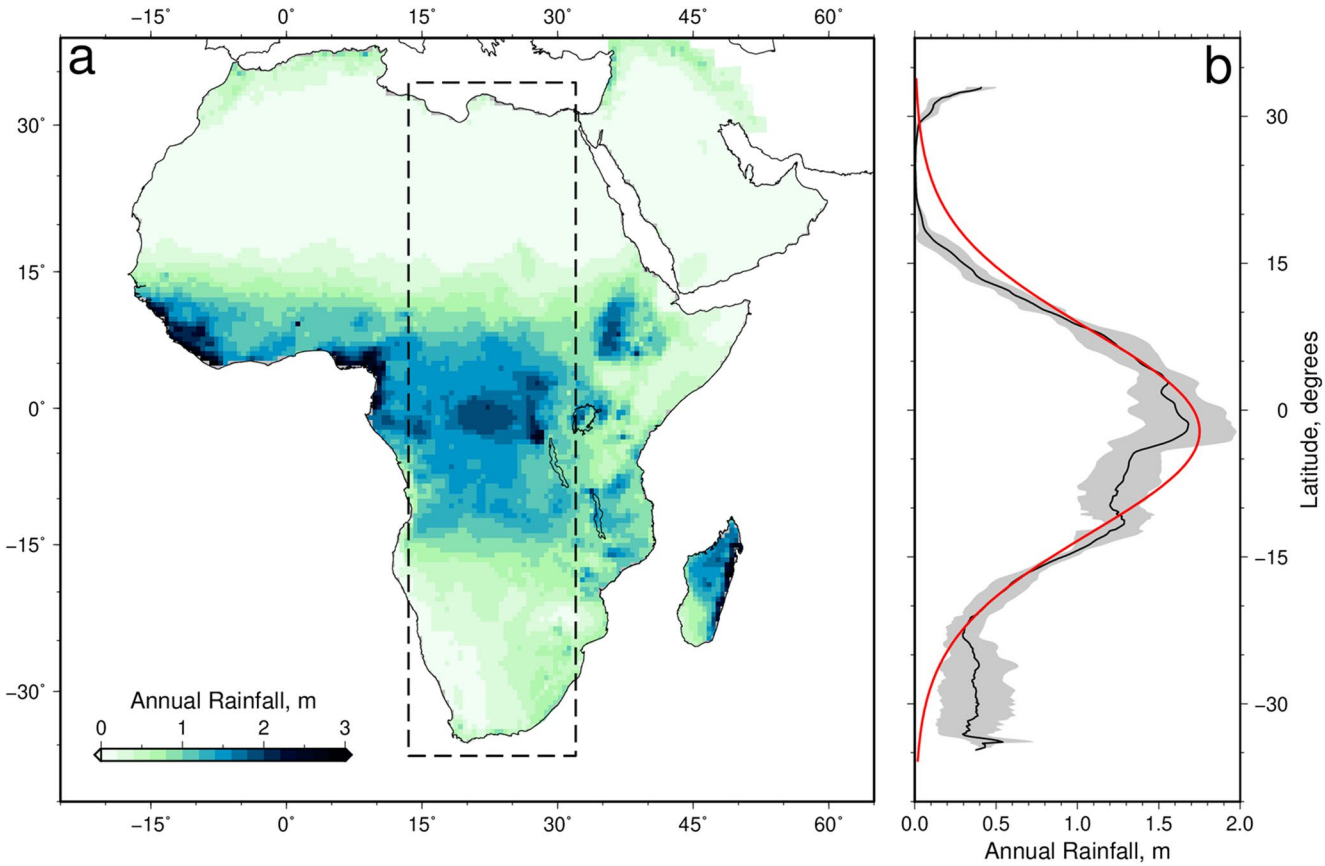

Figure 10. (a) Average annual precipitation for Africa and Arabia between years 2000 and 2010 (Matsuura & Willmott, 2012). Dashed box = region within which average precipitation rate is calculated. (b) Black line with gray band = average precipitation rate for box shown in panel a ± 1σ; red line = best-fitting Gaussian curve.

sample drier hinterlands where average precipitation has been reduced compared with the constant precipitation case. In contrast, the "Congo" catchment samples a much wetter hinterland, and this difference is clearly manifest in the predicted sedimentary flux, which better matches the observed flux between 35 and 10 Ma (Figure 12f). This improvement is probably a result of wetter simulated conditions in the vicinity of the East African Rift, the southwestern flanks of which are drained by the observed and simulated Congo catchments. Early cumulative uplift occurs here that acts to increase discharge through westward-draining tributaries of the Congo river. As a consequence, Eocene/Oligocene sedimentary flux is enhanced.

3.3.2. Precipitation as Function of Space and Time

Variation of precipitation as a function of latitude alone is both an unrealistic, and an overly severe, test of closed-loop modeling. The African climate has obviously varied through Neogene times and the modern pattern of negligible precipitation rates between ±20° and ±30° is unlikely to have persisted without interruption over this period. It is more reasonable to expect precipitation to be a function of both space and time. Paul et al. (2014) carried out a series of one-dimensional inverse models of river profiles that permitted precipitation to vary periodically as a function of time. They showed that the recovered uplift rate history was largely unchanged provided that $P(t)$ varied with periods ≤1 Ma. Similar results were obtained for Arabia and for Central America by Wilson et al. (2014) and by Stephenson et al. (2014), respectively. These precipitation tests suggest that the ability of inverse models to match individual river profiles is not significantly influenced by $P(t)$ unless it varies with periodicities of, say, $O(10)$ Ma. This conclusion is not surprising because the solution of the stream power equation takes the form of an integral. Here, we wish to generalize this one-dimensional analysis by carrying out landscape simulations with $P(x, y, t)$. Our goal is to investigate the relative importance of tectonic and precipitation forcing. In these simulations, it is important to note that spatial and temporal variations of precipitation affect not just channel erosion but interfluvial regions and hillslopes as well.

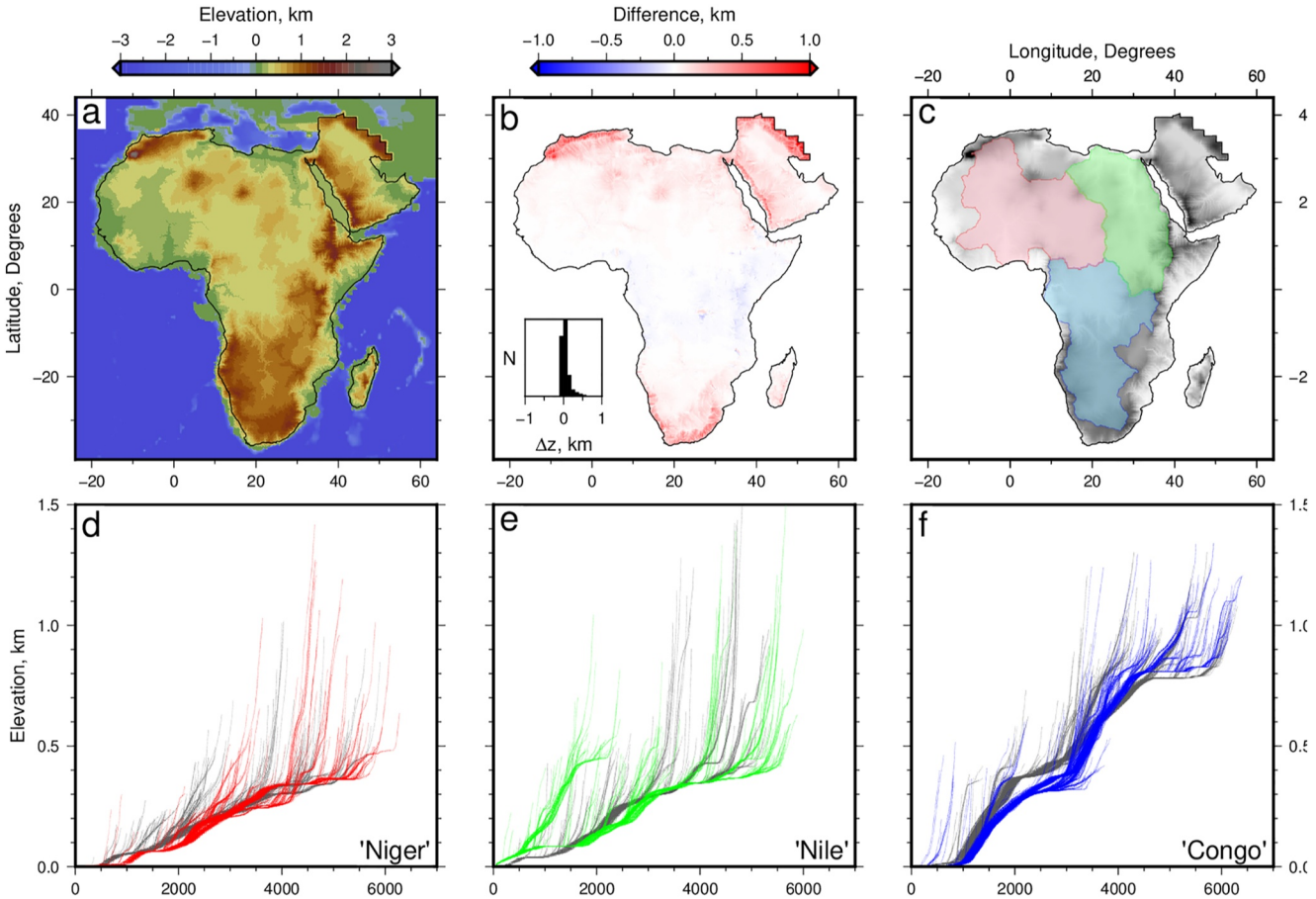

Figure 11. (a) Present-day synthetic African landscape calculated using Badlands algorithm of Salles and Hardiman (2016) subject to cumulative uplift history shown in Figure 2 where precipitation rate varies as a function of latitude (Figure 10). (b) Difference between synthetic landscapes calculated using latitudinally variable and constant precipitation rate. RMS value = 3.0, average misfit = 59 m, and volumetric misfit = 2.0×10^6 km^3. Inset panel shows histogram of differences between observed and simulated landscapes, in 100 m bins. (c) Red/green/blue polygons = 'Niger'/'Nile'/'Congo' catchments, respectively. Gray shading = synthetic landscape shown in panel (a) (d)–(f) Red/green/blue lines = synthetic river profiles for 'Niger', 'Nile' and 'Congo' catchments for latitudinally variable precipitation rate; gray lines = synthetic river profiles for constant precipitation (Figure 7).

A range of sedimentologic and paleontologic observations—fluvial and lacustrine facies distributions, freshwater algal occurrences, vertebrate and invertebrate morphology, paleosol analysis, and archeologic studies—suggest that, as recently as Pleistocene and Holocene times, arid regions of northern and southern Africa experienced precipitation rates up to 0.5 m yr^{-1} higher than modern values (e.g., Armitage et al., 2007; Brook et al., 2011; DeMenocal et al., 2000; Gasse, 2000; Kröpelin & Soulié-Märsche, 1991; Larrasoaña et al., 2013). Similar observational evidence shows that wet periods existed during Neogene times (e.g., Coetzee, 1980; Coetzee & Rogers, 1982; DeMenocal, 1995; Drake et al., 2008; Feakins, 2013; Griffin, 2002; van Zinderen Bakker & Mercer, 1986). Marine records of eolian dust show that African climate variability tends to be dominated by changes in insolation caused by orbital forcing. Before ~2.8 Ma, orbital precession with cycles that are 19–23 ka long exerted the dominant influence on the African climate cycle. Between 2.8 and 1.0 Ma, climate variability was principally controlled by obliquity. During the last 1 Ma, the development of large amplitude glacial cycles has shifted African climate cycles toward a 100 ka periodicity controlled by orbital eccentricity, although the effects of shorter period orbital forcing are still evident (DeMenocal, 1995). In southern Africa, sedimentary records from the Pretoria Saltpan suggest that the 23 ka cycle has been dominant over the last 200 ka (T. C. Partridge et al., 1997). These cyclical variations act to moderate the precipitation rate which consequently fluctuates through time. Following Paul et al. (2014), we assume that precipitation varies sinusoidally and imposes a variability between 0 and 1 m yr^{-1} as a function of time onto the observed latitudinal variation over the duration of landscape simulation. Although precipitation varies on orbital timescales that are generally shorter than 100 ka, we follow Paul et al. (2014) and choose this value as a minimum periodicity in order to ensure that these precipitation tests are sufficiently severe.

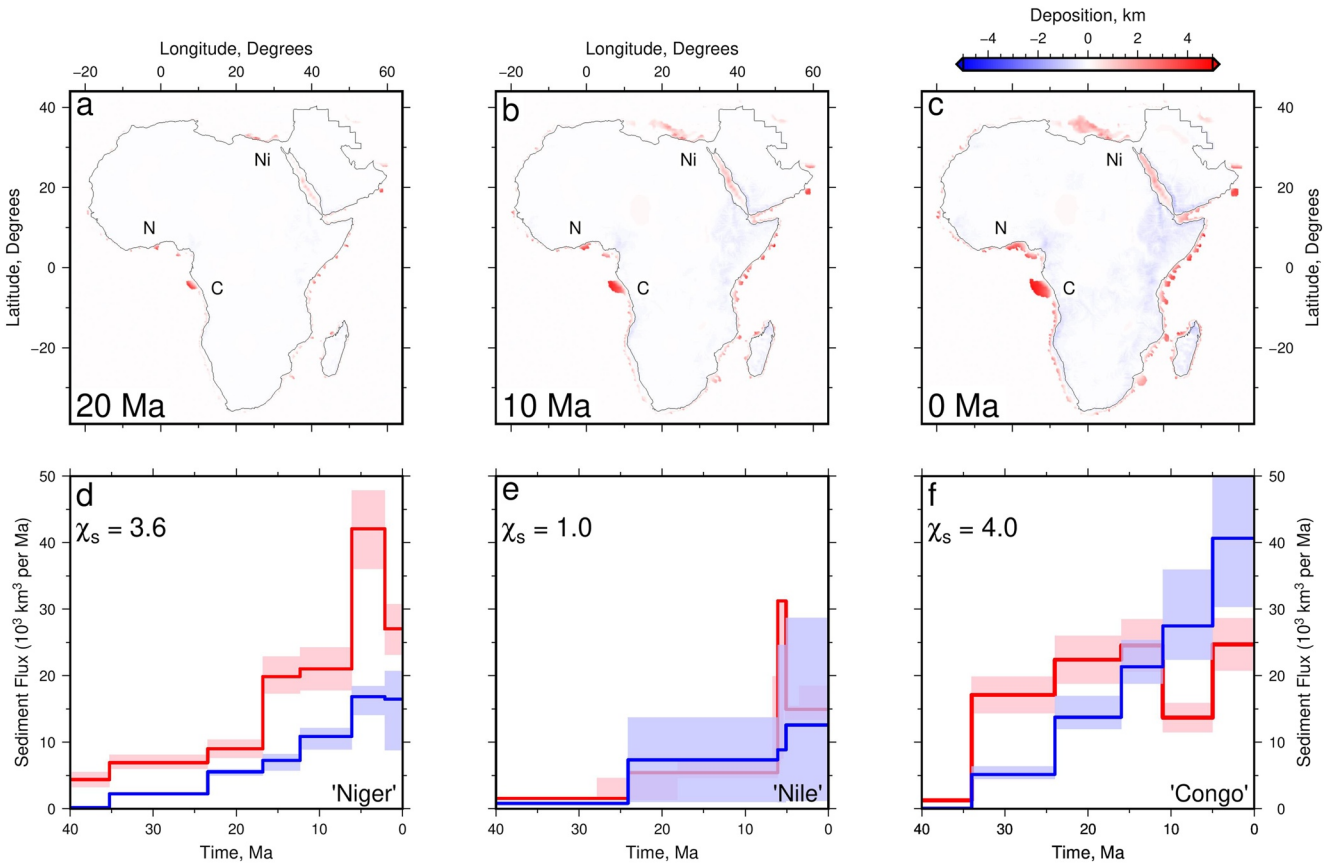

Figure 12. (a) Cumulative offshore deposition calculated at 20 Ma using Badlands algorithm where precipitation rate varies as function of latitude. (b) Same at 10 Ma. (c) Same at present day. (d) Red line with pink band = observed sedimentary flux for Niger delta (Grimaud et al., 2017; Haack et al., 2000; Rouby et al., 2011); blue line with turquoise band = predicted sedimentary flux for 'Niger' delta; χ_s = RMS misfit between observed and calculated flux. (e) Red line with pink band = observed flux for Nile delta (Abdel Aal et al., 2001; Walford, 2003); blue line with turquoise band = predicted flux for 'Nile' delta. (f) Red line with pink band = observed flux for Congo delta (Lucazeau et al., 2003); blue line with turquoise band = predicted flux $\pm 1\sigma$ for 'Congo' delta.

Thus our tests have periodicities that are much longer than those for which damping of the erosional response to climatic variations has been proposed (Godard et al., 2013).

The results of four spatio-temporal precipitation tests are presented in Figure 13. If precipitation varies with a periodicity of 1 Ma or less, the simulated landscape closely resembles the observed landscape at the present day. As expected, differences between one of these two models and a model for which precipitation only varies as a function of latitude are significant (compare Figures 11 and 13b,e). This difference is a consequence of spatio-temporally varying precipitation which causes the previously arid extremities of Africa to be slightly wetter on average and therefore to erode at a faster rate. Thus, the assumed form of spatio-temporal precipitation variation brings simulated landscapes closer to the constant precipitation scheme so that the differences between observed and simulated landscapes are reduced to $O(100)$ m.

Two more severe tests were carried out in which the periodicity was increased to 28 Ma, which permits 1.5 sinusoidal cycles of $P(x, y, t)$ over a 42 Ma duration (Figures 13i and 13l). The first test has a wet-dry-wet cycle which yields a simulated landscape that closely matches the observed landscape. There are minor differences at the northern and southern margins of Africa but the biggest differences occur close to the equator where there is a greater degree of fluvial erosion, as a consequence of an overall higher precipitation rate (Figure 13h). The second test has a dry-wet-dry cycle which has the effect of reducing the overall amount of fluvial erosion. This reduction reduces the misfit close to the equator but increases it at the northern and southern extremities. We conclude that only unrealistically lengthy excursions in precipitation are likely to have any significant effect on the overall shape of the fluvial landscape during the Neogene period when the bulk of African and Arabian topography is assumed to have been generated.

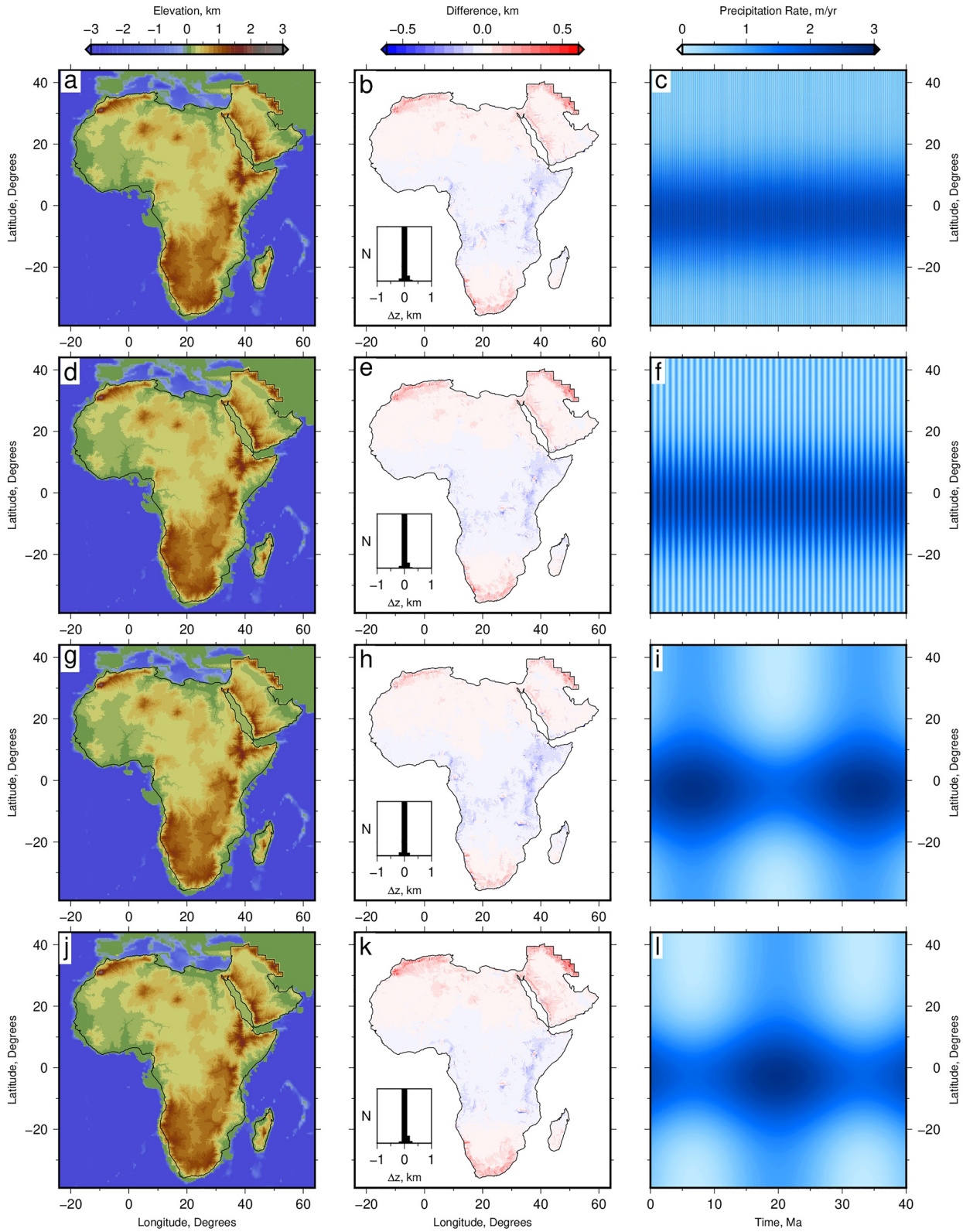
Elevation, km
−3 −2 −1 0 1 2 3
Difference, km
−0.5 0.0 0.5
Precipitation Rate, m/yr
0 1 2 3
a
b
c
d
e
f
g
h
i
j
k
l
N
−1 0 1
Δz, km
Latitude, Degrees
Longitude, Degrees
Time, Ma
−20 0 20 40 60
0 10 20 30 40

Figure 13.

Drainage planforms and longitudinal river profiles for these four tests are presented in Figure 14. In all four cases, the predicted drainage planform remains relatively unchanged and reproduces the "Nile", "Niger", and "Congo" catchments that were previously obtained. We infer that the precipitation pattern has little influence upon drainage divide migration and changes in the catchment area at the largest length scales and at the longest time scales. As before, there are systematic horizontal offsets of river profiles from each of the three catchments which reflect spatio-temporal precipitation variations. In the case of the "Nile" and "Niger" catchments, these offsets are much smaller than for spatially varying precipitation. In contrast, the "Congo" catchment has horizontal offsets of up to 1,000 km for all four precipitation tests. These offsets are slightly smaller than for constant precipitation and reflect greater values of channel erosion within the equatorial belt.

Figure 15 presents calculated sedimentary fluxes for the "Nile", "Niger", and "Congo" catchments, which are determined using four different spatio-temporal precipitation models. Overall, we find that the match between observed and calculated fluxes is better for short period variations of precipitation (i.e., 100 ka and 1 Ma). For all three catchments, this match is poorer for the longer period cycles (i.e., wet-dry-wet and dry-wet-dry). We obtain optimal results for the "Niger" catchment where the residual RMS misfit values between observed and predicted fluxes are less than 3 for periodicities of 100 ka–1 Ma and 28 Ma. As before, there are significant discrepancies between observed and predicted fluxes for the "Nile" and "Congo" catchments. We conclude that spatio-temporal variations of precipitation where the periodicity is less than 1 Ma yield the best match between observed and predicted fluvial landscapes and, to some extent, fluxes. This inference is unsurprising, given observational records that support periodic wet periods throughout Africa at latitudes where hyperaridity prevails at the present day. Marine sedimentary records show that this periodicity is orbitally forced and generally shorter than 100 ka (DeMenocal, 1995,2004; Holz et al., 2007; Stuut et al., 2002). Although the shortest periods used here are 100 ka and 1 Ma, our conclusions obviously hold for even shorter periods. The match between observed and predicted landscapes and fluxes deteriorates when we use very long period variations.

4. Closed-Loop Modeling

We return to the inverse problem by carrying out closed-loop modeling which is a well-known method for analyzing the significance of different degrees of complexity (Lorenz, 1963). Our aim is to test the efficacy of a simplified inverse modeling approach by inverting suites of river profiles generated by dynamic landscape simulations under different precipitation conditions. We carry out these tests for two reasons. First, we wish to determine whether or not a central assumption of river profile inverse modeling is reasonable, namely, invariance of upstream drainage area, A, as a function of time. In other words, is inverse modeling of fixed channels robust to fluvial dynamicism that takes the form of drainage divide migration and changes in catchment size? One way of tackling this problem is to exploit the inherent dynamicism that underpins landscape simulations (i.e., the fact that these simulations repeatedly route flow across the landscape after it has been altered by external forcing and by fluvial erosion, which produces variable drainage planforms). Second, we wish to test whether or not an inverse model that assumes constant precipitation can recover valid regional uplift histories from landscape simulations that assume different spatial and temporal patterns of precipitation. This goal is achieved by inverting drainage networks extracted from synthetic landscapes—an essential component of the closed-loop modeling strategy.

4.1. Constant Precipitation

We invert suites of synthetic river profiles that have been generated by six different landscape simulations, starting with a constant precipitation model and culminating with more complex spatio-temporal precipitation models. Figure 16 shows the results of inverting ~3600 synthetic river profiles extracted from a constant precipitation landscape simulation where $P = 1$ m yr^{-1}. Values of v and m are identical to those used to calculate the original

Figure 13. (a) Synthetic African landscape calculated for present day using Badlands algorithm subject to cumulative uplift history shown in Figure 2, where precipitation rate varies as a function of latitude and as function of time with a period of 100 ka (Figure 10). (b) Difference between synthetic landscapes calculated using spatio-temporally variable and constant precipitation rate. Inset panel shows a histogram of differences between simulated and observed landscapes. RMS value = 1.45, average misfit = 29 m, and volumetric misfit = 1.0×10^6 km^3. (c) Precipitation rate as function of latitude and time with period of 100 ka. (d–f) Same for period of 1 Ma. RMS value = 1.45, average misfit = 29 m, and volumetric misfit = 1.0×10^6 km^3. (g–i) Same for period of 28 Ma (wet-dry-wet cycle). RMS value = 1.55, average misfit = 31 m, and volumetric misfit = 1.1×10^6 km^3. (j–l) Same for period of 28 Ma (dry-wet-dry cycle). RMS value = 1.65, average misfit = 33 m, and volumetric misfit = 1.1×10^6 km^3.

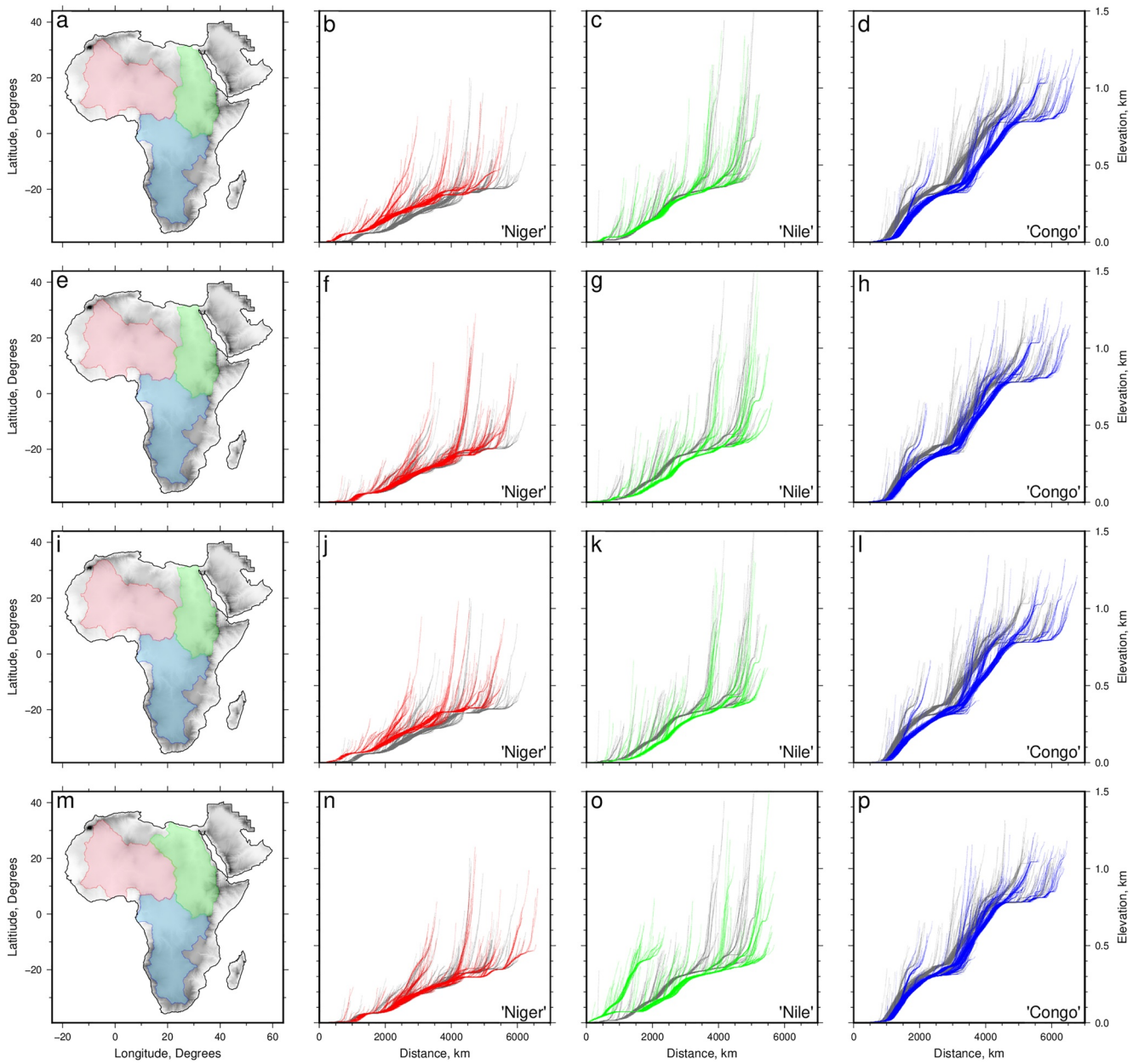

Figure 14. (a) Synthetic catchment pattern for spatio-temporally varying precipitation with period of 100 ka. Red/green/blue polygons = 'Niger'/'Nile'/'Congo' catchments, respectively. (b) Synthetic river profiles for 'Niger' catchment where black lines in background are synthetic profiles calculated assuming constant precipitation (Figure 7). (c) Same for 'Nile' catchment. (d) Same for 'Congo' catchment. (e)–(h) Synthetic example where period is 1 Ma. (i)–(l) Synthetic example where period is 28 Ma (wet-dry-wet cycle). (m)–(p) Synthetic example where period is 28 Ma (dry-wet-dry cycle).

tectonic forcing. As before, the model start time is given by the maximum value of τ_G for the drainage network, which in turn depends upon v and m (Equation 6). Calculated model start times are older than 42 Ma by which time inverse models are well resolved. Suites of river profiles from the three principal catchments can be adequately fitted with negligible residual misfit values. These residual misfits are smaller than those obtained by inverting observed river profiles because fluvial landscapes are affected by a range of processes that are not included in landscape simulations (e.g., variable erosion rates, sediment transport, vegetative binding, non-linear fluid flow). These processes probably contribute to the whitening of power spectra of river profiles at length scales that are shorter than ~100 km (G. G. Roberts, 2019; G. G. Roberts, White, et al., 2019). Damped, non-negative inverse models are specifically designed to fit large-scale knickzones that are more likely to have been generated

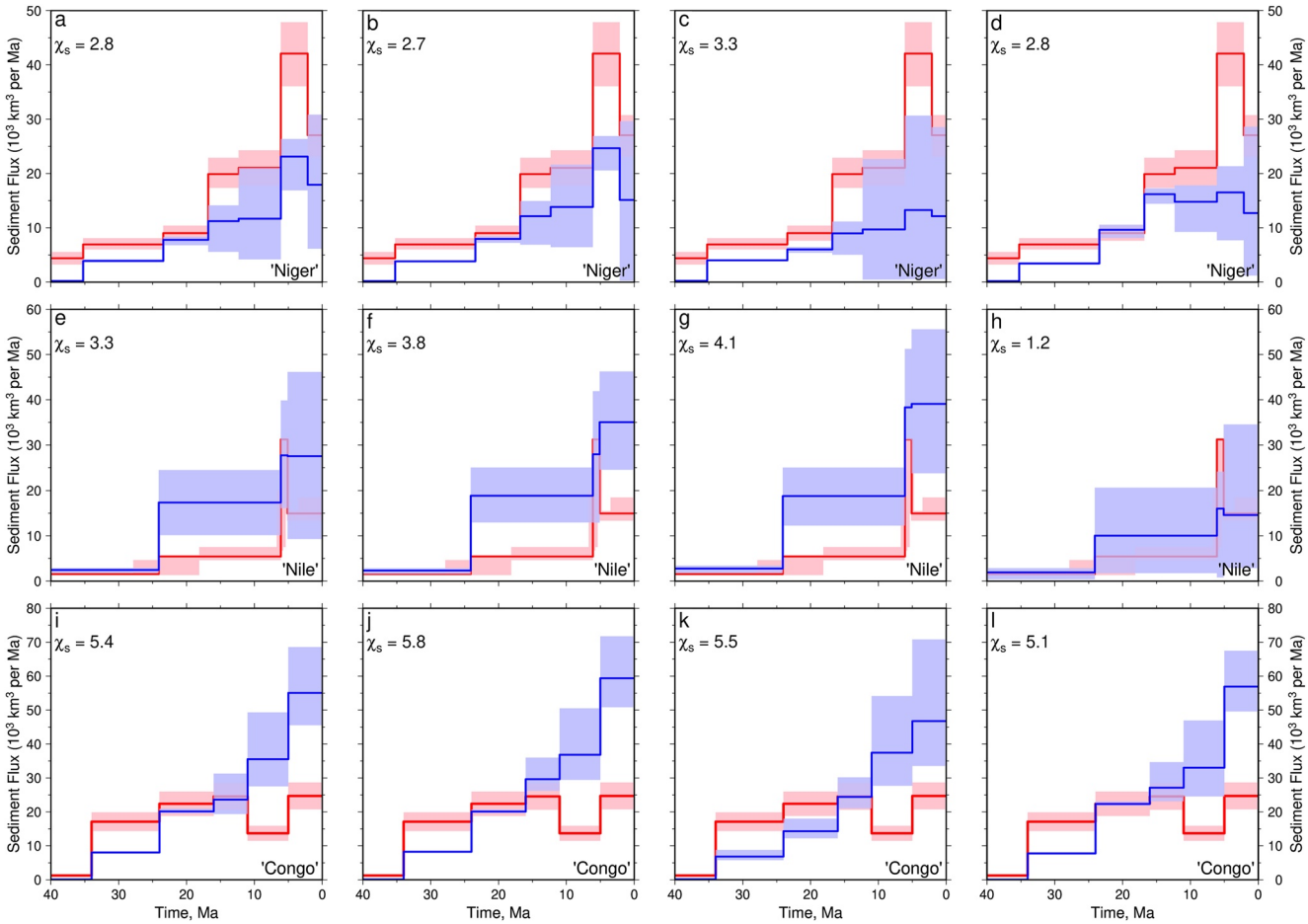

Figure 15. (a) Red line with pink band = observed sedimentary flux for Niger delta; blue line with turquoise band = predicted sedimentary flux for 'Niger' delta assuming spatio-temporally varying precipitation with period of 100 ka; χ_s = RMS misfit between observed and calculated flux. (b) Same for period of 1 Ma. (c) Same for period of 28 Ma (wet-dry-wet cycle). (d) Same for period of 28 Ma (dry-wet-dry cycle). (e–h) Same for Nile and 'Nile' deltas. (i–l) Same for Congo and 'Congo' deltas.

by tectonic forcing. Figures 16a–16c show the cumulative regional uplift history since 42 Ma that is recovered by inverse modeling. This uplift history closely resembles the original tectonic forcing obtained by inverting the observed drainage inventory of Africa. Assuming a standard uncertainty of 20 m, the average RMS misfit between input and recovered cumulative uplift, calculated for all time steps between 42 and 0 Ma, is $\bar{\chi}_l = 6.6$. This value reflects the fact that the inverse algorithm includes significant damping and smoothing.

Regional uplift starts in eastern and southern Africa, spreading northwestward as a function of time. Note that the resultant uplift history tends to underestimate the observed topography as well as that determined by inverse modeling of observed river profiles shown in Figure 2. This underestimate reflects the fact that fluvial channels are to some extent low-lying transects that cut through landscapes, that automatically extracted drainage networks generally do not extend as far back as drainage divides, and that the inverse model is significantly damped and smoothed. Figure 16 demonstrates that, despite being allowed to dynamically emerge and evolve as a function of time in response to regional uplift and erosion, simulated river profiles record the original tectonic forcing (Figures S14–S16 of Supporting Information S1). Uplift rate events at different times since 40 Ma can also be recovered, which indicates that the inverse algorithm is not biased toward monotonically increasing uplift rate. Recent uplift rate events are better fitted by closed-loop modeling, which is a consequence of decreasing temporal resolution with increasing age. Maps of original and recovered uplift rate histories are presented in Figure S26 of Supporting Information S1. The mean difference between original and recovered uplift rate through space and time is 0.006 mm yr^{-1}. This difference is greatest wherever synthetic drainage planforms least resemble observed planforms or where the spatial gradient of uplift rate is highest (e.g., Angola, Madagascar).

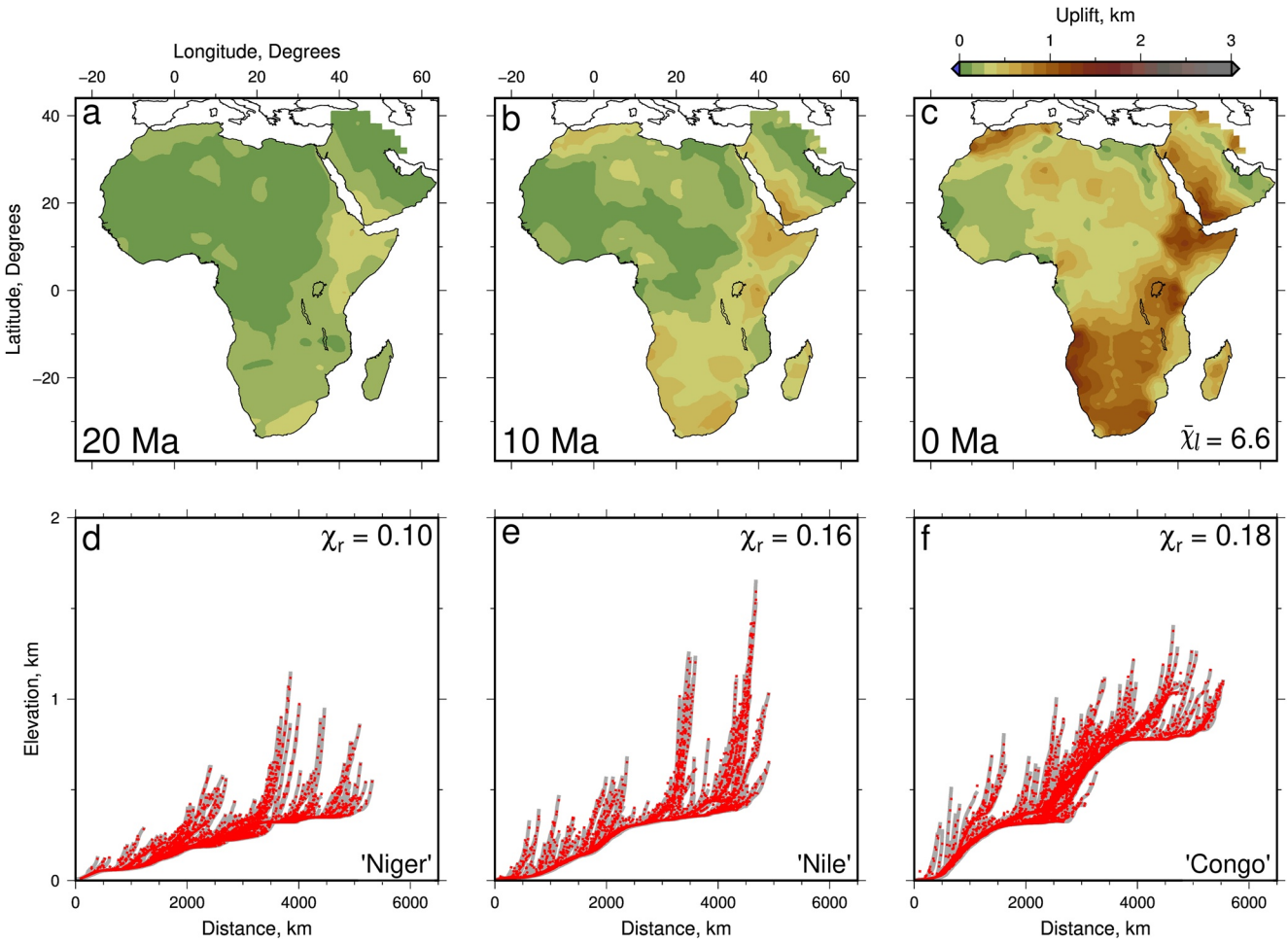

Figure 16. (a) Cumulative uplift of Africa and Arabia at 20 Ma calculated by inverse modeling of ~3600 river profiles extracted from synthetic landscape generated using Badlands algorithm with constant precipitation. (b) Same at 10 Ma. (c) Same at present day. $\bar{\chi}_l$ = RMS misfit between 'observed' and calculated cumulative uplift histories. (d) Gray lines = 'observed' river profiles from 'Niger' catchment; red dotted lines = calculated river profiles determined by inverse modeling; χ_r is RMS misfit between 'observed' and calculated profiles. (e) Same for 'Nile' catchment. (f) Same for 'Congo' catchment.

4.2. Variable Precipitation

Inverse modeling of river profiles assumes that precipitation is constant as a function of space and time. This assumption can be tested by inverting synthetic river profiles calculated by landscape simulations which are run for a variety of precipitation models. Once again, this approach is based upon closed-loop modeling. In each case, inversion is carried out by assuming that upstream drainage area alone is a proxy for discharge, the precipitation term is ignored, and values of v and m are identical to those used to calculate the original tectonic forcing.

Figure 17 displays a suite of cumulative uplift histories which were calculated by separately inverting river profiles which were generated using five different precipitation models. The first model assumes that precipitation varies as a function of latitude (Figures 17a–17c). In this case, the average RMS misfit between the original and the recovered cumulative uplift histories is $\bar{\chi}_l = 7.1$. Note that regional uplift along the northern and southern edges of Africa occurs later than that in the original landscape simulation. This discrepancy is caused by the low values of precipitation rate at latitudes higher than ±30° since it means that simulated knickzones do not retreat at a sufficiently fast rate along fluvial channels within the upper reaches of the "Niger" catchment and the western and southern reaches of the "Nile" catchment. These smaller values cause uplift events to be translated forward in time to compensate for knickzones having traveled shorter distances. Nonetheless, the original and recovered landscapes agree at the present day and the relative timing of major uplift episodes is approximately correct. The mean misfit between the original and recovered cumulative uplift is 136 m per node.

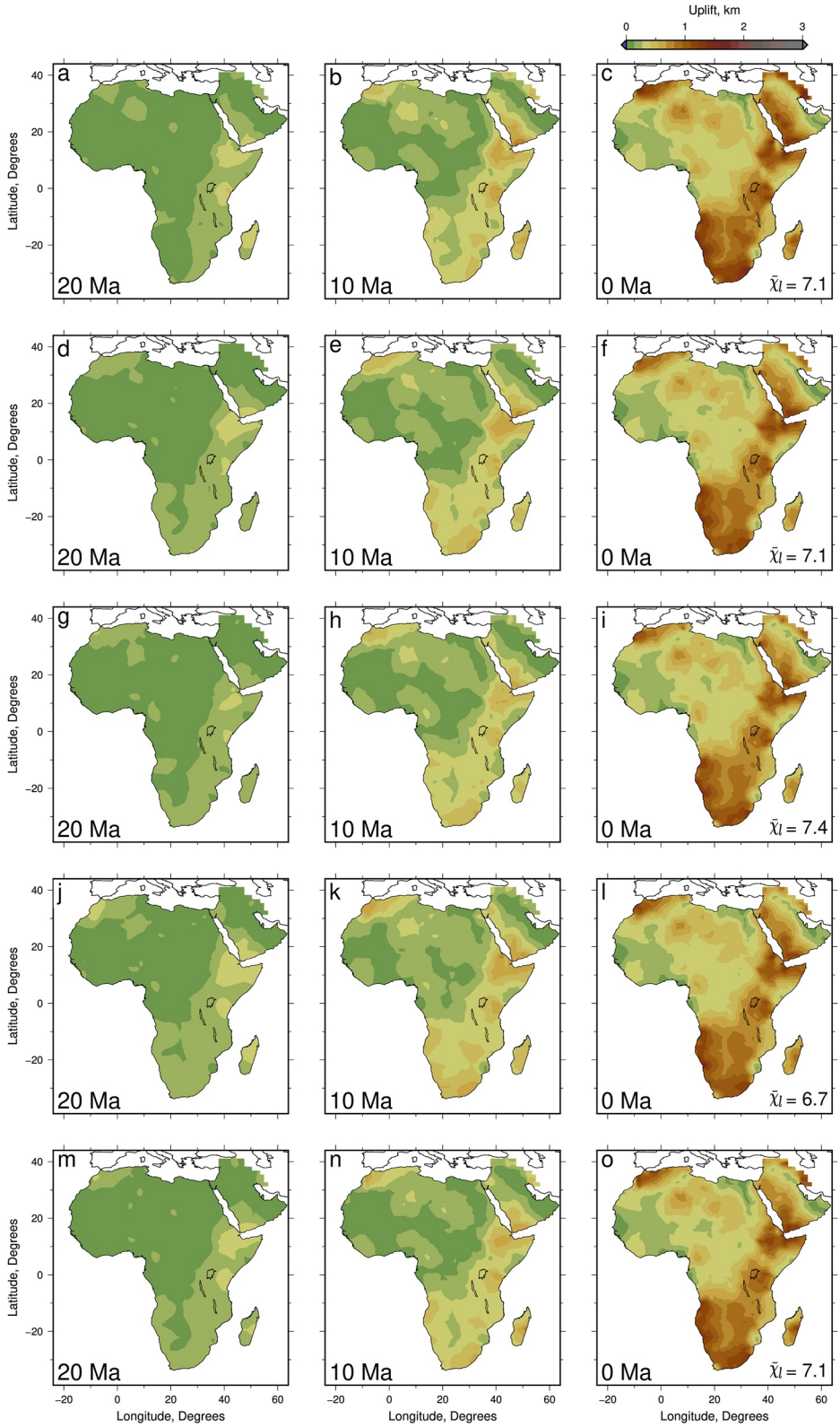

Figure 17. (a–c) Cumulative uplift history of Africa and Arabia calculated by inverse modeling of ~3,600 river profiles extracted from synthetic landscape generated using Badlands algorithm with spatially varying precipitation (Figure 13). $\bar{\chi}_l$ = RMS misfit between 'observed' and calculated cumulative uplift histories. (d–f) Same for spatio-temporally varying precipitation with period of 100 ka (Figure 13c). (g–i) Same for period of 1 Ma (Figure 13f). (j–l) Same for period of 28 Ma (wet-dry-wet cycle; Figure 13i). (m–o) Same for period of 28 Ma (dry-wet-dry cycle; Figure 13l).

Figures 17d–17o and 18d–18o show the results of inverse modeling of different river profile inventories that were simulated by spatio-temporal variations of P. Periodicities of 100 ka, 1 Ma, 28 Ma (wet-dry-wet), and 28 Ma (dry-wet-dry) are employed. In general, the inclusion of variable precipitation across Africa and Arabia in landscape simulations helps to improve the timing of uplift events within northern and southern Africa. The two short period precipitation models yield the most reasonable uplift histories. Note that river profiles generated by long period variations of P can still be inverted to produce faithful cumulative uplift histories (Figures 19b–19g). The principal difference arises for the (dry-wet-dry) cyclicity which causes uplift events along the northern and southern edges to be recovered at later times due to the average precipitation rates at higher latitudes in the forward-modeled landscape simulation being less than 1 m yr^{-1}. Since the simulated landscape is subject to an average precipitation rate over time that is similar to the modern spatial distribution for Africa, this recovered result closely matches that obtained for the spatially varying precipitation model. These inferences are borne out by comparing original and recovered cumulative uplift histories for individual nodes (Figure 19). For example, at the 'Hoggar' location, the recovered uplift rate history is translated forward in time by ~5 Ma with respect to the original uplift rate history (Figure 19f). Even though "Hoggar" is located in the driest part of the landscape simulation, it is encouraging that this difference is modest. Even smaller differences are found in the (wet-dry-wet) cyclicity is employed.

These results suggest that differences between original and recovered cumulative uplift histories are not significant if precipitation rate, P, is permitted to vary as a function of time and space (Figures 17–19). For periodicities of 100 ka, 1 Ma, 28 Ma (wet-dry-wet), and 28 Ma (dry-wet-dry), we obtain average RMS misfit values between the original and recovered landscapes of $\bar{\chi}_l$ =7.1, 7.4, 6.7, and 7.1. The size of these values reflects the fact the inverse algorithm is significantly damped and smoothed. Differences between uplift rate histories recovered from drainage generated by landscape simulations with constant and variable precipitation rates are presented in Figures S27–S31 of Supporting Information S1. Mean differences between the recovered forcing, given variable precipitation rates, are $\leq$0.003 mm yr^{-1}.

We propose that spatio-temporal changes in precipitation do not have an especially negative influence on our ability either to match inventories of river profiles or to calculate regional uplift histories that are consistent with independent geologic observations. This result is probably neither unexpected nor surprising given that the solution to the stream-power equation is integrative. In other words, average discharge along a fluvial channel is more significant than instantaneous discharge in controlling the geometries of longitudinal river profiles. We conclude that regional tectonic uplift plays the predominant role in generating and sculpting landscapes. This external forcing can be regarded as the primary factor in determining fluvial channel evolution and knickzone retreat.

5. Discussion and Conclusions

We have revised, streamlined, and augmented an inventory of longitudinal river profiles for Africa, Arabia, and Madagascar that was originally assembled by Paul et al. (2014), Wilson et al. (2014), and G. G. Roberts et al. (2012). Now, a total of 4,018 river profiles are extracted from a digital elevation model. This considerably expanded database was inverted using the damped non-negative least squares scheme described by Rudge et al. (2015). We find that suites of river profiles appear to contain coherent records of uplift events that influenced landscape development during Neogene times. This cumulative uplift history is in agreement with independent geologic constraints (Figure 3). Much of this region appears to have been at, or below, sea level by the end of the Cretaceous period and during Paleogene times. This observation justifies an initial condition of negligible or modest topography, although we freely acknowledge that there is limited direct evidence for this assumption across southern Africa. Here, it is necessary to appeal to isostatic arguments and to the similarity with the Namibian and Angolan domes, for which there is a more robust case in favor of Neogene uplift.

Isostatic arguments for youthful elevation of southern Africa are summarized in Figure 20. An initial lithospheric template is calculated by balancing continental lithosphere at sea level against the structure of a mid-ocean ridge. Depletion of the reference mantle density was scaled between 0–20 kg m^{-3} based upon present-day lithospheric thicknesses that vary between 116 and 220 km, respectively (Priestley et al., 2019). If the present-day lithospheric thickness is a_1, then the reference mantle density, ρ_m^* is given by

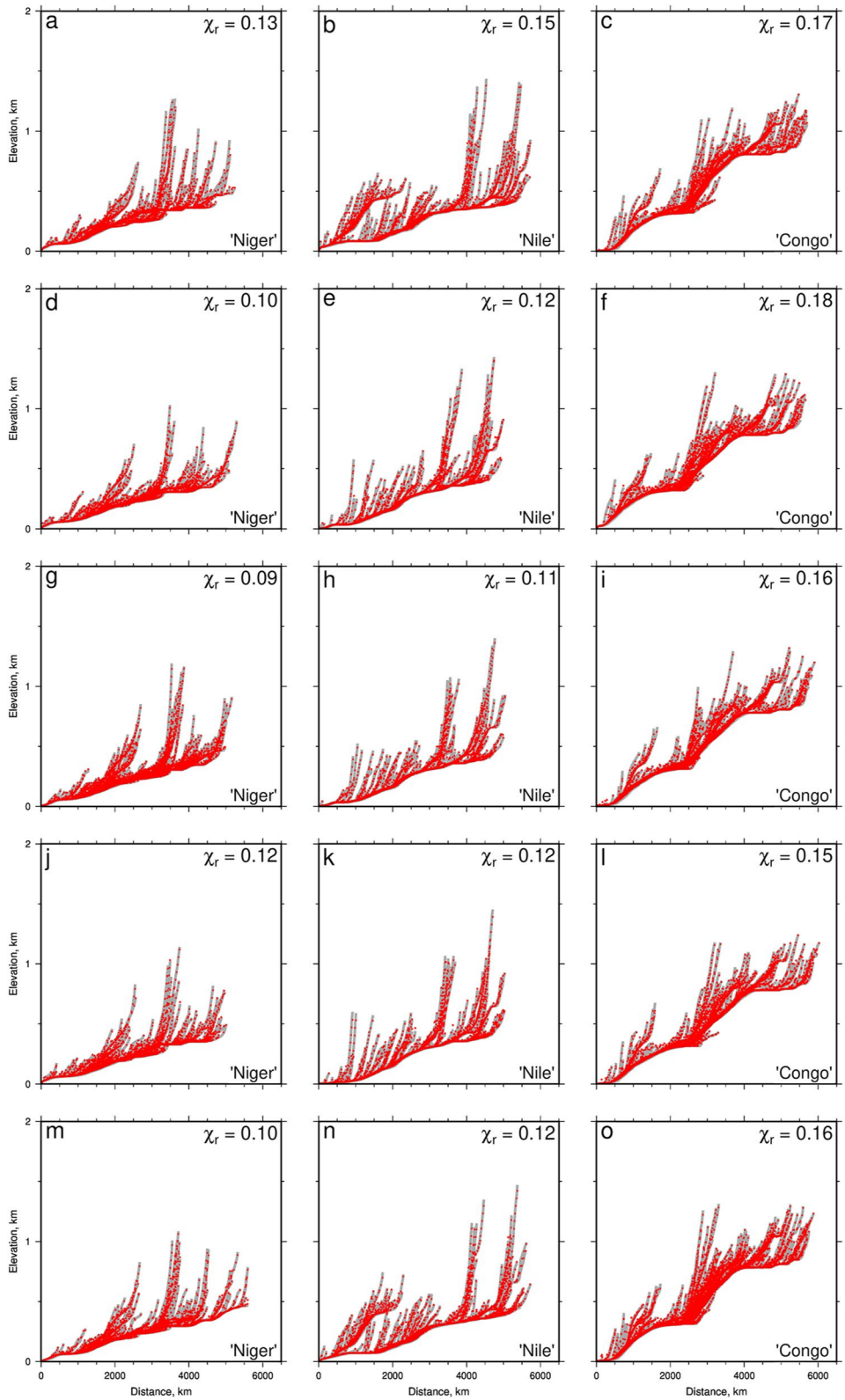

Figure 18. (a) Gray lines = 'observed' river profiles from 'Niger' catchment extracted from synthetic landscape generated using Badlands algorithm with spatially varying precipitation (Figure 13); red dotted lines = calculated river profiles determined by inverse modeling that assumes constant precipitation; χ_r = RMS misfit. (b) Same for 'Nile' catchment. (c) Same for 'Congo' catchment. (d–f) Same for spatio-temporally varying precipitation with period of 100 ka (Figure 13c). (g–i) Same for period of 1 Ma (Figure 13f). (j–l) Same for period of 28 Ma (wet-dry-wet cycle; Figure 13i). (m–o) Same for period of 28 Ma (dry-wet-dry cycle; Figure 131).

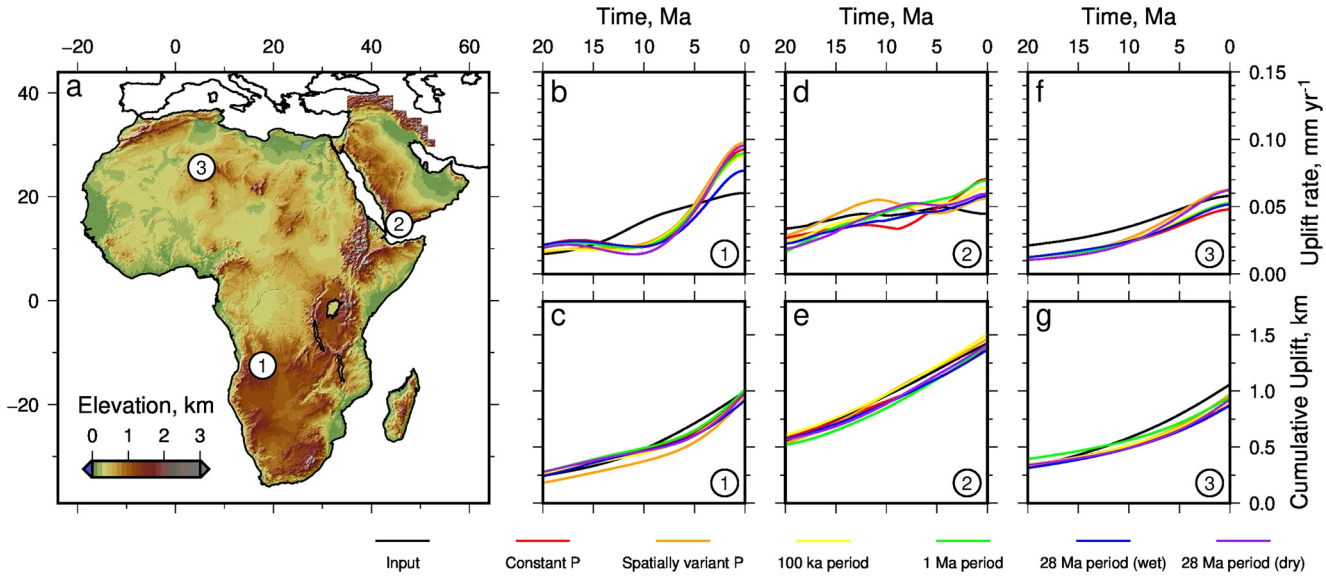

Figure 19. (a) Observed African topography. ①,②,③ = locations of nodes from the inverse model at which uplift histories are plotted. (b) Uplift rate as a function of time averaged over nine nodes at location ① from Angolan dome. Black line = uplift rate history recovered by inverse modeling of observed drainage network; colored lines = uplift rate histories recovered by inverse modeling of synthetic drainage networks generated by landscape simulations forced by original uplift rate history but subject to different precipitation histories (see legend for color scheme and Figure 17). (c) Equivalent cumulative uplift histories. (d and e) Same for location ③ from Yemeni Highlands. (f) and (g) Same for location ② from Hoggar massif.

$$\rho_m^* = \begin{cases} 3.33 \ (= \rho_m) & \text{if } a_1 < 170 \text{ km} \\ (-3.33 \times 10^{-4}) a_1 + 3.39 & \text{if } 170 \le a_1 \le 230 \text{ km} \\ 3.31 & \text{if } a_1 > 230 \text{ km.} \end{cases} \quad (14)$$

The average crustal thickness is assumed to be 40 km. Elevation generated by thinning the lithosphere is shown in Figure 20b. A hypothetical 100-km thick layer of hot asthenospheric material at the base of the present-day lithosphere, for which there is increasing global tomographic evidence generates additional elevation (Rudge et al., 2008, Figure 20c). In agreement with A. G. Jones et al. (2017), these calculations suggest that the elevation of the South African plateau is underpredicted, implying that there is an additional contribution from the deeper mantle.

In this African study, we assess the significance of key limitations inherent to an inverse algorithm that is based upon the stream power law. First, continental variability of geomorphic parameters v and m can give rise to significant uncertainties since the inverse modeling approach is usually predicated upon constant values. To address this limitation, we exploit a database of emergent marine deposits with a range of ages. Our novel strategy of calibration and validation suggests that observed and calculated regional uplift rates agree within the limits of uncertainty. This agreement suggests that the values of v and m do not significantly vary on the spatial and temporal scales of interest, at least for the African continent. Second, it is often argued that $n > 1$, which would mean that under certain specific conditions 'signal shredding' is anticipated (i.e., loss of signal when steeper knickzones overtake and therefore "consume" shallower knickzones). Rudge et al. (2015) amongst others have demonstrated that $n = 1$ yields the smallest misfit between observed and calculated river profiles. Although their analysis does not necessarily prove that $n = 1$, the implication is that this version of the empirical stream power law is appropriately parsimonious. To bolster this argument, we carried out a series of forwarding and inverse modeling tests where $n \neq 1$, which demonstrate that assuming $n = 1$ yields the smallest misfit between observed and simulated landscapes and optimal recovery of uplift rate (Figures S1–S5 of Supporting Information S1). Third, we acknowledge that there could be many other complicating factors such as erosional thresholds, transport-limited effects, and erosionally coupled precipitation. Our contention is that the importance of these factors can only be objectively assessed by closed-loop modeling. In this way, we have carefully and objectively investigated the effect that erosionally coupled precipitation can have (Figures S20–S25 of Supporting Information S1). We discover that

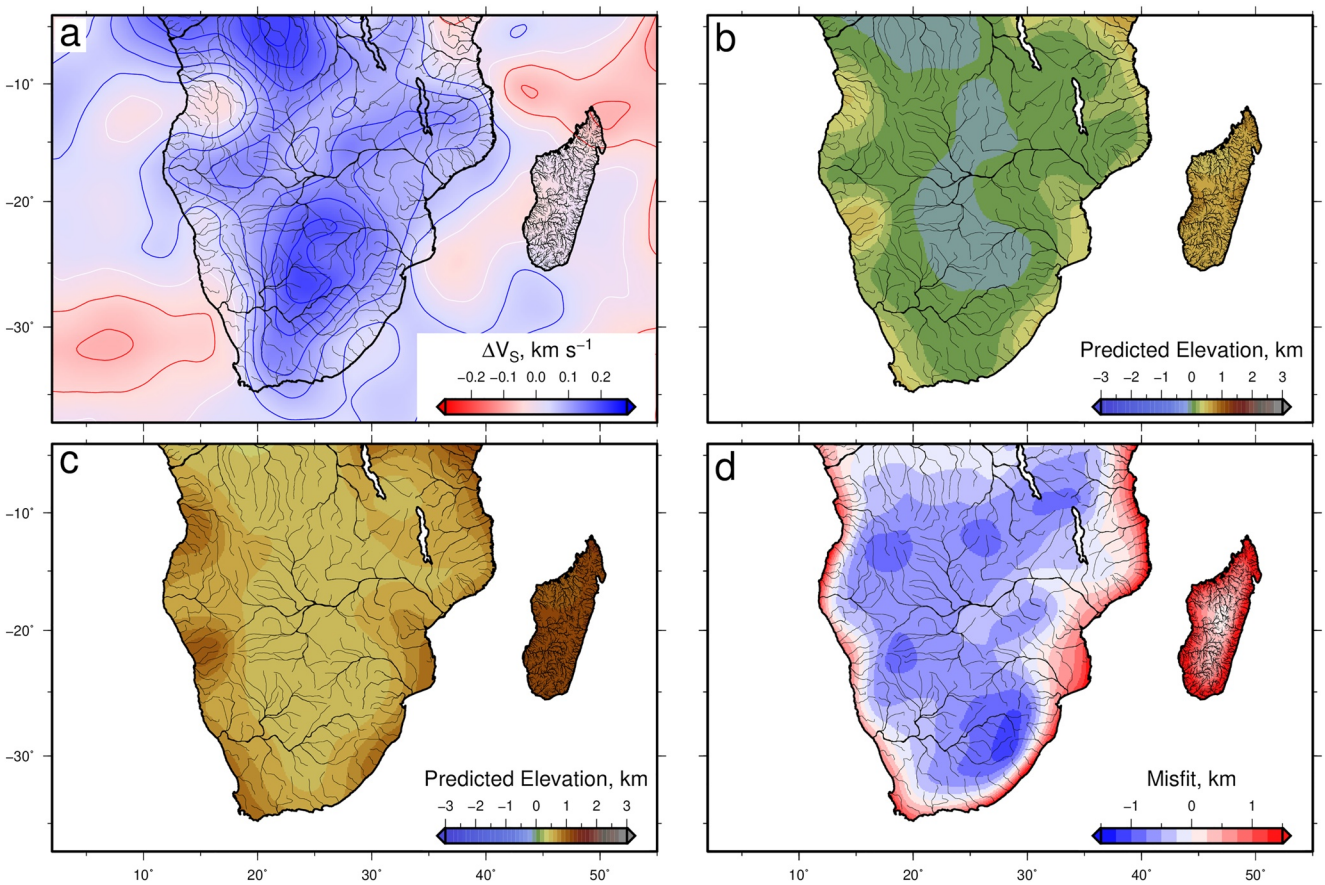

Figure 20. (a) Map of shear wave velocity anomalies beneath sub-equatorial Africa averaged between 100 and 200 km taken from surface wave tomographic model of Schaeffer and Lebedev (2013). Black network = observed river profiles. (b) Regional topography calculated by thinning initial lithospheric template that sits at sea level so that it matches present-day lithospheric thickness (initial template constructed from two end members: 116 km thick lithosphere beneath the Phanerozoic crust and 220 thick lithosphere beneath the cratonic crust. (c) Calculated present-day topography as in panel b with additional ∼500 m of regional elevation generated by temperature anomaly of 150°C in 100–200 thick channel beneath African plate. (d) Residual misfit between calculated topography from panel c and observed topography, where the latter has been low-pass filtered so that wavelengths < 500 km are excluded.

coupling between P and v has only a modest influence on the recoverability of tectonic forcing. Other proposed forms of complexity should be investigated in the same objective manner with a view to identifying the simplest models that best fit the observations.

Our principal conclusion is that the drainage patterns of Africa, Arabia, and Madagascar appear to be moderated by regional uplift with wavelengths of $\sim 10^3$ km and amplitudes of ∼1 km. Substantial inventories of river profiles demonstrate that systematic and mappable patterns of knickzones exist. Joint inverse modeling of river profiles yields a cumulative uplift history that is consistent with independent geologic observations. Landscape simulations that are forced by this uplift history yield drainage networks that bear similarities with the observed planform, although there are significant differences with respect to the sizes of the biggest catchments. Similar networks are recovered when precipitation rates are varied as a function of space and time. Inverse modeling of synthetic river profiles extracted from these forward-modeled landscape simulations for varying precipitation rate conditions yields uplift histories that broadly match the original forcing subject to damping and smoothing constraints. Minor discrepancies between original and recovered tectonic forcing can arise where simulated and observed drainage planforms differ. This application of closed-loop modeling provides support for the use of simplified inverse algorithms.

Finally, we agree with Salles et al. (2017) that tectonic uplift appears to be the dominant forcing mechanism of fluvial landscapes. Ultimately, sculpting of the African, Arabian, and Malagasy landscapes appear to be moderated by the development of sub-plate temperature anomalies that are well resolved by many, but not all, tomographic models (Al-Hajri et al., 2009; Hoggard et al., 2016; Schaeffer & Lebedev, 2013). Application of the empirical

stream power incision equation to the evolution of surface drainage in response to mantle convective processes suggests that coherent signals of regional uplift carved into landscapes are, in principle, recoverable. The integrative nature of this formulation implies that river profiles generated by landscape simulation in response to a known regional uplift history can be inverted to recover the original uplift history, notwithstanding periodic precipitation forcing as a function of space and time.

Data Availability Statement

Digital elevation measurements and inverse modeling algorithms can be downloaded from srtm.csi.cgair.org and https://doi.org/10.5281/zenodo.5536459, respectively. Python version of Badlands landscape simulation code (v1.1.0) is available from https://doi.org/10.5281/zenodo.268053.

Acknowledgments
This work forms part of a collaboration between the University of Cambridge and BP Exploration. CO is supported by Leverhulme Trust grant RPG-2019-073. Paleontologic databases were extracted from paleobiodb.org. Figures were prepared using Generic Mapping Tools v6 (Wessel et al., 2019). The authors thank J. Armitage, P. Ball, P. van der Beek, J. Braun, A. Dickinson, C. Faccenna, V. Fernandes, I. Frame, A. Jackson, A. Lipp, D. Lyness, F. McNab, F. Richards, C. Richardson, J. Rudge, and A. Woods for their help. S. Willett and S. Gallen provided excellent, thorough, thought-provoking, and lengthy reviews. Department of Earth Sciences contribution number esc. 6036.

References

Abdel Aal, A., El Barkooky, A., Gerrits, M., Meyer, H., Schwander, M., & Zaki, H. (2001). Tectonic evolution of the Eastern Mediterranean Basin and its significance for the hydrocarbon prospectivity of the Nile Delta deepwater area. *GeoArabia*, *6*(3), 363–384.

Abdelkareem, M., Ghoneim, E., El-Baz, F., & Askalany, M. (2012). New insight on paleoriver development in the Nile basin of the eastern Sahara. *Journal of African Earth Sciences*, *62*(1), 35–40. https://doi.org/10.1016/j.jafrearsci.2011.09.001

Abouessa, A., Pelletier, J., Duringer, P., Schuster, M., Schaeffer, P., Métais, E., et al. (2012). New insight into the sedimentology and stratigraphy of the Dur At Talah tidal-fluvial transition sequence (Eocene-Oligocene, Sirt Basin, Libya). *Journal of African Earth Sciences*, *65*, 72–90. https://doi.org/10.1016/j.jafrearsci.2012.02.004

Abu El-Ella, R. (1990). The Neogene-quaternary section in the Nile Delta, Egypt: Geology and hydrocarbon potential. *Journal of Petroleum Geology*, *13*(3), 329–340. https://doi.org/10.1111/j.1747-5457.1990.tb00850.x

Adnet, S., Hosseinzadeh, R., Antunes, M. T., Balbino, A. C., Kozlov, V. A., & Cappetta, H. (2009). Review of the enigmatic Eocene shark genus Xiphodolamia (Chondrichthyes, Lamniformes) and description of a new species recovered from Angola, Iran and Jordan. *Journal of African Earth Sciences*, *55*(3–4), 197–204. https://doi.org/10.1016/j.jafrearsci.2009.04.005

Aït-Hamou, F., Dautria, J.-M., Cantagrel, J.-M., Dostal, J., & Briqueu, L. (2000). New geochronological and isotopic data on the Cenozoic volcanism of Ahaggar (southern Algeria): Evidence for a mantle plume. *Geochemistry*, *330*, 829–836.

Al-Hajri, Y., White, N., & Fishwick, S. (2009). Scales of transient convective support beneath Africa. *Geology*, *37*(10), 883–886. https://doi.org/10.1130/G25703A.1

Allegre, R. (1939). Quelques Membraniporides du Cretace de l'Aures (Algerie) Cretaceous Membraniporidae from Aures (Algeria). *Bulletin du Museum National d'Histoire Naturelle*, *11*, 163–166.

Al-Qayim, B., Al-Sanabani, J., & Al-Subbary, A. K. (2005). Paleoenvironmental implication of marine bioturbated horizons in the Majzir Formation, Western Yemen. *Arabian Journal for Science and Engineering*, *30*(2A), 165–180.

Al-Subbary, A.-K., Nichols, G. J., Bosence, D. W. J., & Al-Kadasi, M. (1998). Pre-rift doming, peneplanation or subsidence in the southern Red Sea? Evidence from the Medj-zir Formation (Tawilah Group) of western Yemen. In B. H. Purser, & D. W. J. Bosence (Eds.), *Sedimentation and tectonics of rift basins: Red sea-Gulf of aden* (pp. 119–134): Chapman & Hall. https://doi.org/10.1007/978-94-011-4930-3_8

Anderson, R. S., & Anderson, S. P. (2010). *Geomorphology: The Mechanics and Chemistry of landscapes*. Cambridge University Press.

Anka, Z., Séranne, M., Lopez, M., Scheck-Wenderoth, M., & Savoye, B. (2009). The long-term evolution of the Congo deep-sea fan: A basin-wide view of the interaction between a giant submarine fan and a mature passive margin (ZaiAngo project). *Tectonophysics*, *470*(1–2), 42–56. https://doi.org/10.1016/j.tecto.2008.04.009

Armitage, S. J., Drake, N. A., Stokes, S., El-Hawat, A., Salem, M. J., White, K., et al. (2007). Multiple phases of North African humidity recorded in lacustrine sediments from the Fazzan Basin, Libyan Sahara. *Quaternary Geochronology*, *2*(1–4), 181–186. https://doi.org/10.1016/j.quageo.2006.05.019

Azzaroli, A. (1958). L'Oligocene e il Miocene della Somalia. Stratigrafia, Tettonica, Paleontologia (Macroforaminferi, Coralli, Molluschi). *Palaeontolographia Italica*, *52*, 1–142.

Baby, G., Guillocheau, F., Braun, J., Robin, C., & Dall'Asta, M. (2019). Solid sedimentation rates history of the Southern African continental margins: Implications for the uplift history of the South African Plateau. *Terra Nova*, *00*, 1–65. https://doi.org/10.1111/ter.12435

Ball, P. W., White, N. J., Masoud, A., Nixon, S., Hoggard, M. J., Maclennan, J., et al. (2019). Quantifying asthenospheric and lithospheric controls on Mafic magmatism across North Africa. *Geochemistry, Geophysics, Geosystems*, *20*, 1–3555. https://doi.org/10.1029/2019gc008303

Beauvais, A., & Chardon, D. (2013). Modes, tempo, and spatial variability of Cenozoic cratonic denudation: The West African example. *Geochemistry, Geophysics, Geosystems*, *14*(5), 1590–1608. https://doi.org/10.1002/ggge.20093

Beauvais, A., Ruffet, G., Hénocque, O., & Colin, F. (2008). Chemical and physical erosion rhythms of the West African Cenozoic morphogenesis: the ^{39}Ar-^{40}Ar dating of supergene K-Mn oxides. *Journal of Geophysical Research*, *113*, 1–15. https://doi.org/10.1029/2008JF000996

Becker, J. J., Sandwell, D. T., Smith, W. H. F., Braud, J., Binder, B., Depner, J., & Weatherall, P. (2009). Global bathymetry and elevation data at 30 arc seconds resolution: SRTM30 PLUS. *Marine Geodesy*, *32*(4). https://doi.org/10.1080/01490410903297766

van der Beek, P., & Braun, J. (1999). Controls on post-mid-Cretaceous landscape evolution in the southeastern highlands of Australia: Insights from numerical surface process models. *Journal of Geophysical Research*, *104*(B3), 4945. https://doi.org/10.1016/0031-0182(86)90095-7

van der Beek, P., Summerfield, M. A., Braun, J., Brown, R. W., & Fleming, A. (2002). Modeling postbreakup landscape development and denudational history across the southeast African (Drakensberg Escarpment) margin. *Journal of Geophysical Research: Solid Earth*, *107*(B12), 4966. ETG 11–1–ETG 11–18. https://doi.org/10.1029/2001JB000744

Bellion, Y., Saint-Marc, P., & Damotte, R. (1989). Contribution à la connaissance des dépôts marin au passage Crétacé-Tertiaire dans la vallée du Tilemsi (Nord-Mali). *Journal of African Earth Sciences*, *9*(1), 187–194. https://doi.org/10.1016/0899-5362(89)90020-1

Berggren, W. A. (1974). Paleocene benthonic foraminiferal biostratigraphy, biogeography and paleoecology of Libya and Mali. *Micropaleontology*, *20*(4), 449–465. https://doi.org/10.2307/1485130

Beydoun, Z. R. (1966). *Geology of the Arabian peninsula Protectorate and part of Dhufar* (p. 56). U.S. Geological Survey Professional Paper, 560-H.

Bitner, M. A., & Boukhary, M. (2012). First record of Eocene brachiopods from the United Arab Emirates, Arabian Gulf and their paleogeographical significance. *Neues Jahrbuch für Geologie und Paläontologie - Abhandlungen*, *265*(3), 275–279. https://doi.org/10.1127/0077-7749/2012/0263
Bluck, B. J., Ward, J. D., Cartwright, J., & Swart, R. (2007). The Orange River, southern Africa: An extreme example of a wave-dominated sediment dispersal system in the South Atlantic Ocean. *Journal of the Geological Society*, *164*(2), 341–351. https://doi.org/10.1144/0016-76492005-189
Botha, G. A. (2000). Paleosols and duricrusts. In T. C. Partridge, & R. R. Maud (Eds.), *The Cenozoic of southern Africa* (pp. 131–144). Oxford University Press.
Braun, J. (2018). A review of numerical modeling studies of passive margin escarpments leading to a new analytical expression for the rate of escarpment migration velocity. *Gondwana Research*, *53*, 209–224. https://doi.org/10.1016/j.gr.2017.04.012
Braun, J., Guillocheau, F., Robin, C., Baby, G., & Jelsma, H. (2014). Rapid erosion of the Southern African Plateau as it climbs over a mantle superswell. *Journal of Geophysical Research: Solid Earth*, *119*(7), 6093–6112. https://doi.org/10.1002/2014JB010998
Braun, J., Heimsath, A. M., & Chappell, J., (2001). Sediment transport mechanisms on soil-mantled hillslopes. *Geology*, *29*(8), 683–686. https://doi.org/10.1130/0091-7613(2001)029<0683:STMOSM>2.0.CO;2
Braun, J., Robert, X., & Simon-Labric, T. (2013). Eroding dynamic topography. *Geophysical Research Letters*, *40*(8), 1494–1499. https://doi.org/10.1002/grl.50310
Braun, J., & Willett, S. D. (2013). A very efficient O(n), implicit and parallel method to solve the stream power equation governing fluvial incision and landscape evolution. *Geomorphology*, *180–181*, 170–179. https://doi.org/10.1016/j.geomorph.2012.10.008
Brook, G. A., Railsback, L. B., & Marais, E. (2011). Reassessment of carbonate ages by dating both carbonate and organic material from an Etosha Pan (Namibia) stromatolite: Evidence of humid phases during the last 20 ka. *Quaternary International*, *229*(1–2), 24–37. https://doi.org/10.1016/j.quaint.2010.05.009
Brown, G. F., Schmidt, D. L., & Huffman, A. C. J. (1989). Geology of the Arabian Peninsula: Shield area of Western Saudi Arabia. *U. S. Geological Survey Professional Paper*, *560*, 199.
Burke, K. (1996). The African Plate. *South African Journal of Geology*, *99*(4), 341–409. https://doi.org/10.3133/pp560a
Canet, E., Fournier, A., & Jault, D. (2009). Forward and adjoint quasi-geostrophic models of the geomagnetic secular variation. *Journal of Geophysical Research*, *114*(11), 1–343. https://doi.org/10.1177/036215379602600412
Cavin, L., Bardet, N., Cappetta, H., Gheerbrant, E., Iarochene, S. M., & Sudre, J. (2000). A new Palaeocene albulid (Teleostei: Elopomorpha) from the Ouled Abdoun phosphatic basin, Morocco. *Geological Magazine*, *137*(5), 583–591. https://doi.org/10.1017/s0016756800004647
Chardon, D., Chevillotte, V., Beauvais, A., Grandin, G., & Boulangé, B. (2006). Planation, bauxites and epeirogeny: One or two paleosurfaces on the West African margin? *Geomorphology*, *82*(3–4), 273–282. https://doi.org/10.1016/j.geomorph.2006.05.008
Chardon, D., Grimaud, J.-L., Rouby, D., Beauvais, A., & Christophoul, F. (2016). Stabilization of large drainage basins over geological time scales: Cenozoic West Africa, hot spot swell growth, and the Niger River. *Geochemistry, Geophysics, Geosystems*, *17*(3), 1164–1181. https://doi.org/10.1002/2015GC006169
Coetzee, J. A. (1980). Tertiary environmental changes along the south-western African coast. *Palaeontologia Africana*, *23*, 197–203.
Coetzee, J. A., & Rogers, J. (1982). Palynological and lithological evidence for the Miocene palaeoenvironment in the Saldanha region (South Africa). *Palaeogeography, Palaeoclimatology, Palaeoecology*, *39*(1–2), 71–85. https://doi.org/10.1016/0031-0182(82)90073-6
Cole, G. A., Requejo, A. G., Ormerod, D., Yu, Z., & Clifford, A. (2000). Petroleum geochemical assessment of the lower Congo Basin. Petroleum systems of South Atlantic margins. *AAPG Memoir*, *73*(73), 325–340.
Coleman, R., Gregory, R., & Brown, G. (1983). *Cenozoic volcanic rocks of Saudi Arabia* (pp. 1–82). U.S. Geological Survey. https://doi.org/10.3133/OFR83788
Crosby, A. G., Fishwick, S., & White, N. (2010). Structure and evolution of the intracratonic Congo Basin. *Geochemistry, Geophysics, Geosystems*, *11*, 1–20, Q06010. https://doi.org/10.1029/2009GC003014
Culling, W. E. H. (1963). Soil creep and the development of hillside slopes. *The Journal of Geology*, *71*(2), 127–n.
Davies, G. F. (1994). Thermomechanical erosion of the lithosphere by mantle plumes. *Journal of Geophysical Research*, *99*(B8), 15709–15722. https://doi.org/10.1086/626891
de Wit, M. C. J. (1999). Post-Gondwana drainage and the development of diamond placers in western South Africa. *Economic Geology*, *94*(5), 721–740. https://doi.org/10.2113/gsecongeo.94.5.721
de Wit, M. C. J. (2003). Madagascar: Heads it's a continent, tails it's an island. *Annual Review of Earth and Planetary Sciences*, *31*, 213–248. https://doi.org/10.1146/annurev.earth.31.100901.141337
Delaunay, A. (2018). Les mouvements verticaux de Madagascar (90-0 Ma): Une analyse couplée des formes du relief et de l'enregistrement sédimentaire des marges ouest malgaches. *PhD Dissertation, L'Université de Rennes*, *1*, 1–374. https://doi.org/10.1029/94jb00119
DeMenocal, P. B. (1995). Plio-Pleistocene African Climate. *Science*, *270*(5233), 53–59. https://doi.org/10.1126/science.270.5233.53
DeMenocal, P. B. (2004). African climate change and faunal evolution during the Pliocene-Pleistocene. *Earth and Planetary Science Letters*, *220*(1–2), 3–24. https://doi.org/10.1016/S0012-821X(04)00003-2
DeMenocal, P. B., Ortiz, J., Guilderson, T., Adkins, J., Sarnthein, M., Baker, L., & Yarusinsky, M. (2000). Abrupt onset and termination of the African Humid Period: Rapid climate responses to gradual insolation forcing. *Quaternary Science Reviews*, *19*(1–5), 347–361. https://doi.org/10.1016/S0277-3791(99)00081-5
DeMets, C., Gordon, R. G., & Argus, D. F. (2010). Geologically current plate motions. *Geophysical Journal International*, *181*(1), 1–80. https://doi.org/10.1111/j.1365-246X.2009.04491.x
Dietrich, W. E., Reiss, R., Hsu, M.-L., & Montgomery, D. R. (1995). A process-based model for colluvial soil depth and shallow landsliding using digital elevation data. *Hydrological Processes*, *9*(March), 383–400.
Dixey, F. (1960). The geology and geomorphology of Madagascar, and a comparison with Eastern Africa. *Quarterly Journal of the Geological Society*, *116*(1–4), 255–268. https://doi.org/10.1002/hyp.3360090311
Doucouré, C. M., & de Wit, M. J. (2003). Old inherited origin for the present near-bimodal topography of Africa. *Journal of African Earth Sciences*, *36*(4), 371–388. https://doi.org/10.1016/S0899-5362(03)00019-8
Drake, N. A., El-Hawat, A. S., Turner, P., Armitage, S. J., Salem, M. J., White, K. H., & McLaren, S. (2008). Palaeohydrology of the Fazzan Basin and surrounding regions: The last 7 million years. *Palaeogeography, Palaeoclimatology, Palaeoecology*, *263*(3–4), 131–145. https://doi.org/10.1016/j.palaeo.2008.02.005
Droz, L., Rigaut, F., Cochonat, P., & Tofani, R. (1996). Morphology and recent evolution of the Zaire turbidite system (Gulf of Guinea). *GSA Bulletin*, *108*(3), 253–269.
Ebinger, C. J., Bechtel, T. D., Forsyth, D. W., & Bowin, C. O. (1989). Effective elastic plate thickness beneath the East African and Afar plateaus and dynamic compensation of the uplifts. *Journal of Geophysical Research: Solid Earth*, *94*(B3), 2883–2901. https://doi.org/10.1130/0016-7606(1996)108<0253:mareot>2.3.co;2

Ebinger, C. J., Yemane, T., Harding, D. J., Tesfaye, S., Kelley, S., & Rex, D. C. (2000). Rift deflection, migration, and propagation: Linkage of the Ethiopian and Eastern rifts, Africa. *Bulletin of the Geological Society of America*, *112*(2), 163–176. https://doi.org/10.1130/0016-7606(2000)112<163:RDMAPL>2.0.CO;2

Elmejdoub, N., & Jedoui, Y. (2009). Pleistocene raised marine deposits of the Cap Bon peninsula (N-E Tunisia): Records of sea-level highstands, climatic changes and coastal uplift. *Geomorphology*, *112*(3–4), 179–189. https://doi.org/10.1130/0016-7606(2000)112<163:rdmapl>2.0.co;2

Faccenna, C., Glišović, P., Forte, A., Becker, T. W., Garzanti, E., Sembroni, A., & Gvirtzman, Z. (2019). Role of dynamic topography in sustaining the Nile River over 30 million years. *Nature Geoscience*, *12*(December), 1012–1016. https://doi.org/10.1038/s41561-019-0472-x

Fairhead, J. D. (1979). A gravity link between the domally uplifted Cainozoic volcanic centres of North Africa and its similarity to the East African Rift System anomaly. *Earth and Planetary Science Letters*, *42*(1), 109–1017. https://doi.org/10.1016/0012-821X(79)90195-X

Feakins, S. J. (2013). Pollen-corrected leaf wax D/H reconstructions of northeast African hydrological changes during the late Miocene. *Palaeogeography, Palaeoclimatology, Palaeoecology*, *374*, 62–71. https://doi.org/10.1016/j.palaeo.2013.01.004

Fernandes, N. F., & Dietrich, W. E. (1997). Hillslope evolution by diffusive processes: The timescale for equilibrium adjustments. *Water Resources Research*, *33*(6), 1307–1318. https://doi.org/10.1029/97WR00534

Ferrier, K. L., Huppert, K. L., & Perron, J. T. (2013). Climatic control of bedrock river incision. *Nature*, *496*(7444), 206–209. https://doi.org/10.1038/nature11982

Fishwick, S. (2010). Surface wave tomography: Imaging of the lithosphere-asthenosphere boundary beneath central and southern Africa? *Lithos*, *120*(1–2), 63–73. https://doi.org/10.1016/j.lithos.2010.05.011

Fox, M., Goren, L., May, D. A., & Willett, S. D. (2014). Inversion of fluvial channels for paleorock uplift rates in Taiwan. *Journal of Geophysical Research: Earth Surface*, *119*(9), 1853–1875. https://doi.org/10.1002/2014JF003196

Frierson, D. M. W., Lu, J., & Chen, G. (2007). Width of the Hadley cell in simple and comprehensive general circulation models. *Geophysical Research Letters*, *34*(18), 1–5. https://doi.org/10.1029/2007GL031115

Gasse, F. (2000). Hydrological changes in the African tropics since the last glacial maximum. *Quaternary Science Reviews*, *19*(1–5), 189–211. https://doi.org/10.1016/S0277-3791(99)00061-X

Gingerich, P. D., & Zouhri, S. (2015). New fauna of archaeocete whales (Mammalia, Cetacea) from the Bartonian middle Eocene of southern Morocco. *Journal of African Earth Sciences*, *111*, 273–286. https://doi.org/10.1016/j.jafrearsci.2015.08.006

Globig, J., Fernàndez, M., Vergés, J., Robert, A., & Faccenna, C. (2016). New insights into the crust and lithospheric mantle structure of Africa from elevation, geoid, and thermal analysis. *Journal of Geophysical Research: Solid Earth*, *121*, 1–36. https://doi.org/10.1002/2016JB012972. Received

Glotzbach, C. (2015). Deriving rock uplift histories from data-driven inversion of river profiles. *Geology*, *43*(6), 467–470. https://doi.org/10.1130/G36702.1

Godard, V., Tucker, G. E., Burch Fisher, G., Burbank, D. W., & Bookhagen, B. (2013). Frequency-dependent landscape response to climatic forcing. *Geophysical Research Letters*, *40*(5), 859–863. https://doi.org/10.1002/grl.50253

Goren, L., Fox, M., & Willett, S. D. (2014). Tectonics from fluvial topography using formal linear inversion: Theory and applications to the Inyo Mountains, California. *Journal of Geophysical Research F: Earth Surface*, *119*(8), 1651–1681. https://doi.org/10.1002/2014JF003079

Goudie, A. S. (2005). The drainage of Africa since the Cretaceous. *Geomorphology*, *67*(3–4), 437–456. https://doi.org/10.1016/j.geomorph.2004.11.008

Griffin, D. L. (2002). Aridity and humidity: Two aspects of the late Miocene climate of North Africa and the Mediterranean. *Palaeogeography, Palaeoclimatology, Palaeoecology*, *182*(1–2), 65–91. https://doi.org/10.1016/S0031-0182(01)00453-9

Grimaud, J.-L., Rouby, D., Chardon, D., & Beauvais, A. (2017). Cenozoic sediment budget of West Africa and the Niger delta. *Basin Research*, 1–18. https://doi.org/10.1111/bre.12248

Gripp, A. E., & Gordon, R. G. (1990). Current plate velocities relative to the hotspots incorrating the NUVEL-1 global plate motion model. *Geophysical Research Letters*, *30*(8), 1109–1186.

Guillocheau, F., Rouby, D., Robin, C., Helm, C., Rolland, N., Le Carlier de Veslud, C., & Braun, J. (2012). Quantification and causes of the terrigeneous sediment budget at the scale of a continental margin: A new method applied to the Namibia-South Africa margin. *Basin Research*, *24*(1), 3–30. https://doi.org/10.1029/gl017i008p01109

Guillocheau, F., Simon, B., Baby, G., Bessin, P., Robin, C., & Dauteuil, O. (2017). Planation surfaces as a record of mantle dynamics: The case example of Africa. *Gondwana Research*, 1–17. https://doi.org/10.1016/j.gr.2017.05.015

Guiraud, M., Buta-Neto, A., & Quesne, D. (2010). Segmentation and differential post-rift uplift at the Angola margin as recorded by the transform-rifted Benguela and oblique-to-orthogonal-rifted Kwanza basins. *Marine and Petroleum Geology*, *27*(5), 1040–1068. https://doi.org/10.1016/j.marpetgeo.2010.01.017

Guiraud, R., & Bosworth, W. (1999). Phanerozoic geodynamic evolution of northeastern Africa and the northwestern Arabian platform. *Tectonophysics*, *315*(1–4), 73–108. https://doi.org/10.1016/S0040-1951(99)00293-0

Guiraud, R., Issawi, B., & Bosworth, W. (2001). Phanerozoic history of Egypt and surrounding areas. *In: Peri-tethyan rift/wrench basins and passive margins* (pp. 469–104). MNHN Paris.

Gunnell, Y., & Burke, K. (2008). *The African erosion surface: A continental-scale Synthesis of Geomorphology, tectonics, and Environmental change over the Past 180 million Years* (pp. 1–66). Memoir of the Geological Society of America. https://doi.org/10.1130/2008.1201

Gunnell, Y., Zeyen, H., & Calvet, M. (2008). The African erosion surface: A continental-scale synthesis of geomorphology, tectonics, and environmental change over the past 180 million years. *Earth and Planetary Science Letters*, *276*(3–4), 302–313. https://doi.org/10.1016/j.epsl.2008.09.031

Gurnis, M., Mitrovica, J. X., Ritsema, J., & Van Heijst, H.-J. (2000). Constraining mantle density structure using geological evidence of surface uplift rates: The case of the African Superplume. *Geochemistry, Geophysics, Geosystems*, *1*(7), 1–35. https://doi.org/10.1029/1999GC000035

Haack, R. C., Sundararaman, P., Diedjomahor, J. O., Gant, N. J., May, E. D., & Kelsch, K. (2000). *Niger Delta Petroleum Systems, Nigeria* (Vol. 73, pp. 213–n). AAPG Memoir.

Haas, O., & Miller, A. K. (1952). Eocene nautiloids of British Somaliland. *Bulletin of the American Museum of Natural History*, *99*(5), 317.

Hartley, R., Watts, A. B., & Fairhead, J. D. (1996). Isostasy of Africa. *Earth and Planetary Science Letters*, *137*(1–4), 1–18. https://doi.org/10.1016/0012-821X(95)00185-F

Hartmann, J., & Moosdorf, N. (2012). The new global lithological map database GLiM: A representation of rock properties at the Earth surface. *Geochemistry, Geophysics, Geosystems*, *13*(12), 1–37. https://doi.org/10.1029/2012GC004370

Hobley, D. E., Adams, J. M., Siddhartha Nudurupati, S., Hutton, E. W., Gasparini, N. M., Istanbulluoglu, E., & Tucker, G. E. (2017). Creative computing with Landlab: An open-source toolkit for building, coupling, and exploring two-dimensional numerical models of Earth-surface dynamics. *Earth Surface Dynamics*, *5*(1), 21–46. https://doi.org/10.5194/esurf-5-21-2017

Hoggard, M. J., White, N., & Al-Attar, D. (2016). Global dynamic topography observations reveal limited influence of large-scale mantle flow. *Nature Geoscience*, *9*(May), 1–8. https://doi.org/10.1038/ngeo2709

Hoggard, M. J., Winterbourne, J., Czarnota, K., & White, N. (2017). Oceanic residual depth measurements, the plate cooling model, and global dynamic topography. *Journal of Geophysical Research: Solid Earth*, *122*(3), 2328–2463. https://doi.org/10.1002/2016JB013457

Holmes, A. (1945). *Principles of physical geology (No. 1)*. Thomas Nelson and Sons Ltd. https://doi.org/10.1080/11035894509446436

Holz, C., Stuut, J. B. W., Henrich, R., & Meggers, H. (2007). Variability in terrigenous sedimentation processes off northwest Africa and its relation to climate changes: Inferences from grain-size distributions of a Holocene marine sediment record. *Sedimentary Geology*, *202*(3), 499–508. https://doi.org/10.1016/j.sedgeo.2007.03.015

Howard, A. D., Dietrich, W. E., & Seidl, M. A. (1994). Modeling fluvial erosion on regional to continental scales. *Journal of Geophysical Research*, *99*(B7), 13971–13986.

Ismail, A. A., Boukhary, M., & Naby, A. I. A. (2010). Subsurface stratigraphy and micropaleontology of the Neogene rocks, Nile Delta, Egypt. *Geologia Croatica*, *63*(1), 1–26. https://doi.org/10.1029/94jb00744

Jenson, S. K., & Domingue, J. O. (1988). Extracting topographic structure from digital elevation data for geographic information system analysis. *Photogrammetric Engineering & Remote Sensing*, *54*(November), 1593–1600. https://doi.org/10.4154/gc.2010.01

Jones, A. G., Afonso, J. C., & Fullea, J. (2017). Geochemical and geophysical constraints on the dynamic topography of the Southern African Plateau. *Geochemistry, Geophysics, Geosystems*, *18*, 1–20. https://doi.org/10.1002/2017GC006908

Jones, S. M., Lovell, B., & Crosby, A. G. (2012). Comparison of modern and geological observations of dynamic support from mantle convection. *Journal of the Geological Society*, *169*(6), 745–3575. https://doi.org/10.1144/jgs2011-118

Jouve, S. (2005). A new description of the skull of Dyrosaurus phosphaticus (Thomas, 1893) (Mesoeucrocodylia: Dyrosauridae) from the Lower Eocene of North Africa. *Canadian Journal of Earth Sciences*, *42*, 323–337. https://doi.org/10.1139/e05-008

Karner, G. D., & Driscoll, N. W. (1999). Tectonic and stratigraphic development of the West African and eastern Brazilian Margins: Insights from quantitative basin modelling. *Geological Society, London, Special Publications*, *153*(1), 11–40. https://doi.org/10.1144/GSL.SP.1999.153.01.02

Keller, G., Adatte, T., Stinnesbeck, W., Luciani, V., Karoui-Yaakoub, N., & Zaghbib-Turki, D. (2002). Palaeoecology of the Cretaceous-Tertiary mass extinction in planktonic foraminifera. *Palaeogeography, Palaeoclimatology, Palaeoecology*, *178*, 257–297.

Keller, G., Li, L., & MacLeod, N. (1995). The Cretaceous/Tertiary boundary stratotype section at El Kef, Tunisia: How catastrophic was the mass extinction? *Palaeogeography, Palaeoclimatology, Palaeoecology*, *119*, 221–254. https://doi.org/10.1016/s0031-0182(01)00399-6

King, L. (1978). *The Geomorphology of central and southern Africa. Biogeography and Ecology of southern Africa* (p. 31). Monographiae Biologicae.

Košťák, M., Jagt, J. W. M., Speijer, R. P., Stassen, P., & Steurbaut, E. (2013). New Paleocene sepiid coleoids (Cephalopoda) from Egypt: Evolutionary significance and origin of the Sepiid 'rostrum. *PLoS One*, *8*(11), 1–19. https://doi.org/10.1371/journal.pone.0081180

Kröpelin, S., & Soulié-Märsche, I. (1991). Charophyte remains from Wadi Howar as evidence for deep mid-Holocene freshwater lakes in the eastern Sahara of Northwest Sudan. *Quaternary Research*, *36*(2), 210–223. https://doi.org/10.1016/0033-5894(91)90026-2

Larrasoaña, J. C., Roberts, A. P., & Rohling, E. J. (2013). Dynamics of green Sahara periods and their role in Hominin evolution. *PLoS One*, *8*(10). https://doi.org/10.1371/journal.pone.0076514

Lavier, L. L., Steckler, M. S., & Brigaud, F. (2001). Climatic and tectonic control on the Cenozoic evolution of the West African margin. *Marine Geology*, *178*(1–4), e76514–80. https://doi.org/10.1016/S0025-3227(01)00175-X

Li, K., Jackson, A., & Livermore, P. W. (2011). Variational data assimilation for the initial-value dynamo problem. *Physical Review E*, *84*(056321), 1–16. https://doi.org/10.1103/PhysRevE.84.056321

Lighthill, M. J., & Whitham, G. B. (1955). On kinematic waves I. Flood movement in long rivers. *Proceedings of the Royal Society of London*, *229*, 281–316. https://doi.org/10.1098/rspa.1955.0088

Lo, P. G., Dia, A., & Kampunzu, A. B. (1992). Cenozoic volcanism in Western Senegal and its relationship to the opening of the Central Atlantic Ocean. *Tectonophysics*, *209*(1–4), 281–291. https://doi.org/10.1016/0040-1951(92)90035-5

Lodhia, B. H., Roberts, G. G., Fraser, A. J., Jarvis, J., Newton, R., & Cowan, R. J. (2019). Observation and simulation of solid sedimentary flux: Examples from Northwest Africa. *Geochemistry, Geophysics, Geosystems*, *20*, 1–22. https://doi.org/10.1029/2019gc008262

Lorenz, E. N. (1963). Deterministic nonperiodic flow. *Journal of the Atmospheric Sciences*, *20*, 130–4634.

Lucazeau, F., Brigaud, F., & Leturmy, P. (2003). Dynamic interactions between the Gulf of Guinea passive margin and the Congo River drainage basin: 2. Isostasy and uplift. *Journal of Geophysical Research*, *108*(B8), 2384. https://doi.org/10.1175/1520-0469(1963)020<0130:dnf>2.0.co;2

Madden, C. T., Naqvi, I. M., Whitmore, F. C., Jr, Schmidt, D. L., Langston, W., Jr, & Wood, R. C. (1980). Paleocene vertebrates from coastal deposits in the Harrat Haden area, At Taif region, Kingdom of Saudi Arabia. *U.S. Geological Survey Open File Report*, *269*, 1–32.

Martill, D. M., Ibrahim, N., Brito, P. M., Baider, L., Zhouri, S., Loveridge, R., & Hing, R. (2011). A new Plattenkalk Konservat Lagerstätte in the Upper Cretaceous of Gara Sbaa, south-eastern Morocco. *Cretaceous Research*, *32*(4), 433–446. https://doi.org/10.1016/j.cretres.2011.01.005

Matsuura, K., Willmott, C. J., & Hing, R. (2012). *Terrestrial precipitation: 1900-2010 gridded Monthly time series*. Department of Geography, University of Delaware. Retrieved from https://climatedataguide.ucar.edu/climate-data/global-land-precipitation-and-temperature-willmott-matsuura-university-delaware

McCartney, J., Roberts, E., Tapanila, L., & O'Leary, M. (2018). Large palaeophiid and nigerophiid snakes from Paleogene Trans-Saharan Seaway deposits of Mali. *Acta Palaeontologica Polonica*, *63*(2), 207–220. https://doi.org/10.4202/app.00442.2017

McKenzie, D. (2010). The influence of dynamically supported topography on estimates of Te. *Earth and Planetary Science Letters*, *295*(1–2), 127–138. https://doi.org/10.1016/j.epsl.2010.03.033

McKenzie, D., & Fairhead, D. (1997). Estimates of the effective elastic thickness of the continental lithosphere from Bouguer and free air gravity anomalies. *Journal of Geophysical Research: Solid Earth*, *102*(B12), 27523–27552. https://doi.org/10.1029/97JB02481

McNab, F., Ball, P. W., Hoggard, M. J., & White, N. J. (2018). Neogene uplift and magmatism of Anatolia: Insights from drainage analysis and basaltic geochemistry. *Geochemistry, Geophysics, Geosystems*, *19*(1), 175–213. https://doi.org/10.1002/2017GC007251

Moucha, R., & Forte, A. M. (2011). Changes in African topography driven by mantle convection: Supplementary information. *Nature Geoscience*, *4*(10), 707–712. https://doi.org/10.1038/ngeo1235

Moufti, A. M. B. (2010). Field, mineralogical and geochemical characteristics of as-Sarat laterite profiles, SW Saudi Arabia. *Journal of King Abdulaziz University - Earth Sciences*, *21*(2), 47–75. https://doi.org/10.4197/Ear.21-2.3

Murphy, B. P., Johnson, J. P. L., Gasparini, N. M., & Sklar, L. S. (2016). Chemical weathering as a mechanism for the climatic control of bedrock river incision. *Nature*, *532*(7598), 223–227. https://doi.org/10.1038/nature17449

Nyagah, K. (1995). Stratigraphy, depositional history and environments of deposition of Cretaceous through Tertiary strata in the Lamu Basin, southeast Kenya and implications for reservoirs for hydrocarbon exploration. *Sedimentary Geology*, *96*(1–2), 43–71. https://doi.org/10.1016/0037-0738(94)00126-F

Nyblade, A. A., & Robinson, S. W. (1994). The African Superswell. *Geophysical Research Letters*, *21*(9), 765–768. https://doi.org/10.1029/94GL00631

Nyblade, A. A., & Sleep, N. H. (2003). Long lasting epeirogenic uplift from mantle plumes and the origin of the Southern African Plateau. *Geochemistry, Geophysics, Geosystems*, *4*(12). https://doi.org/10.1029/2003GC000573

O'Leary, M. A., Sarr, R., Malou, R., Sow, E. H., Lepre, C., & Hill, R. V. (2012). A new fossil Amiid from the Eocene of Senegal and the persistence of extinct marine Amiids after the cretaceous–paleogene boundary. *Copeia*, *4*, 603–608. https://doi.org/10.1643/ci-11-130

Parker, R. L. (1994). Linear problems with exact data. *In Geophysical inverse theory* (pp. 55–104). Princeton University Press.

Parrish, J. T., Ziegler, A. M., & Scotese, C. R. (1982). Rainfall patterns and the distribution of coals and evaporites in the Mesozoic and Cenozoic. *Palaeogeography, Palaeoclimatology, Palaeoecology*, *40*, 67–101.

Partridge, T. C., & Maud, R. (1987). Geomorphic evolution of southern Africa since the Mesozoic. *South African Journal of Geology*, *90*(2), 179–208. https://doi.org/10.1016/0031-0182(82)90085-2

Partridge, T. C., Demenocal, P. B., Lorentz, S. A., Paiker, M. J., & Vogel, J. C. (1997). Orbital forcing of climate over South Africa: A 200,000-year rainfall record from the Pretoria Saltpan. *Quaternary Science Reviews*, *16*(10), 1125–1133. https://doi.org/10.1016/S0277-3791(97)00005-X

Paul, J. D., Roberts, G. G., & White, N. (2014). The African landscape through space and time. *Tectonics*, *33*(6), 898–935. https://doi.org/10.1002/2013TC003479

Petters, S. W. (1978). Mid-Cretaceous paleoenvironments and biostratigraphy of the Benue Trough, Nigeria. *Bulletin of the Geological Society of America*, *89*(1), 151–154. https://doi.org/10.1130/0016-7606(1978)89<151:MPABOT>2.0.C.O;2

Piccoli, G., & Savazzi, E. (1983). Five shallow benthic mollusc faunas from the Upper Eocene (Baron, Priabona, Garoowe, Nanggulan, Takashima). *Bollettino della Societa Paleontologica Italiana*, *22*(1–2), 31–47. https://doi.org/10.1130/0016-7606(1978)89<151:mpabot>2.0.co;2

Powers, R. W., Ramirez, L. F., Redmond, C. D., & Elberg, E. L., Jr. (1966). *Geology of the Arabian peninsula sedimentary Geology of Saudi Arabia* (p. 154). U.S. Geological Survey Professional Paper, 560-D.

Priestley, K., McKenzie, D., & Ho, T. (2019). A lithosphere-asthenosphere boundary - A global model derived from multimode surface-wave tomography and petrology. *Geophysical Monograph*, *239*, 111–123.

Pritchard, D., Roberts, G. G., White, N. J., & Richardson, C. N. (2009). Uplift histories from river profiles. *Geophysical Research Letters*, *36*, L24301. https://doi.org/10.1029/2009GL040928

Reijers, T. (2011). Stratigraphy and sedimentology of the Niger Delta. *Geologos*, *17*(3), 133–162. https://doi.org/10.2478/v10118-011-0008-3

Reyment, R. A., & Dingle, R. V. (1987). Palaeogeography of Africa during the Cretaceous period. *Palaeogeography, Palaeoclimatology, Palaeoecology*, *59*, 93–116.

Richards, F. D., Hoggard, M. J., & White, N. J. (2016). Cenozoic epeirogeny of the Indian peninsula. *Geochemistry, Geophysics, Geosystems*, *17*, 2825–2834. https://doi.org/10.1016/0031-0182(87)90076-9

Roberts, D. L., & Brink, J. S. (2002). Dating and correlation of Neogene coastal deposits in the Western Cape (South Africa): Implications for neotectonism. *South African Journal of Geology*, *105*, 337–4954.

Roberts, G. G. (2019). Scales of similarity and disparity between drainage networks. *Geophysical Research Letters*, *46*, 1–10. https://doi.org/10.2113/1050337

Roberts, G. G., Paul, J. D., White, N., & Winterbourne, J. (2012). Temporal and spatial evolution of dynamic support from river profiles: A framework for Madagascar. *Geochemistry, Geophysics, Geosystems*, *13*(4), 1–3790. https://doi.org/10.1029/2012GC004040

Roberts, G. G., & White, N. (2010). Estimating uplift rate histories from river profiles using African examples. *Journal of Geophysical Research*, *115*(B2), B02406. https://doi.org/10.1029/2009JB006692

Roberts, G. G., White, N., & Lodhia, B. H. (2019). The generation and scaling of longitudinal river profiles. *Journal of Geophysical Research: Earth Surface*, *124*, 17. https://doi.org/10.1029/2018JF004796

Rodríguez Tribaldos, V., White, N. J., Roberts, G. G., & Hoggard, M. J. (2017). Spatial and temporal uplift history of South America from calibrated drainage analysis. *Geochemistry, Geophysics, Geosystems*, *18*(6), 2321–n. https://doi.org/10.1002/2017GC006909

Roe, G. H., Montgomery, D. R., & Hallet, B. (2002). Effects of orographic precipitation variations on the concavity of steady-state river profiles. *Geology*, *30*(2), 143–146.

Rosenbloom, N. A., & Anderson, R. S. (1994). Hillslope and channel evolution in a marine terraced landscape, Santa Cruz, California. *Journal of Geophysical Research*, *99*(B7), 14013–14029. https://doi.org/10.1130/0091-7613(2002)030<0143:eoopvo>2.0.co;2

Rouby, D., Bonnet, S., Guillocheau, F., Gallagher, K., Robin, C., Biancotto, F., & Braun, J. (2009). Sediment supply to the Orange sedimentary system over the last 150 My: An evaluation from sedimentation/denudation balance. *Marine and Petroleum Geology*, *26*(6), 782–794. https://doi.org/10.1016/j.marpetgeo.2008.08.004

Rouby, D., Nalpas, T., Jermannaud, P., Robin, C., Guillocheau, F., Raillard, S., et al. (2011). Gravity driven deformation controlled by the migration of the delta front: The Plio-Pleistocene of the Eastern Niger Delta. *Tectonophysics*, *513*(1–4), 54–67. https://doi.org/10.1016/j.tecto.2011.09.026

Royden, L., & Perron, J. T. (2013). Solutions of the stream power equation and application to the evolution of river longitudinal profiles. *Journal of Geophysical Research: Earth Surface*, *118*(2), 497–518. https://doi.org/10.1002/jgrf.20031

Rudge, J. F., Roberts, G. G., White, N. J., & Richardson, C. N. (2015). Uplift histories of Africa and Australia from linear inverse modeling of drainage inventories. *Journal of Geophysical Research: Earth Surface*, *120*(5), 894–914. https://doi.org/10.1002/2014JF003297

Rudge, J. F., Shaw Champion, M. E., White, N., McKenzie, D., & Lovell, B. (2008). A plume model of transient diachronous uplift at the Earth's surface. *Earth and Planetary Science Letters*, *267*(1–2), 146–160. https://doi.org/10.1016/j.epsl.2007.11.040

Ruetenik, G. A., Moucha, R., & Hoke, G. D. (2016). Landscape response to changes in dynamic topography. *Terra Nova*, *28*(4), 289–296. https://doi.org/10.1111/ter.12220

Sahagian, D. (1988). Epeirogenic motions of Africa as inferred from Cretaceous shoreline deposits. *Tectonics*, *7*(1), 125–138. https://doi.org/10.1029/TC007i001p00125

Said, R. (1981). *The geological evolution of the River Nile*. Springer-Verlag.

Salles, T., Flament, N., & Müller, D. (2017). Influence of mantle flow on the drainage of eastern Australia since the Jurassic Period. *Geochemistry, Geophysics, Geosystems*, *18*(1), 280–305. https://doi.org/10.1002/2016GC006617

Salles, T., & Hardiman, L. (2016). Badlands: An open-source, flexible and parallel framework to study landscape dynamics. *Computers & Geosciences*, *91*, 77–89. https://doi.org/10.1016/j.cageo.2016.03.011

Salman, G., & Abdula, I. (1995). Development of the Mozambique and Ruvuma sedimentary basins, offshore Mozambique. *Sedimentary Geology*, *96*(1–2), 7–41. https://doi.org/10.1016/0037-0738(95)00125-R

Schaeffer, A. J., & Lebedev, S. (2013). Global shear speed structure of the upper mantle and transition zone. *Geophysical Journal International*, *194*(1), 417–449. https://doi.org/10.1093/gji/ggt095

Séranne, M., & Anka, Z. (2005). South Atlantic continental margins of Africa: A comparison of the tectonic vs climate interplay on the evolution of equatorial west Africa and SW Africa margins. *Journal of African Earth Sciences*, *43*(1–3), 283–300. https://doi.org/10.1016/j.jafrearsci.2005.07.010

Séranne, M., & Nzé Abeigne, C. R. (1999). Oligocene to Holocene sediment drifts and bottom currents on the slope of Gabon continental margin (west Africa) consequences for sedimentation and southeast Atlantic upwelling. *Sedimentary Geology*, *128*(3–4), 179–199. https://doi.org/10.1016/S0037-0738(99)00069-X

Sestini, G. (1989). Nile Delta: A review of depositional environments and geological history. *Geological Society, London, Special Publications*, *41*(1), 99–127. https://doi.org/10.1144/GSL.SP.1989.041.01.09

Shobe, C. M., Tucker, G. E., & Barnhart, K. R. (2017). The SPACE 1.0 model: A Landlab component for 2-D calculation of sediment transport, bedrock erosion, and landscape evolution. *Geoscientific Model Development*, *10*(12), 4577–4604. https://doi.org/10.5194/gmd-10-4577-2017

Skelton, P. W., Nolan, S. C., & Scott, R. W. (1990). The Maastrichtian transgression onto the northwestern flank of the Proto-Oman Mountains: Sequences of rudist-bearing beach to open shelf facies. *The Geology and Tectonics of the Oman Region*, *49*(1), 521–547. https://doi.org/10.1144/GSL.SP.1992.049.01.32

Smith, T. R., & Bretherton, F. P. (1972). Stability and the conservation of mass in drainage basin evolution. *Water Resources Research*, *8*(6), 1506–1529.

Soliar, T. (1988). The mosasaur Goronyosaurus from the Upper Cretaceous of Sokoto State, Nigeria. *Palaeontology*, *31*(3), 747–762. https://doi.org/10.1029/wr008i006p01506

Stanley, J. R., Braun, J., Baby, G., Guillocheau, F., Robin, C., Flowers, R. M., & Beucher, R. (2021). Constraining plateau uplift in Southern Africa by combining thermochronology, sediment flux, topography, and landscape evolution modeling. *Journal of Geophysical Research: Solid Earth*, *126*, 1–34. https://doi.org/10.1029/2020JB021243

Stephenson, S. N., Roberts, G. G., Hoggard, M. J., & Whittaker, A. C. (2014). A Cenozoic uplift history of Mexico and its surroundings from longitudinal river profiles. *Geochemistry, Geophysics, Geosystems*, *15*(12), 4734–4758. https://doi.org/10.1002/2014GC005425

Stock, J. D., & Montgomery, D. R. (1999). Geologic constraints on bedrock river incision using the stream power law. *Journal of Geophysical Research*, *104*(B3), 4983. https://doi.org/10.1002/2014gc005425

Stuut, J. B. W., Prins, M. A., Schneider, R. R., Weltje, G. J., Fred Jansen, J. H., & Postma, G. (2002). A 300-kyr record of aridity and wind strength in southwestern Africa: Inferences from grain-size distributions of sediments on Walvis Ridge, SE Atlantic. *Marine Geology*, *180*(1–4), 221–4993. https://doi.org/10.1016/S0025-3227(01)00215-8

Tantawy, A. A., Keller, G., Adatte, T., Stinnesbeck, W., Kassab, A., & Schulte, P. (2001). Maastrichtian to Paleocene depositional environment of the Dakhla Formation, Western Desert, Egypt: Sedimentology, mineralogy, and integrated micro- and macrofossil biostratigraphies. *Cretaceous Research*, *22*(6), 795–827. https://doi.org/10.1006/cres.2001.0291

Tapanila, L., Roberts, E. M., Bouare, M. L., Sissoko, F., & O'Leary, M. A. (2008). Phosphate taphonomy of bone and coprolite conglomerates: A case study from the Eocene of Mali, NW Africa. *PALAIOS*, *23*(3), 139–152. https://doi.org/10.2110/palo.2006.p06-113r

Tapley, B., Ries, J., Bettadpur, S., Chambers, D., Cheng, M., Condi, F., & Poole, S. (2007). *The GGM03 mean earth gravity model from GRACE*. AGU Fall Meeting Abstracts.

Thomas, M. F. (1994). *Geomorphology in the tropics: A study of weathering and denudation in low latitudes*. Wiley.

Thorne, R. L., Roberts, S., & Herrington, R. (2012). Climate change and the formation of nickel laterite deposits. *Geology*, *40*(4), 331–334. https://doi.org/10.1130/G32549.1

Tinker, J., de Wit, M., & Brown, R. (2008). Linking source and sink: Evaluating the balance between onshore erosion and offshore sediment accumulation since Gondwana break-up, South Africa. *Tectonophysics*, *455*(1–4), 77–93. https://doi.org/10.1016/j.tecto.2007.10.009

Tong, H., & Hirayama, R. (2008). A new species of Argillochelys (Testudines: Cryptodira: Cheloniidae) from the Ouled Abdoun phosphate basin, Morocco. *Bulletin de la Societe Geologique de France*, *179*(6), 623–630. https://doi.org/10.2113/gssgfbull.179.6.623

Uhen, M., Clapham, M., & Marshall, C. (2019). *Paleobiology database*. https://paleobiodb.org

van Zinderen Bakker, E. M., & Mercer, J. H. (1986). Major late Cenozoic climatic events and paleoenvironmental changes in Africa viewed in a world wide context. *Palaeogeography, Palaeoclimatology, Palaeoecology*, *56*, 217–235.

Walford, H. L. (2003). *Spatial and temporal evolution of African epeirogeny (Unpublished doctoral dissertation)* (pp. 1–217). University of Cambridge.

Walford, H. L., White, N. J., & Sydow, J. C. (2005). Solid sediment load history of the Zambezi Delta. *Earth and Planetary Science Letters*, *238*(1–2), 49–63. https://doi.org/10.1016/j.epsl.2005.07.014

Walker, R. T., Telfer, M., Kahle, R. L., Dee, M. W., Kahle, B., Schwenninger, J.-L., et al. (2016). Rapid mantle-driven uplift along the Angolan margin in the late Quaternary. *Nature Geoscience*, *1*(November). https://doi.org/10.1038/ngeo2835

Wapenhans, I., Fernandes, V. M., O'Malley, C., White, N., Roberts, G. G., & Watts, A. B. (2021). Scale-dependent contributors to river profile geometry. *Journal of Geophysical Research: Earth Surface*, *126*, 909–914. https://doi.org/10.1029/2020jf005879

Wessel, P., Luis, J., Uieda, L., Scharroo, R., Wobbe, F., Smith, W. H. F., & Tian, D. (2019). The generic mapping tools version 6. *Geochemistry, Geophysics, Geosystems*, *20*, 1–9. https://doi.org/10.1029/2019gc008515

Whipple, K. X., & Tucker, G. E. (1999). Dynamics of the stream-power river incision model: Implications for height limits of mountain ranges, landscape response timescales, and research needs. *Journal of Geophysical Research*, *104*(B8), 661–5564.

Whitmore, F. C., & Madden, C. T. (1994). *Paleocene vertebrates from Jabal Umm Himar, kingdom of Saudi Arabia, 2093*. U.S. Geological Survey Bulletin. https://doi.org/10.1029/1999jb900120

Wildman, M., Brown, R., Beucher, R., Persano, C., Stuart, F., Gallagher, K., & Carter, A. (2016). The chronology and tectonic style of landscape evolution along the elevated Atlantic continental margin of South Africa resolved by joint apatite fission track and (U-Th-Sm)/He thermochronology. *Tectonics*, *35*(3), 511–545. https://doi.org/10.1002/2015TC004042

Wilson, J. W. P., Roberts, G. G., Hoggard, M. J., & White, N. J. (2014). Cenozoic epeirogeny of the Arabian Peninsula from drainage modeling. *Geochemistry, Geophysics, Geosystems*, *15*, 3723–3761. https://doi.org/10.1002/2014GC005283

Wu, S., Bras, R. L., & Barros, A. P. (2006). Sensitivity of channel profiles to precipitation properties in mountain ranges. *Journal of Geophysical Research*, *111*(1), 1–13. https://doi.org/10.1029/2004JF000164

Zachos, L. G., Smadi, A., & Ahmad, F. (2008). Oligocene echinoids from Wadi Al Ghadaf, Jordan. *Rivista Italiana di Paleontologia e Stratigrafia*, *114*(1), 41–49.

Zalmout, I. S., Mustafa, H. A., & Gingerich, P. D. (2000). Priabonian Basilosaurus Isis (Cetacea) from the Wadi Esh-Shallala formation: First marine mammal from the Eocene of Jordan. *Journal of Vertebrate Paleontology*, *20*(1), 201–204. https://doi.org/10.1671/0272-4634(2000)020

Ziegler, M. A. (2001). Late Permian to Holocene paleofacies evolution of the Arabian Plate and its hydrocarbon occurrences. *GeoArabia*, *6*(3), 445–504. https://doi.org/10.1671/0272-4634(2000)020[0201:pbicft]2.0.co;2